Universidade de Lisboa

Faculdade de Ciências

Departamento de Física

Epileptogenic focus localization and complexity analysis of its BOLD signal

Vânia Sofia Santos Tavares

Dissertação

Mestrado Integrado em Engenharia Biomédica e Biofísica

Perfil em Engenharia Clínica e Instrumentação Médica

2014

Universidade de Lisboa

Faculdade de Ciências

Departamento de Física

Epileptogenic focus localization and complexity analysis of its BOLD signal

Vânia Sofia Santos Tavares

Dissertação

Mestrado Integrado em Engenharia Biomédica e Biofísica

Perfil em Engenharia Clínica e Instrumentação Médica

Orientadores: Professor Hugo Ferreira

Professor Alberto Leal

2014

A emoção e a sua vivência constituem a base daquilo que os seres humanos descrevem há milénios como sendo a alma ou o espírito humano.

António Damásio

ACKNOWLEDGMENTS

First of all I would like to thank my supervisor Professor Hugo Ferreira for giving me the opportunity to learn and for all the patience, advices, guidance and support in my academic path.

I would like to thank my co-supervisor Dr. Alberto Leal for the availability and contribution to this work and also for the kindness for providing me the epileptic patients' data. I´m very grateful for that.

I'm also thankful to Dr. Carlos Capela from neurology department and Dr. Luís Cerqueira from Hospital São José, Centro Hospitalar de Lisboa Central, E.P. E. for so kindly providing me data from epileptic patients.

I also thank to Technical University of Graz for kindly made available some subjects datasets used on this work.

I still have to thank André Ribeiro for the contribution given to part of this work development.

To all the persons who make me go on living every day. To my grandmother for having taught me to play as in the old days – using my imagination. For all the moments when, even without understanding me, you gave me your support.

To Rafa and Miguel, my forever beloved ones and brothers, for all the hugs and "I love you so much, sister!". To you a sincere thanks.

To my sister and bestfriend Joana. Pages are not enough to describe all the moments when your support was important. From the long nights awaken working and discussing ideas to the walking days that allowed me to recover my strength. Thank you for being by my side.

To Vitor, my daily light, my inner comfort, my strength to go on day after day, my morning coffee companion, my lift at the end of the day, my life support for these last eight years. I thank you from the bottom of my heart.

At last to my mom and dad, an endless gratitude. To mom for all the nights you didn´t rest because you were listening to me. To dad for reducing all problems to *base X(times) height dividing by two*. Thank you for everything.

This research was supported by Fundação para a Ciência e Tecnologia (FCT) and Ministério da Ciência e Educação (MCE) Portugal (PIDDAC) under grants PTDC/SAU-ENB/120718/2010 and PEst-OE/SAU/UI0645/2014.

RESUMO

Epilepsia é considerada a mais importante doença neurológica crónica a nível mundial. Esta afeta mais de 50 milhões de pessoas de todas as idades, e dessa população apenas 70% dos casos são controláveis com fármacos anti-epiléticos. Dos restantes 30%, 10% beneficiam da ressecação cirúrgica da região responsável pela atividade epilética e os restantes 20% não conseguem controlar adequadamente as suas crises. De entre as razões que justificam o baixo impacto da cirurgia encontra-se o facto de se desconhecer, na maioria dos casos, o foco desta atividade elétrica anormal. Por isso, a deteção deste foco é importante tanto para o diagnóstico como para o controlo das crises.

O foco epiletogénico é um conceito teórico, consistindo na descreve a região cerebral que é necessário remover para deixar o doente livre de crises. Este é caracterizado por dois tipos de atividade epiléptica: a ictal e a interictal. A primeira diz respeito à atividade elétrica gerada durante as crises epiléticas e a segunda à atividade gerada entre as crises. A primeira é caracterizada uma intensa descarga elétrica que pode ter uma duração até alguns minutos. Já a segunda forma de atividade epiletogénica é, normalmente, mais breve no tempo e não associada a manifestações comportamentais detetáveis.

Os métodos atualmente utilizados no diagnóstico da epilepsia baseiam-se quer na deteção da atividade ictal, quer deteção da atividade interictal. Estes incluem a tomografia por emissão de positrões (PET, do inglês *Positron Emission Tomography*), a tomografia computorizada de emissão de fotão único (SPECT, do inglês *Single Photon Emission Computed Tomography*), o magnetoencephalografia (MEG), o eletroencefalografia (EEG), tanto de escalpe como intracraniana, e, por fim, a combinação entre o EEG e a imagiologia por ressonância magnética funcional (fMRI, do inglês *functional Magnetic Resonance Imaging*). Todas estas técnicas possuem diversas limitações: em termos de baixa resolução temporal (PET, SPECT) e espacial (EEG, MEG), utilização de radiação ionizante (PET, SPECT), de carácter invasivo (EEG intracraniano), e, também, pelas dificuldade técnicas e financeiras que advêm da implementação de equipamento (MEG, EEG/fMRI). De forma a ultrapassar algumas destas dificuldades, novos métodos de processamento de dados de fMRI do estado de repouso têm sido desenvolvidos. Estes têm em vista a deteção de atividade epiletogénica interictal.

A partir de estudos recentes em doentes com epilepsia do lobo temporal (TLE, do inglês *Temporal Lobe Epilepsy*) foi elaborada a hipótese de que o foco epiletogénico apresenta um comportamento distinto do restante parênquima cerebral quer em termos de perfil temporal,

quer em termos da complexidade dos seus sinais dependentes do nível de oxigenação do sangue BOLD (do inglês *Blood Oxygen Level Dependent*, designação dada aos sinais provenientes da técnica fMRI). Em particular, diversos estudos de EEG/fMRI sugerem que a atividade interictal está associada a picos transientes nos sinais BOLD, apresentando estes, por conseguinte, um perfil temporal BOLD distinto da restante atividade cerebral. Adicionalmente, estudos recentes com EEG indicam que o tecido epiletogénico apresenta uma menor complexidade, em termos de perfil temporal, que o parênquima saudável.

Com base nestas hipóteses, é possível aplicar uma análise de agregação temporal bi-dimensional (2dTCA, do inglês *bi-dimensional Temporal Clustering Analysis*) para identificar regiões cerebrais que possuam um perfil temporal semelhante. Desta análise espera-se que sejam encontrados diversos conjuntos de regiões com perfis temporais distintos, eventualmente incluindo os potenciais focos epiletogénicos. No entanto, a aplicação desta técnica isoladamente não é suficiente para identificar com segurança o foco da atividade epiletogénica.

Para tal, uma avaliação da complexidade dos sinais BOLD correspondentes a essas mesmas regiões pode ser feita utilizando duas abordagens: uma baseada no nível de entropia do sinal e outra baseada nas propriedades fractais do sinal. Relativamente à primeira abordagem, o método utilizado para avaliar a dinâmica da complexidade foi a análise da entropia à multiescala (MSE, do inglês, *Multiscale Entropy*) desenvolvendo uma variante modificada do algoritmo original. Este baseia-se no cálculo da entropia do sinal BOLD ao longo de múltiplas escalas temporais. Na análise de sinais BOLD de origem epiletogénica postula-se que o tecido possua uma complexidade menor que o restante tecido saudável, possuindo, no geral, uma entropia mais baixa.

Na segunda abordagem, o método utilizado para avaliar as correlações temporais de longo-alcance (LRTC, do inglês *Long Range Temporal Correlations*) ou as propriedades fractais dos sinais BOLD é a análise de flutuações com remoção de tendência (DFA, do inglês *Detrended Fluctuation Analysis*). Este método baseia-se na análise da auto-afinidade do próprio sinal, isto é, analisa as autocorrelações do sinal ao longo das diversas escalas temporais. No caso da análise de sinais BOLD com origem epiletogénica postula-se que as LRTCs sejam mais fortes do que as LRTCs para sinais BOLD de tecido saudável. Isto porque num sinal periódico, como é o caso da atividade interictal, é de esperar observar uma autocorrelação maior do que num sinal com uma periodicidade mais baixa.

Esta combinação metodológica tem como objetivo fornecer um biomarcador para a identificação de tecido epiletogénico a fim de ajudar no diagnóstico, na monitorização e no tratamento da epilepsia.

A demonstração da aplicabilidade desta metodologia na identificação do foco epiletogénico baseou-se na análise de três doentes, cada um com um tipo diferente de epilepsia: epilepsia do lobo temporal unilateral e bilateral e displasia cortical focal (FCDE, do inglês *Focal Cortical Dysplasia Epilepsy*). Em todos os doentes, foi identificada uma região cerebral, cujo sinal BOLD possui um comportamento temporal distinto, concordantes com a informação clínica.

A análise feita aos doentes com epilepsia do lobo temporal identificou a origem da atividade epilética baseada na hipótese que os sinais BOLD do tecido epiletogénico possuem uma entropia menor que o restante parênquima cerebral. A análise de conectividade funcional aos focos encontrados revelou correlações positivas e negativas com outras regiões cerebrais associadas quer a possíveis redes criadas pelo foco epiletogénico, quer a outras redes cerebrais que normalmente aparecem em estudos fMRI de estado de repouso.

Por outro lado, a análise feita ao doente com displasia cortical focal indicou como provável foco epiletogénico uma região cerebral que não corresponde à informação clínica da lesão displásica. No entanto, uma análise da conectividade funcional da região encontrada pelo método indicou que esta possui correlações fortes com a região da lesão. De facto, as hipóteses postuladas neste trabalho baseiam-se em estudos elaborados para pacientes com TLE, pelo que ainda não existe uma assinatura de complexidade associada aos sinais BOLD de origem em FCDE. Por conseguinte, propõe-se como trabalho futuro, um estudo de uma amostra de doentes com FCDE de modo a classificar os sinais BOLD das regiões cerebrais displásicas em termos da entropia (MSE) e das LRTC (DFA).

Os resultados preliminares obtidos neste estudo abrem novas perspetivas para a utilização de dados fMRI no auxílio ao diagnóstico, monitorização e tratamento da epilepsia, principalmente na avaliação pré-cirúrgica. No entanto, existem alguns limites associados à metodologia que precisam ser melhorados. O primeiro diz respeito ao facto dos sinais BOLD variarem consoante os indivíduos estudados, as zonas cerebrais e as condições dos tecidos cerebrais: se são saudáveis ou patológicos. Ou seja, é expectável haver variação da frequência, amplitude e forma destes sinais. Ainda, há estudos que demonstram que a atividade interictal pode produzir tanto um aumento como um decréscimo da magnitude do sinal BOLD, ou até não ter efeito na mesma. Resumindo, cada caso de epilepsia é único e condicionado pelos fatores descritos acima e, portanto, assumir uma resposta homogénea para todos eles torna restrita a aplicabilidade deste

método. Por conseguinte, o método deve ser otimizado para cada indivíduo ou grupo de indivíduos.

Concluindo, tanto quanto me é dado a conhecer, este trabalho foi o primeiro a combinar uma análise de agregação temporal de regiões cerebrais com a análise da complexidade dessas mesmas regiões utilizando dados do estado de repouso de ressonância magnética funcional. Além da contribuição deste trabalho relativamente à sua aplicação à epilepsia, a metodologia desenvolvida é igualmente válida para ser aplicada ao estudo da dinâmica dos sinais BOLD no geral, estudando, por exemplo, redes neuronais de estado de repouso em indivíduos saudáveis em termos do seu comportamento temporal e a nível da sua complexidade.

PALAVRAS-CHAVE

Epilepsia; foco epiletogénico; imagiologia por ressonância magnética funcional; análise de agregação temporal; análise de complexidade.

ABSTRACT

Epilepsy is one of the most important chronic neurological disorders worldwide affecting more than 50 million people of all ages. Among these almost 20% of epilepsy cases are uncontrollable and have an unknown source of this abnormal electrical activity.

The present methods for detection of the epileptogenic foci comprises positron emission tomography, single photon emission computed tomography, magnetoencephalography, electroencephalography (EEG) alone and EEG/functional magnetic resonance imaging (fMRI), all with limitations in terms of temporal and spatial resolutions. In order to overcome some of those limitation a new method using fMRI alone was developed based on the hypotheses that the epileptogenic focus shows Blood Oxygen Level Dependent (BOLD) temporal profiles distinct from the remaining brain parenchyma during interictal activity and that the epileptogenic focus BOLD signals show lower complexity than healthy parenchyma.

Therefore, bi-dimensional temporal clustering analysis (2dTCA), a data-driven technique, was used to identify brain regions with similar temporal profiles. Then, the BOLD signals of these regions were assessed regarding complexity using a modified multiscale entropy algorithm and also detrended fluctuation analysis in order to identify which of those regions corresponded to epileptogenic tissue.

In order to demonstrate the applicability of the developed method a sample of three epileptic patients were analyzed comprising three types of epilepsy: unilateral and bilateral temporal lobe epilepsies, and focal cortical dysplasia. The results showed that this method is able to detect the brain regions associated with epileptogenic tissue. The results also showed that the epileptogenic focus influences the dynamics of related brain networks. This could be a key factor in the applicability of this method to other epilepsy cases.

Finally, new perspectives are envisioned concerning the use of this method in the medical care of epilepsy and in the study of other brain networks.

KEYWORDS

Epilepsy; epileptogenic focus; functional magnetic resonance imaging; temporal clustering analysis; complexity analysis.

CONTENTS

LIST OF FIGURES

LIST OF TABLES

LIST OF ACRONYMS

2dTCA	Two-dimensional Temporal Clustering Analysis
α	Scaling Exponent
AI	Anisotropy Index
BOLD	Blood Oxygen Level Dependent
CI	Complexity Index
dHb	Deoxyhemoglobin
EEG	Electroencephalography
EPI	Echo Planar Imaging
FDG	Fluorodeoxyglucose
fMRI	Functional Magnetic Resonance Imaging
FWER	Family-Wise Error Rate
DFA	Detrended Fluctuation Analysis
DMN	Default Mode Network
GLM	General Linear Model
HRF	Hemodynamic Response Function
ICA	Independent Component Analysis
iEEG	Intracranial Electroencephalography
LRTC	Long-Range Temporal Correlations
MEG	Magnetocencephalography
MSE	Multiscale Entropy Analysis
oHb	Oxyhemoglobin
PET	Positron Emission Tomography
RMS	Root-Mean-Square
ROI	Region-of-Interest
RTC	Reference Time Course

sEEG	Scalp Electroencephalography
SPM	Statistical Parametric Map
SNR	Signal-to-Noise Ratio
TCA	Temporal Clustering Analysis

CHAPTER 1. INTRODUCTION AND OBJECTIVES

Epilepsy is one of the most important chronic neurological disorders worldwide affecting more than 50 million people of all ages. Although 70% of the cases are treatable with anti-epileptic drugs and less than 10% with surgical therapy, the remaining 20% can't control their seizures. This neurological disorder brings an important impact on epileptic patients concerning discrimination, social stigma, and higher national healthcare costs. People with epilepsy can be targets of prejudice and the stigma of the disorder can discourage people from seeking treatment for symptoms and becoming identified with the disorder (WHO 2012).

An epileptic seizure can be defined as a "transient occurrence of signs and/or symptoms due to abnormal excessive or synchronous neuronal activity in the brain" (Fisher et al. 2005). These brief electrical disturbances can have effects on sensory, motor, and autonomic functions, provoke changes in awareness or behavior, loss of consciousness, and convulsions. Uncontrolled epilepsy can also lead to depression, anxiety, and loss of cognitive function (Avanzini et al. 2013).

The epileptogenic zone or focus is a theoretical concept corresponding to the brain volume that needs to be removed to render the patients seizure-free, i.e., it describes the abnormal cortex responsible for the generation of epileptic seizures. Thus, the cessation of seizures is accomplished with the complete resection of this area (Hamandi et al. 2005). This focus is characterized by two types of electrical activity, ictal which means during seizure, and interictal, which mean between seizures. The last one is normally more brief in time and is periodic (Ko et al. 2014).

Hereupon, epileptogenic focus identification is important to epilepsy diagnostic and seizure control. The present methods for this purpose are based on Positron Emission Tomography (PET) and Single Photon Emission Computed Tomography (SPECT) (Mountz 2007; Kim & Mountz 2011), Magnetoencephalography (MEG) (Foley et al. 2014), Electroencephalography (EEG) alone (Hassanpour et al. 2004; Leal et al. 2007; Leal et al. 2008) and EEG/functional Magnetic Resonance Imaging (fMRI) analysis (Leal et al. 2006; Leite et al. 2013; Wang et al. 2012; Hamandi et al. 2005; Thornton et al. 2010). There's a tradeoff in terms of time and spatial resolutions for all these techniques (Fig. 1). The first technique is a direct measure of the Fluorodeoxyglucose (FDG) uptake in the brain based on the hypotheses that the cortical blood flow increases in the area of seizure

discharge (Mountz 2007). The second one works is a similar way, but with a different radiotracer (Tc-99m) (Kim & Mountz 2011). The main limitation of using PET and SPECT to localize the epileptogenic zone relies on specificity of abnormalities due to its limited spatial resolution and poor temporal resolution (Morgan et al. 2004; Clare 1997). Furthermore, the need for a radiotracer is also a drawback, making this technique more invasive.

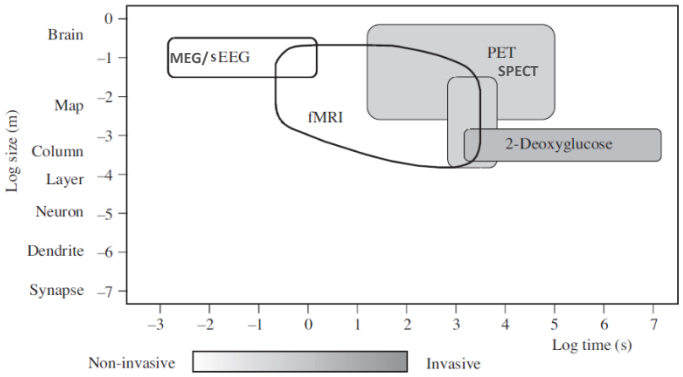

Fig. 1- Relative spatial and temporal sensitivities of different functional brain imaging methods. MEG: magnetoencephalography; sEEG: scalp electroencephalography; fMRI: functional magnetic resonance imaging; PET: positron emission tomography; SPECT: single photon emission computed tomography. Adapted from (Jezzard et al. 2001).

The third and fourth techniques used to localize ictal and interictal electrical activity are MEG and EEG. There are two main modes of using the latter modality, scalp EEG (sEEG) and intracranial EEG (iEEG). Both of these modalities have high temporal resolution, allowing the detection of brief spikes of electric activity, such as interictal activity. However, when regarding the needs of abnormalities' specificity for presurgical assessment, the spatial resolution of sEEG and MEG is poor. In order to improve the resolution of sEEG a high-density of electrodes is needed (Leal et al. 2007; Leal et al. 2008). This issue can be overcome by iEEG, as the electrical signal is recorded directly from cortical tissue. The major drawback of this last modality relies on the fact that it's extremely invasive.

Lastly, simultaneous EEG-fMRI is an emergent technique which combines the best of two modalities, high temporal resolution from EEG and high spatial resolution from fMRI. The strategy followed in this case is to continuously sample the interictal and ictal events while measuring the BOLD signal simultaneously with EEG. This is somewhat cumbersome as it requires a very specific and delicate setup, particularly for acceptable recording of the EEG. Otherwise it will bring several kinds of noise problems, including movements artifacts (Wang et al. 2012), compromising the feasibility of EEG-fMRI studies. Another shortcoming associated with this technique, and with EEG alone, is that they aren't sensitive to interictal epileptiform activity in deep structures making this technique useful only in patients with frequent interictal events recorded from the sEEG (Morgan et al. 2004; Lopes et al. 2012). To overcome some of the limitations described above and find a more suitable solution to localize a seizure onset, efforts are being taken to develop new processing methods using fMRI

technique only (Yee & Gao 2002; Morgan et al. 2004; Hamandi et al. 2005; Morgan et al. 2008; Morgan et al. 2010).

Another approach to epilepsy diagnosis and characterization of epileptic signals behavior has been recently taken on the complexity field. Some authors have been hypothesized that epileptogenic brain tissue has a different complexity than healthy brain tissue (Parish et al. 2004; Monto et al. 2007; Protzner et al. 2010). A complete characterization of this complexity could lead to a definition of a physiological biomarker applicable to epilepsy, namely for diagnostic and monitoring of its treatment. For that purpose two main approaches can be used: a disorder level based (Ouyang et al. 2009; Protzner et al. 2010) or a fractal properties based (Parish et al. 2004; Monto et al. 2007) methods. In both of them it is expected that in the epileptogenic focus the complexity is lower because of its intrinsic periodic interictal electric activity.

This thesis project will focus on the epileptic focus localization through fMRI BOLD signals and then on the complexity analysis of its time series. Therefore, in the next section the concepts inherent to this work will be described.

1.1. BOLD signal origin and fMRI analysis

Functional magnetic resonance imaging (fMRI) is a powerful non-invasive tool that allows the study of the functional responses of the brain in a quantitative way. One advantage of using fMRI is the identification of brain activity due to a stimulus with a high spatial resolution (Jezzard et al. 2001).

This technique is based on the hemodynamic response function (HRF) of the brain, which arises when a given stimulus is applied. The HRF is a transfer function of the neurovascular coupling characteristic of brain activation. When a stimulus acts on a particular region of the brain evokes, in that area, a change in blood flow. This facilitates

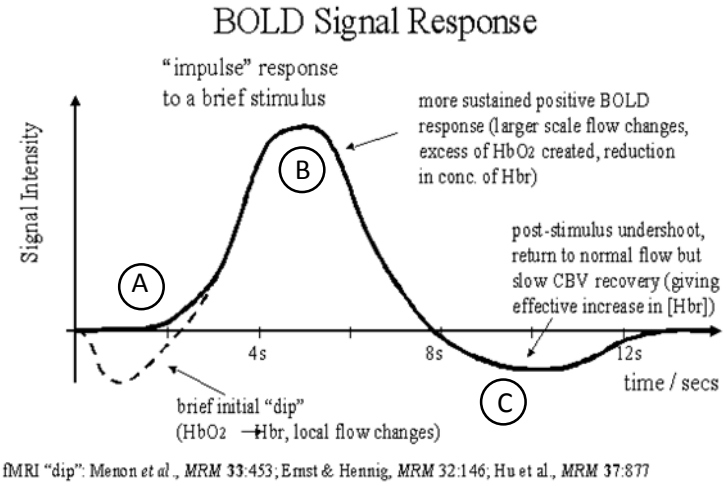

Fig. 2- BOLD Signal Response to a brief stimulus. Adapted from (Jezzard 1999).

glucose oxidation by providing more oxygen molecules. If there is an increased consumption of oxygen, there'll be an increased concentration of deoxyhemoglobin (dHb), a paramagnetic oxygen binding molecule. Oxyhemoglobin (oHb), on the other hand, is a diamagnetic molecule with a magnetic susceptibility smaller than that of dHB (Clare 1997).

Therefore, a change in hemoglobin oxygenation leads to changes in the local distortions of a magnetic field applied, generating local field gradients and local changes of T2* in tissue the blood vessels. The measure of the T2* originate the BOLD signals (Jezzard et al. 2001), see Fig. 2. The brain hemodynamic response can be summarized in the following steps. When a brief stimulus acts, there's an initial decrease of BOLD signal due to increase of oxygen consumption (Fig. 2A). Then, the increased blood flow decreases the dHb concentration increasing the BOLD signal (Fig. 2B). Finally, a delay of the return to the initial blood volume level provokes a decrease of oHb, and a consequently increase of dHb reducing temporally the BOLD signal intensity (Fig. 2C).

The output of fMRI is a set of volumes comprising the scans of the brain at successive times, usually named raw data. Each volume is divided in resolution dependent number of small elements, named voxels, in which the information of the correspondent brain region is stored. One of the goals of acquiring fMRI data is to perform a robust, sensitive, and valid analysis to detect brain regions that show increased signal intensity at the stimulus time. In other words, the aim of fMRI analysis is to identify which voxels have their signal significantly greater than the noise level (Clare 1997; Jezzard et al. 2001). A typical pipeline analysis, schematically represented in Fig. 3, includes a first step of raw data pre-processing that usually includes, correction to time effects and to subject movement during the experiment, and data spatial smoothing to improve the signal to noise ratio. Additional steps, such as, data detrending, filtering and regressing out of nuisance covariates are often taken. The aim of this pre-process is to improve the detection of activation events. Then, a statistical analysis is performed to detect which voxels shows a response to the assessed stimulus. This step usually involves a model estimation, through a general linear model (GLM) based on convolution between the HRF and the stimulus temporal profile. Finally, in order to display the activation images, statistical confidence must be given to the results by inferring about

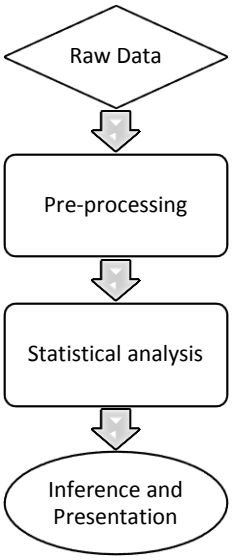

Fig. 3- Steps involved in the processing of fMRI data. Adapted from (Clare 1997).

probability values. See **Appendix A** for more information about statistical analysis, inference and statistical maps presentation in fMRI.

The assessment of a stimulus via a pipeline analysis as described above can be one of two types. The first one comprises a stimulus that has typically few time points of duration, and its analysis is usually named a block-related one. The second one, a transient stimulus with a short duration is used, whereby its analysis is named an event-related one (Josephs et al. 1997). In epilepsy, once the stimulus is usually a transient spike corresponding to interictal electric activity, the analysis described in the above pipeline of event-related type.

Since no technique is free of shortcomings this one has several limitations too. One of them concerns the temporal resolution, which is limited by the profile of the hemodynamic response, and low signal-to-noise ratio (SNR) and contrast-to-noise ratio (CNR), leading to high variance in the results. One way to overcome this last limitation is to repeat the stimuli more than once, decreasing variance in results (Jezzard et al. 2001). However, this is difficult to apply in epilepsy since the timing of the stimulus, interictal or ictal seizure activity, is random and uncontrollable (Morgan et al. 2007).

1.2. Epileptogenic focus localization

As explained before, the timing of ictal and interictal activity in epilepsy is unknown and unpredictable. Therefore, an analysis based on models isn't suitable to localizing the epileptogenic focus, since no assumptions about temporal profile of the stimuli can be made. Data-driven techniques have been developed to deal with such cases as they are model-free. Some examples of such methods are the following: principal component analysis (Sugiura et al. 2004; You et al. 2011), independent component analysis (ICA) (Rodionov et al. 2007), hierarchical clustering (Cordes et al. 2002; Keogh et al. 2005), and fuzzy clustering (Somorjai & Jarmasz 2003; Wahlberg & Lantz 2000). When applied to fMRI datasets these methods result in a large number of components, which are hard to classify without spatial and temporal information (De Martino et al. 2007; Rodionov et al. 2007).

Another data-driven method developed in the past years is temporal clustering analysis (TCA) (Yee & Gao 2002; Gao & Yee 2003; Morgan et al. 2004; Hamandi et al. 2005). This is a one-dimensional algorithm that groups together time series to one single cluster with the same temporal profile based on a given criteria. This criterial could be, for example, the same maximum signal magnitude

timing or the same first signal magnitude increase, to one single cluster. A modification of the original TCA to a bi-dimensional method, two-dimensional temporal clustering analysis (2dTCA) (Morgan et al. 2007; Morgan et al. 2008), detects different BOLD responses, assumed to be from different sources. It allows the detection of more than one single cluster. Once obtained the temporal profile of the cluster, it is possible to perform an event-related fMRI analysis.

In Morgan's work (Morgan et al. 2007; Victoria L Morgan et al. 2008; Morgan et al. 2010) the application of 2dTCA to epileptogenic focus localization is based on the hypothesis that interictal epileptic activity provokes a transient BOLD spike with a rate slower than that of BOLD images acquisition. This hypothesis was based on preview results of EEG-fMRI studies applied to temporal lobe epilepsy (Salek-Haddadi et al. 2006; Kobayashi et al. 2005; Federico et al. 2005; Bagshaw et al. 2004). The main results of these works showed that interictal activity detected by EEG is associated with a BOLD signal change.

1.3. Complexity analysis

The human brain has an inherent high complexity arising from the interaction of thousands of neuronal networks that operates over a wide range of temporal and spatial scales (Hutchison et al. 2013). This enables the brain to adapt to the constantly changing environment and to perform mental functions. In pathologic brains this capacity of adaptation is often impaired, leading to ordered or random patterns of behavior. In case of epilepsy, the study of such complexity could help to understand how an epileptic brain functions.

To assess brain complexity we can only observe the macroscopic output of brain function, such as via EEG and fMRI, where a signal change represents a response from millions of neurons, thus creating the need for robust methods to evaluate the complexity of signal from such techniques. These methods are usually based on one of two approaches: disorder level based or a fractal properties based.

The first one comprises methods that are entropy-based, by quantifying the regularity or orderliness of a time series (Pincus 1991; Kurths et al. 1996; Andino et al. 2000; Richman & Moorman 2000). Entropy can be conceptualized has a measure of the degree of disorder of a given system and increases with the degree of irregularity, reaching its maximum in completely random systems, such as uncorrelated or white noise, and its minimum in completely ordered systems, such as a single

frequency sinusoid. Physiologic outputs usually exhibits a higher degree of entropy under healthy conditions than in a pathological state, as they're characterized by a sustained breakdown of long-range correlations and loss of information (Goldberger et al. 2002). However, an increase in the entropy may not always be associated with an increase in dynamical complexity (Costa et al. 2002). One method that has been developed and improved in the past years and has been shown to effectively quantify the complex dynamics of biological signals is the multiscale entropy (MSE) (Costa et al. 2002). It is based on measuring the entropy over multiple time scales inherent in a time series.

The second approach on brain complexity assessment relies on the evaluation of long-range temporal correlations (LRTC), which reflect the self-affinity of a given signal. The majority of quantifications methods such as spectral analysis and Hurst analysis (Peng et al. 1995) for the LRTC study are invalid to evaluate biological signals because, as they are complex and show fractal properties, their stationarity are not guarantee. Thus, a method capable of detecting the LRTC was developed in the past years to overcame the nonstationary problem of biological signals, named detrended fluctuation analysis (DFA) (Peng et al. 1994).

1.4. Thesis hypotheses and goals

This master thesis project is based on the hypotheses that the epileptogenic focus shows a BOLD signal with a distinct temporal profile from the remaining brain parenchyma, either during ictal and interictal activity (Morgan et al. 2007; Victoria L Morgan et al. 2008; Morgan et al. 2010). Particularly, it is known that the interictal epileptic activity provokes a transient BOLD spike with a rate slower than that of BOLD images acquisition (Salek-Haddadi et al. 2006; Kobayashi et al. 2005; Federico et al. 2005; Bagshaw et al. 2004). This makes possible the application of a method for the localization of the epileptogenic focus, the 2dTCA.

Furthermore, it is well-known, from epileptic EEG signal studies, the periodic behavior of epileptic activity of epileptogenic brain regions (Parish et al. 2004; Monto et al. 2007; Protzner et al. 2010). Indeed, in these EEG studies it was shown that the epileptogenic focus EEG signal shows lower complexity than healthy parenchyma. However, there are no studies showing the same results with epileptic BOLD signals. Therefore, for the purpose of this thesis project it is hypothesized that the epileptogenic focus BOLD signals shows lower complexity than healthy parenchyma. Also, this complexity can be assessed by methods like MSE and DFA.

Summarizing, the innovation of this work is to explore the complexity properties of epileptic BOLD signals through the application of an algorithm that localizes the epileptogenic focus and extracts its BOLD signal. The main aim is to provide a definition of a biomarker for epileptic tissue identification in order to help on the diagnostic, monitoring and treatment of epilepsy.

Hereupon, this thesis project have three main goals. First, the algorithms referred above, the 2dTCA, the MSE, and the DFA, will be implemented in Matlab®[1] language using the commercial software package Matlab® R2014a. All of these methods will be optimized for BOLD signals analysis using simulated data. Second, a study with a sample of epileptic patients will be carried out by first localizing potential epileptogenic foci with 2dTCA and analyzing complexity of its BOLD signal in order to compare with those of healthy brain parenchyma. Third, based on the hypotheses stated above, the most likely epileptogenic focus will be chosen.

[1] The MathWorks Inc., Natick, MA, 2000 (http://www.mathworks.com/)

CHAPTER 2. BI-DIMENSIONAL TEMPORAL CLUSTERING ANALYSIS

2.1. Introduction

TCA was firstly introduced by Liu and colleagues with a pioneer work where this method was used to study the temporal response of the brain after eating (Liu et al. 2000). The problem addressed by this approach was the fact that there's no model assumption that can be taken to estimate which brain regions will be activated after eating, once the activation timing is unknown. This algorithm searches for the maximal response in each voxel's time series converting a four-dimensional data, characterized in terms of space and time, into a simple relationship between the number of voxels reaching maximum signals and the time, named histogram. A concept of brain parcellation that accounts for timing and connectivity was accomplished for the first time with the results of this work.

In order to improve the brain activations timing detection Yee and Gao modified the sensitivity of TCA algorithm basing the method on the integrated signal intensity of a temporal cluster at each time point (Yee & Gao 2002; Gao & Yee 2003) rather than only on the size of a temporal cluster (Liu et al. 2000). In other words, in the modified algorithm a condition is superimposed limiting the maximum signal change allowed to be clustered. The results of Yee and Gao work show that, despite the fact that the modified TCA is more sensitive than the original one, neither of them could detect

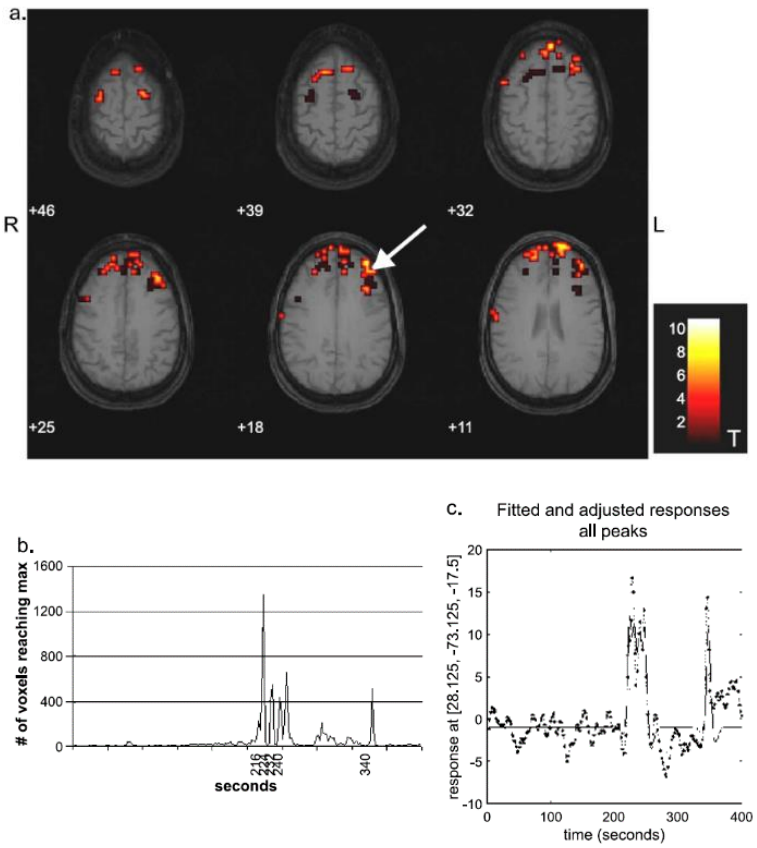

Fig. 4- Results from an epileptic patient with unknown focus localization. **a**: activation map of peaks determined with TCA; **b**: histogram output from TCA; **c**: response of the voxel indicated by the arrow (dotted line) with modeled BOLD response time course (solid line). Adapted from (Morgan et al. 2004).

peaks smaller than the noise level. This opened a window to novel problems, like time shift and movement artifacts, that needed to be addressed before the TCA application.

The application of TCA to epileptogenic focus localization was first addressed by Morgan and colleagues in (Morgan et al. 2004) under the hypothesis that the timing of interictal activity could be determined using TCA on resting fMRI data. Then, activation maps created by event-related fMRI analysis using the discovered discharges timings could be determined to show which brain regions are presumably part of the epileptogenic focus. The result from an epileptic patient with unknown focus localization is shown in Fig. 4. It shows the histogram output from the TCA (Fig. 4b), the results of statistical analysis (Fig. 4a), and fitted and adjusted responses of one voxel pertaining to the found cluster (Fig. 4c). The fact that the TCA defines one single histogram, i.e., one single cluster, implies that voxels spatially distant may be grouped together (as seen in Fig. 4). Whether this detected cluster temporal profile is a representation of the epileptogenic focus or instead a mixture of sources can't be assessed and, therefore, the effectiveness of TCA can't be assessed as well.

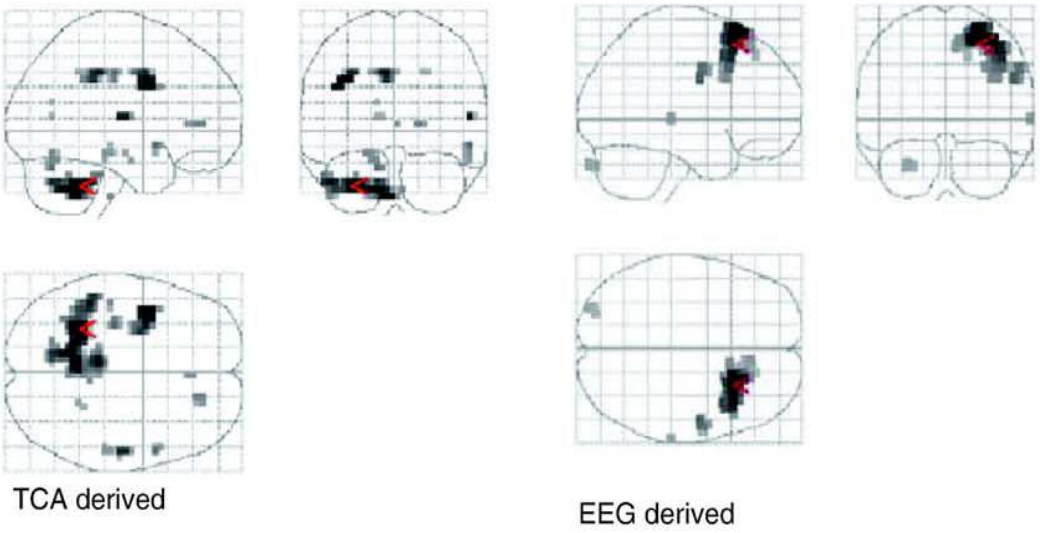

Fig. 5- Statistical maps from a subject with epilepsy obtained with models derived from TCA and from EEG. Adapted from (Hamandi et al. 2005).

Hamandi and colleagues assessed the TCA performance by implementing and evaluating it, as described in (Morgan et al. 2004), using fMRI data acquired with simultaneous EEG in patients with clearly defined focal epilepsy and frequent interictal discharges (Hamandi et al. 2005). They demonstrated that the temporal clusters found were closely correlated with motion events, and not interictal epileptic activity, refuting the validity of using these as onsets in statistical analysis. In order to illustrate this issue, there's a resultant statistical map from an epileptic patient is present

in Fig. 5. It represents the activated brain region found with models in which the onsets were derived either from TCA and EEG. As it can be seen those regions does not match with each other, contrary as expected, suggesting that there may be a confounding with motion events when performing TCA. Hamandi et al. work brought new insights about the limitations of using TCA applied to epilepsy, suggesting that in order to improve this methodology there is the need to primarily separate the noise from the stimuli source and then compare the performance of TCA with other method such as ICA, for example.

Morgan and colleagues posterior work (Morgan et al. 2007; Morgan et al. 2008) brought a new approach to this area by modifying the TCA methodology and overcoming some of the shortcomings described above. They developed a two-dimensional TCA technique addressing the problem of motion and physiological noise by detecting and sorting out separate BOLD responses assumed to be from different sources. This was based on the assumption that BOLD signal changes due to spontaneous interictal activity may be relatively small compared to those of noise, motion, and other activity and are expected to be only slightly slower than the rate of image acquisition (Morgan et al. 2008). Furthermore, as the shape of this BOLD signal response is well known it allows the application of the 2dTCA.

Briefly, in Fig. 6 is depicted a graphical representation of how 2dTCA works and a comparison with TCA. The 2dTCA algorithm will construct a bi-dimensional histogram where columns represent temporal clusters with different temporal profiles. The criterion of grouping time series to different clusters is based on the first time point at which the first signal increase occur, instead of grouping with maximum signal criteria (Liu et al. 2000; Yee & Gao 2002; Gao & Yee 2003; Morgan et al. 2004; Hamandi et al. 2005). This assumes that different sources of activation will not have overlapping timing of BOLD response at the beginning of the time series, which is not proven to be in that way. Supposing that in a functional dataset there are four voxels' time series with different temporal profiles (Vox 1 to 4 in Fig. 6), using 2dTCA Vox 1 and 2 were grouped together in the same histogram column, representing a reference time course of one cluster. On the other hand Vox 3 and 4 will be are grouped together in another column, representing another and independent reference time course of a different cluster. If, for example, one group of voxels represent an epileptogenic focus and another a noising source, such as movement, this algorithm could rule out the latter by sorting different sources in different clusters. If a TCA approach were taken, all the voxel's time courses would be grouped together leading to the identification of brain regions that aren't related to epileptogenic tissue, similar to what was described in (Hamandi et al. 2005), see Fig. 5.

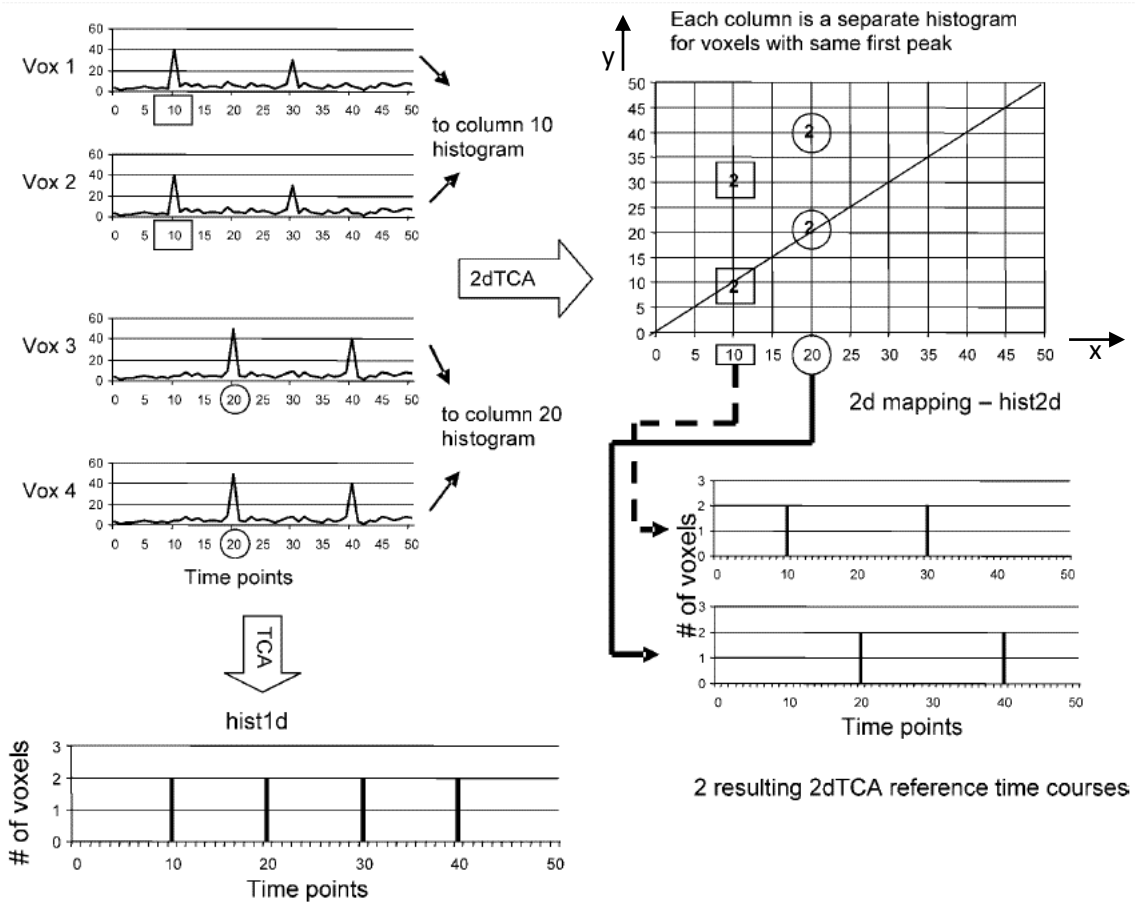

Fig. 6- Graphical depiction of the TCA and 2dTCA algorithms showing how multiple reference time courses are created by the 2dTCA algorithm when multiple different voxel time courses are present in the data (Morgan et al. 2008). x represents the time point at which the voxel's time series is maximum. y represents the time point at which occurs a significant signal increase on the time series.

In Morgan and colleagues' work (Victoria L Morgan et al. 2008), the performance of 2dTCA was assessed, in terms of specificity and sensitivity, by comparing it with the performance of TCA and ICA applied to the same simulated data, where a well-known activations were defined (Morgan et al. 2008). The results showed that 2dTCA algorithm can detect more than one independent reference time course, or equivalently more than one temporal cluster, more effectively than TCA, but slightly less effectively than ICA. However, they argued that as the 2dTCA algorithm will cluster only transient spikes, while decreasing sensitivity to signals of other temporal characteristics, the large number of components determined with ICA would make it difficult to determine the components of interest in vivo when the activation regions are not known. This confirms the advantage of using the 2dTCA as a data-driven for identifying the epileptogenic focus.

As a final remark about the application of 2dTCA on healthy subjects and epileptic patients, more recent work have demonstrated that this algorithm can also be used to detects clusters associated with the default-mode network (DMN) (Morgan et al. 2007; Morgan et al. 2008; Morgan et al. 2010; Pizarro et al. 2012) in healthy (Cauda et al. 2010; Fox et al. 2005)and epileptic subjects and with specific regions, such as the visual, auditory, and motor cortices, through external stimuli with known timing (Morgan & Gore 2009).

2.2. Materials and Methods

2.2.1. Simulated Dataset Characterization

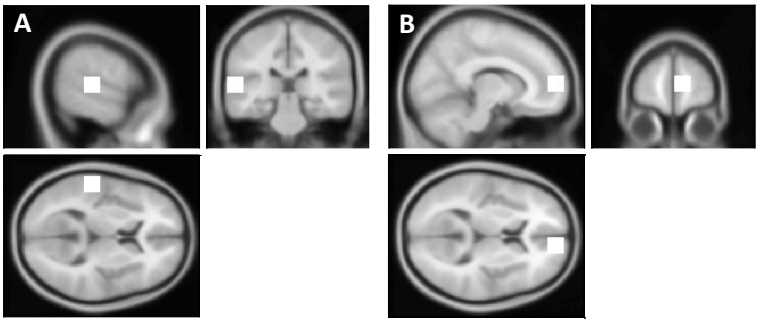

Fig. 7- Depiction of the two regions in which the epileptic activity was simulated. **A)** 216 voxels cubic regions located at the left temporal lobe. **B)** 216 voxels cubic regions located at right frontal lobe. In each frame, **A)** and **B)**, the top left, top right, and bottom left images represent a sagittal, coronal and transverse view, respectively.

A simulated dataset was created, according to the pipeline presented in (Khatamian et al. 2011), from a preprocessed rest fMRI healthy subject scan (see Appendix B for more details of this subject data acquisition) by adding simulated BOLD signals in order to create simulated epileptic activity. For this purpose two regions of interest (ROI) were defined (see Fig. 7), one in the left temporal lobe (LTL) and the other in the right frontal lobe (RFL), to which simulated epileptic activity was added. BOLD signals representing this type of activity were created by convolving the HRF with a spike train containing the timing of each event (see Fig. 8) and added to the BOLD signal already presented in each ROI. The final goal was to obtain simulated data with all combinations of the following characteristics: 5 and 10 spikes randomly distributed in time, correspondent to LTL and RFL ROIs, respectively; simulated activation amplitudes of 0.5 to 2% in increments of 0.25%; and ROI's size of 27, 64, 125, and 216 voxels. Within a ROI the activation frequency and amplitude is homogenous. Each simulation was repeated two times resulting in a total of 56 simulated datasets.

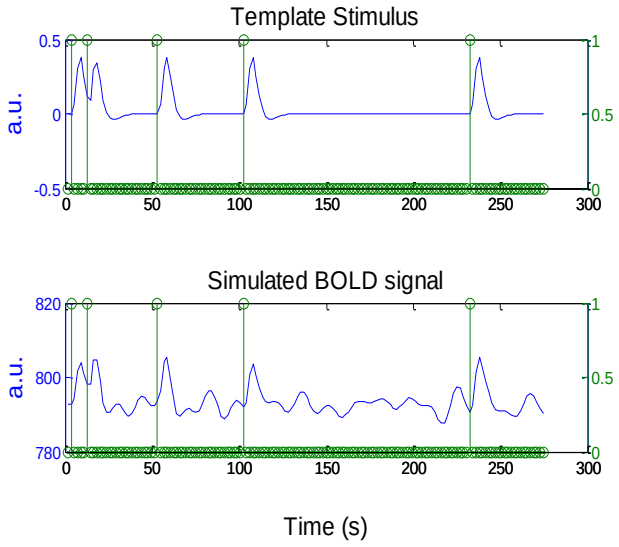

Fig. 8- BOLD signal created by the convolution of the HRF with a spike train containing the timing of each event (**Top**) and its addition to the BOLD signal already presented in the real data (**Bottom**).

2.2.2. Algorithm implementation

The 2dTCA algorithm implemented in this thesis project is based mainly on (Morgan et al., 2008) work with some modified steps based on (Khatamian et al. 2011) and another additional original steps.

fMRI Data pre-processing

Concerning fMRI data, some pre-processing steps are expected before the beginning of the 2dTCA algorithm itself. Namely, slice timing correction for effects due to interleaved acquisition, realignment for correction of motion effects, spatial smoothing, detrending (an additional step not performed in (Morgan et al. 2008; Khatamian et al. 2011)), and temporal filtering. The type of filter used in this last step was a bandpass filter containing the frequencies expected in BOLD response (Glover 1999), instead of a 3-point averaging filter used in (Morgan et al. 2008).

Data transformation

Each functional data series was formatted into *M* one-dimensional arrays corresponding to the *M* analyzed voxels of the dataset. In other words, each array contained the voxel's time series with *N* time points, given by the number of volumes of each raw data. The next steps were performed on this data.

Baseline definition and percent change computation

A definition of the baseline value as the average of the first 5 time points of the voxel's time course as in (Morgan et al. 2008), implies an assumption that the subject is at baseline during that time, which may not be true. Therefore, a *k*-means technique was used such that each voxel's time series was separated into three clusters: one with high values, another with low values, and the last one with the remaining middle values, see Fig. 9 . This differs from the two clusters used in (Khatamian et al. 2011) whereas it was assumed that the BOLD response can represent an activation, an increase in amplitude, or a deactivation, a decrease in amplitude (Pittau et al. 2013). Thus, once we want the baseline of the signal without activation, the mean of the middle cluster was used to estimate the baseline.

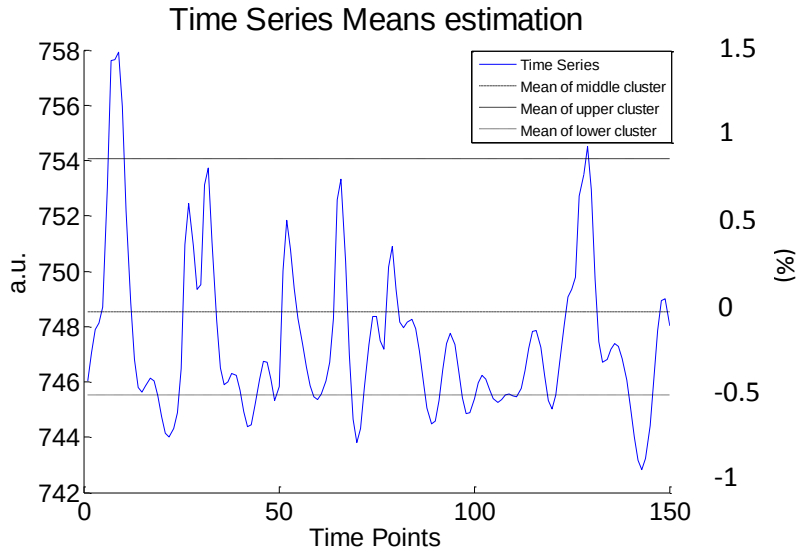

Fig. 9- Example of the three baselines (one corresponding to the mean of each cluster) estimated from *k*-means technique. The scale at the right represents the percentage signal change computed with the baseline corresponding to the mean of the middle cluster.

The percent signal change was then determined according to Eq. 1.

$$\boldsymbol{Percent\ change}\ (\%) = \frac{\boldsymbol{data - baseline}}{\boldsymbol{baseline}} \times \mathbf{100}\ (\%) \qquad \textbf{Eq. 1}$$

The remaining analysis was performed on this percent change data.

Candidate voxels selection

All voxels expected to contain BOLD responses to spikes were identified. For this purpose, two types of limits were defined: one related to the range within which the maximum BOLD signal is allowed to change and another corresponding do the classification of a spike as a transient spike.

For the first one, lower boundaries of maximum signal change from 0 to 2 % in increments of 0.5 % and upper boundaries of minimum signal change from 3 to 11 % in increments of 1 % were tested on the simulated dataset. The goal of this test is to find the best combination of boundaries that allows the selection of a maximum BOLD signal change of interest, but rejects the maximum signal changes due to other sources, such as noise artefacts.

For the second one, the test were run for thresholds in the range of 0 to 2 standard deviations above the baseline in increments of 0.5. The most suitable set of parameters were chosen as that which gives the minimum average false positive rate (FPR), i.e., the best average specificity, across all simulated data with an average true positive rate (TPR), i.e., average sensitivity, greater than 0.9, a method similar to that used in (Khatamian et al. 2011). This limits were found to be 0.5 and 3 % as lower and upper boundaries, respectively, and 2 standard deviations above the baseline as the threshold for transient spike classification, see Fig. 10, with a TPR equal to 0.98 and a correspondent FPR equal to 0.59 and an area under the curve equal to 0.62.

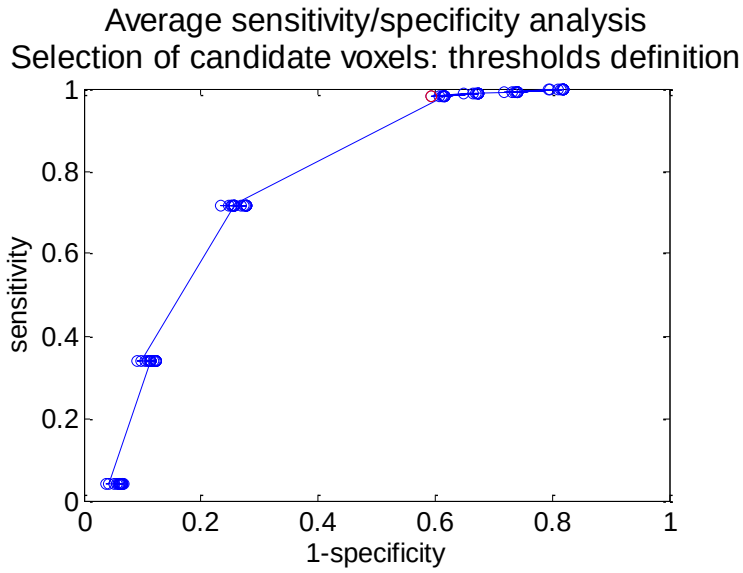

Fig. 10- Average sensitivity/specificity analysis for thresholds definition of candidate voxels selection step. Keeping the average sensitivity above 90 %, the best average specificity (red circle) was found for up and low boundaries of 3 and 0.5%, respectively, and a threshold of 2 standard deviations above the baseline with a TPR equal to 0.98 and a correspondent FPR equal to 0.59. The area under the curve is equal to 0.62.

Hereupon, if a voxel maximum signal change value was within that limits, the voxel was considered for cluster analysis. Otherwise the voxel was considered as a global one if its maximum signal change was under the lower signal change boundary or excluded of the analysis if its maximum signal

change was above the upper signal change boundary. Next, a global time course was determined as the average of all global voxels and regressed out of data.

Event detection and 2D histogram mapping

A two-dimensional map, *hist2d*, was created in an *N* by *N* matrix by incrementing the values in the following manner for all *M* voxels. For each time point:

$$\boldsymbol{hist2d}(\boldsymbol{x},\boldsymbol{y}) = \begin{cases} \boldsymbol{hist2d}(\boldsymbol{x},\boldsymbol{y}) + \boldsymbol{1}, & \boldsymbol{if\ M_i}(\boldsymbol{y}) \geq \boldsymbol{threshold} \\ \boldsymbol{hist2d}(\boldsymbol{x},\boldsymbol{y}) + \boldsymbol{0}, & \boldsymbol{if\ M_i}(\boldsymbol{y}) < \boldsymbol{threshold} \end{cases} \quad \textbf{Eq. 2}$$

where *threshold* corresponds to the limit at which an event is considered to occur in that M_i voxel's time course and is equal to 2 standard deviations above the baseline of that voxel; and *x* is equal to the time point *y* at which the voxel's time series is maximum. Therefore, the *x*-axis of *hist2d* is the time of the maximum signal increase and the *y*-axis is the time at each significant signal increase of the time series.

The result of this 2D histogram consisted of columns that represents individual histograms of significant increases for those voxels whose maximum signal increase occurred at time point *x* (see Fig. 6). These histograms were named reference time courses (RTCs).

RTCs number reduction and its normalization

After the 2D histogram filling a very important step was to analyze which RTCs are truly unique, i.e., which ones describe activity temporally distinct from each other. Voxels can have temporal behaviors closely similar, but with slight variations in their time courses that could lead to different peak timings. Therefore, the number of RTCs were reduced in two steps.

First, a correlation coefficient was computed between each pair of RTCs in order to compare the time course of all RTCs to one another and those with a value above a given threshold are summed.

The second step of grouping RTCs was performed by comparing their activity and by grouping those that share activity in time at a given percentage. As shown in Fig. 11, first, the mean of each RTC's time course was defined as a threshold above which the RTC is considered to have a spike of activation (see corresponding whitelists in Fig. 11B). Second the amount of shared activity between the two RTCs was computed and if this value were equal or above a given percentage, the RTCs were summed.

To test which threshold value (of the first step) and percentage (for the second step) are the best, a range from 0.1 to 0.9 in increments of 0.2 and 10 to 90 % in increments of 20 % were tested on the simulated data, respectively. The performance of each threshold was evaluated by analyzing each RTC's *t*-map, thresholded at *t*>3.1, (see ***t-maps* creation**) individually, choosing the two ones which best describe the two ROIs (the regions where simulated epileptic activity was created), and computing the correspondent TPR as the ratio between the number of voxels activated in the ROIs and the size, in voxels, of those. The best set of parameters was chosen as that which gives the lower number of resulting RTCs, i.e., groups together more RTCs, with a reasonable average TPR, a criterion similar to that used in (Khatamian et al. 2011). This average is simply the mean of the TPR of all simulated data.

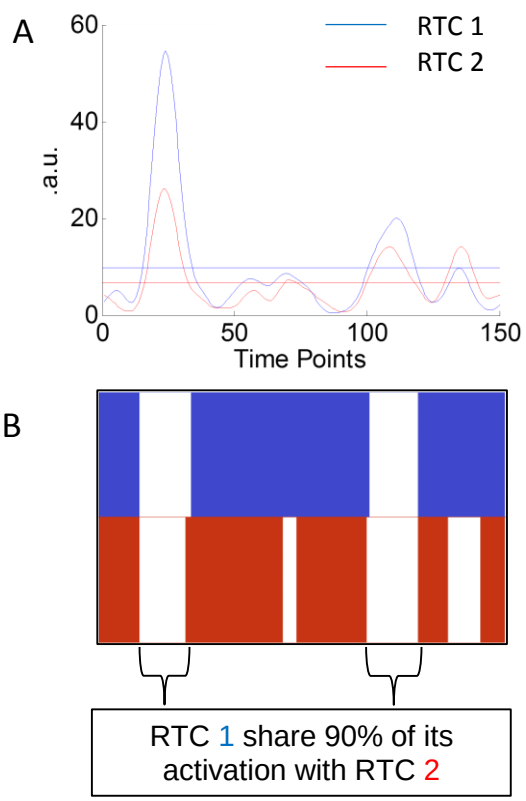

Fig. 11- Illustration of the second step of grouping RTCs. It is based on the percentage of shared activity between two RTCs. **A:** Temporal profile of two hypothetic RTCs. **B:** binary representation of each RTC spike above the mean, where the white color represents activations.

Hereupon, as the first step was independent from the second one, the correlation coefficient threshold was firstly defined. The analysis, shown in Fig. 12, demonstrate that the sensitivity reaches its maximum for a threshold of 0.7 with an average TPR and a corresponding FPR of 0.52 and 0.06, respectively, and an average of RTCs number of 19, then it starts to decline. Regarding the second step threshold, it was defined by fixing the first parameter equal to the best value found, i.e., 0.7, as this steps follows the first in the algorithm. The results showed that after performing the correlation coefficient grouping step, the influence of the second step in the results is negligible, i.e., the number of resultant RTCs as well as the TPR remains similar to that values corresponding to a correlation coefficient threshold of 0.7. Therefore, the limit chosen for the second grouping step was 0.7 with an average TPR and a corresponding FPR 0.06, respectively, of 0.52 and an average of RTCs number of 19, as it performs the highest grouping of RTCs with a similar sensitivity as that for the first step.

Once the final RTCs are defined, they were normalized by subtracting their mean and dividing by their standard deviation.

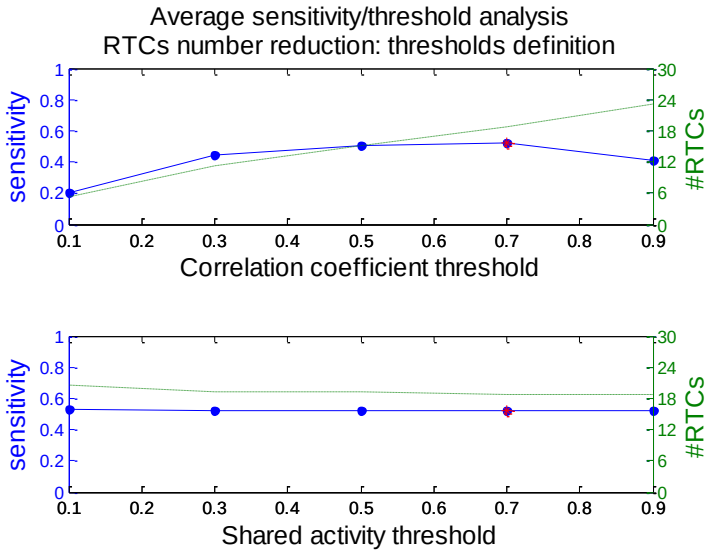

Fig. 12- Average sensitivity/#RTCs analysis for correlation coefficient (**Top**) and shared activity (**Bottom**) threshold definition of RTC grouping step. Optimal parameters for correlation coefficient and shared activity threshold were both defined as 0.7 with a correspondent average TPR and FPR and an average of RTCs number of 0.52, 0.0632 and 18.8 for the first threshold and 0.518, 0.0628 and 18.9 for the second threshold, respectively.

t-*maps creation*

The RTCs were finally passed, along with the nuisance variables (the global time course and motion correction parameters), as regressors to the GLM. In order to obtain the correspondent *t*-maps all regressors were incorporated as contrasts and tested for individual effect (see **Appendix A** for more details). This processing step was performed with the software package SPM[2].

2.2.3. Performance analysis of simulated dataset: sensitivity analysis

Once all thresholds were defined it was important to assess the performance of each simulated dataset in order to determine the most suitable epileptogenic BOLD activity characteristics for 2dTCA input. This evaluation was accomplished by running the 2dTCA algorithm to each simulated data (see **2.2.1 Simulated Dataset Characterization**) using the parameters defined above and computing the average TPR and FPR for each case in a similar way as in **2.2.2 Algorithm implementation - *RTCs number reduction and its normalization***.

[2] Statistical Parametric Mapping (http://www.fil.ion.ucl.ac.uk/spm/)

2.3. Results

The Fig. 13 shows the results of the TPR/FPR analysis to assess the performance of the 2dTCA algorithm in detecting the several forms of simulated epileptic activity. The top and bottom rows of the figure show the following TPR and FPR values for simulated epileptic activity with 5 and 10 spikes, respectively, information of the size of the ROIs and the HRF amplitude above the baseline.

By inspection of the TPR images, it is observed that the TPR values have a tendency to increase towards the increase of both the ROIs sizes and HRF amplitude. Although there are some cases with low TPR value at high ROI size and HRF amplitude (5 spikes: 64 voxels /1.5 % and 125 voxels/1.25 %; 10 spikes: 27 voxels/2 %, 64 voxels/1.25 %, and 216 voxels/2 %). On the other hand, the FPR images show values lower than 0.12 for all cases.

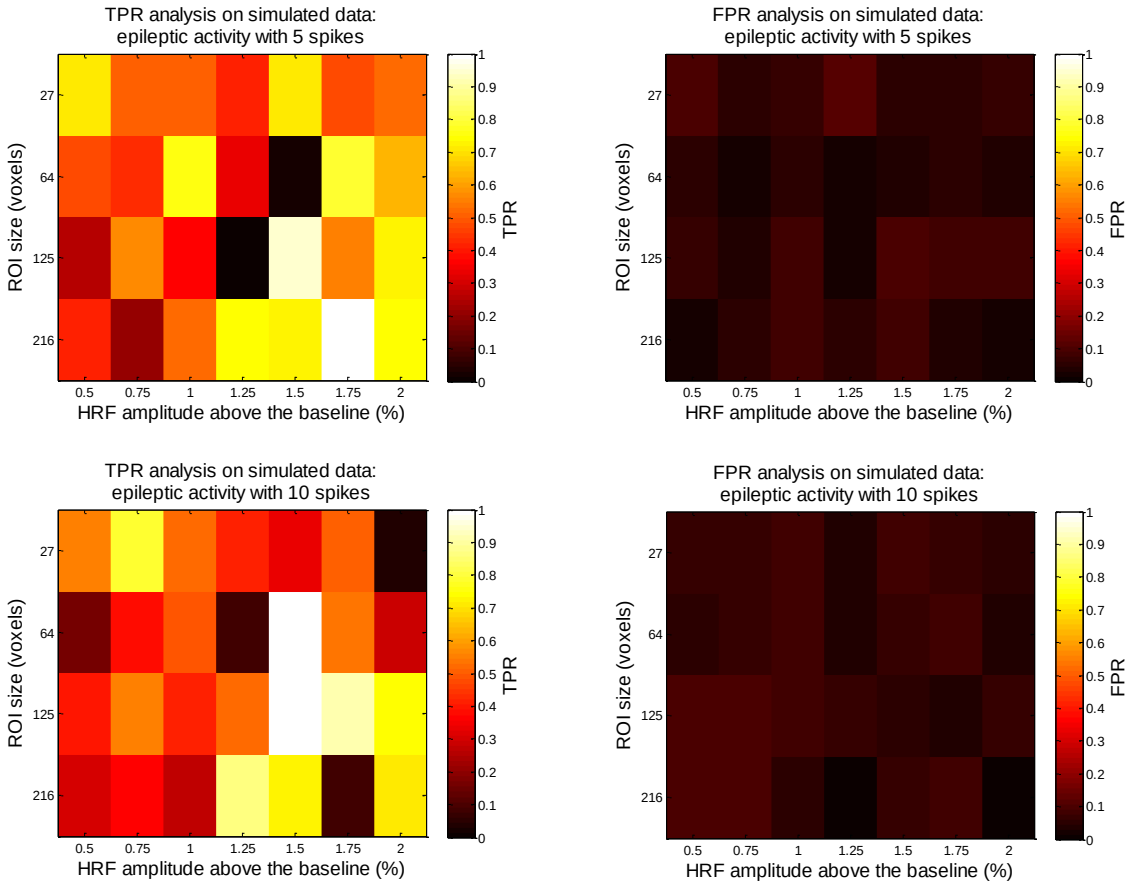

Fig. 13- TPR (**left column**)/FPR (**right column**) analysis on simulated data among ROIs size and HRF amplitude above the baseline. **Top row:** simulated epileptic activity with 5 spikes. **Bottom row:** simulated epileptic activity with 10 spikes.

2.4. Discussion

This chapter describes a data-driven method that allows the detection of different temporal patterns of transient BOLD activation in a single dataset. It has the advantage of being able to detect this type of activity even in deep brain structures with a high spatial resolution.

The results shown in Fig. 13 demonstrate that there is a higher probability of detecting epileptic activity if the HRF amplitude above the baseline is higher than 1.25%, i.e., there are more cases with high TPR when their epileptic activity have an HRF amplitude greater than 1.25%. The same line of reasoning is valid for the ROIs size. The lack of consistency observed for the cases that have a TPR close to zero can be justified by the following facts.

First, the simulated epileptic activity was added to BOLD activity already presented in the healthy subject data. As analyzed in **2.2.2 Algorithm implementation - *Candidate voxels selection*** the thresholds for the selection of potential candidate voxels were defined for an average sensitivity, or TPR, greater than 0.9, meaning that almost all of voxels with the simulated activity of interest were selected. After the selection of the voxels of interest, those that do not have activity of interest are used to calculate the global time course that is, then, regressed out from all the time course's voxels. This step is a critical one since it can induce a negative bias on the time course's voxels reducing the simulated HRF amplitude initially added to the data. Also, the spikes of epileptic activity are added with randomly chosen timing. This can justify the fact that some cases have their simulated epileptic activity masked by this global activity decreasing the overall TPR value. It is also important to note that independently of the TPR value the average FPR is lower than 0.12 for all cases, indicating that the *t*-maps chosen for each case do not describe substantial activation out of the ROIs boundaries. Finally, this inconsistency in the results does not allows to infer about the best frequency of stimuli in order to have a higher TPR.

Second, an issue related to 2dTCA algorithm concerns the assumption that RTCs represent different sources of activation that do not have overlapping temporal profiles of activation. This means that it is assumed that two time series whose maximum signal change occurs at the same time, have the remaining temporal profile with similar shape. Therefore, concerning the results on Fig. 13, as the simulated spikes are attributed to BOLD activity at random, if the maximum signal change of this simulated data has the same timing as other sources of activation then the simulated data will be masked.

Nevertheless, it can be state that in order to have an increased likelihood of detecting BOLD epileptic activity it is desirable that the correspondent HRF has an amplitude greater than 1.25%.

One issue concerning real data studies is related to epileptogenic HRFs when the noise level on the time series is high. In that cases if that response has a low amplitude, the noise will mask it because the algorithm will only map to the bi-dimensional histogram signal increases which are 2 standard deviations above the baseline. Also, in these circumstances the noise amplitude may precede the HRF amplitude. This issue is even more critical with MRI scanners with low magnetic field strengths due to smaller SNRs (Yang et al. 2012).

Another disadvantage of the 2dTCA is that usually a large number of RTCs are obtained and some may result in *t*-maps with significant brain activations not related to epileptic activity. Hence, in real data studies, without some *a priori* knowledge about the localization of the epileptogenic focus it is difficult to select the right *t*-maps. It is therefore important to follow strategies to classify, even in a qualitatively way, the obtained maps with significant activation. An example of an exclusion criterion it's based on common known networks that usually appear on resting-state data, as the Default Mode Network and Visual Network on healthy (Fox et al. 2005; Cauda et al. 2010) and epileptic patients (Victoria L Morgan et al. 2008; Morgan et al. 2010; Morgan et al. 2007). Another way to exclude non-interesting maps is to delimit the statistical analysis to brain regions which are suspected to allocate the epileptogenic focus (clinical information).

CHAPTER 3. MULTISCALE ENTROPY

3.1. Introduction

The early work on complexity analysis of physiological time series were based on entropy algorithms (Andino et al. 2000; Richman & Moorman 2000), which quantifies the regularity of a time series. However, the relationship between the increase or decrease of entropy and low or high regularity of a given time series is not always straightforward. For example, if a certain pathology is associated with erratic fluctuations with statistical properties similar to uncorrelated noise, the assigned value of entropy to that system is high compared to a healthy system with correlated noise (Costa et al. 2002). This is contra intuitive once it is expected that a healthy system has a higher entropy than a pathologic system (Goldberger et al. 2002). The justification for this inconsistency could be in the fact that these entropy algorithms are based on single-scale analysis and do not take into account the complex temporal fluctuations inherent in healthy and pathologic physiologic systems (Costa et al. 2002).

Therefore, in order to respond to this shortcoming, a new method was developed taking into account multiple time scales of analyzed time series, named multiscale entropy (MSE) analysis (Costa et al. 2002; Costa et al. 2005). This method is based on the hypothesis that the ability of a biological system to adapt and function on constantly changing environment is a reflection of its own multiscale complexity. Hence, a reduction of this adaptive capacity, caused by disease states, would be associated with a loss of complexity.

The procedures involved in calculating MSE can be summarized in the following steps (Costa et al. 2005). First, a coarse-grained time series is constructed according to a scale factor, as represented in Fig. 14. The length of each coarse-grained time series is equal to the length of the original time series divided by the scale factor. Second, for each coarse-grained time series a measure of sample entropy is done. The sample entropy is a regularity statistic which searches for patterns in a time series and quantifies its degree of predictability. Thus, it can be defined by the negative natural logarithm of the conditional probability that a dataset of length *N*,

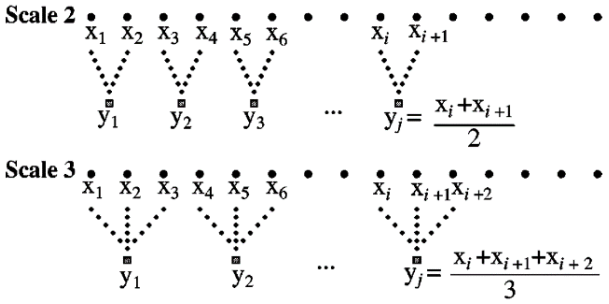

Fig. 14- Schematic illustration of the coarse-graining procedure (Costa et al. 2005).

having repeated itself within a tolerance *r* (similarity factor) for *m* points (pattern length), also repeats itself for *m+1* points, without allowing self-matches (Richman & Moorman 2000). Finally, the sample entropy profile is examined over a range of scales (Costa et al. 2005).

In Fig. 15 is represented a MSE analysis (Bottom) to simulated white and colored (1/f) noises (Top). As shown the entropy value for the coarse-grained 1/f series remains almost constant for all scales, while for the coarse-grained white noise time series monotonically decreases. This is consistent with the fact that 1/f noise contains complex structures across multiple scales (Zhang 1991). Therefore, the statistical properties of fluctuations are different in each scale since new information is revealed in all of them (Costa et al. 2005).

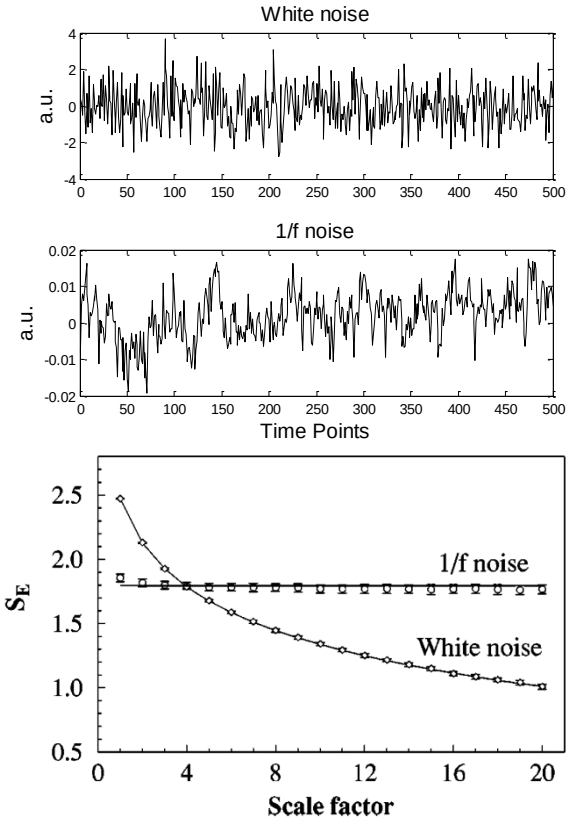

Fig. 15- Top: Simulated white and 1/f noises. **Bottom:** MSE analysis of simulated white and 1/f noise time series. Adapted from (Costa et al. 2005).

Despite all the advantages described above, this technique has several limitations that need to be taken into account. To provide reliable statistics for the entropy measure on each scale the length of the original time-series must be large enough, about 10^m to 20^m (Richman & Moorman 2000). This length definition is dependent on the level of accepted uncertainty. When dealing with EEG time series this limitation is not so restricted once typical length data reaches thousands of time points. However, with BOLD time series, which typically have between 100 and 300 time points, this issue could be an aggravating factor, limiting the factor scale to a low value. For example, if the length of a time series is 100 time points than at a scale factor of 20 we have a coarse-grained time series with only 5 points, restricting the possible choices for *m* (pattern length) and *r* (similarity factor) parameters and, therefore, making the sample entropy estimation unreliable. Thus, a carefully examination on these parameters values are of extreme importance.

Studies on EEG signals have examined the use of several parameter values, such as *m=1* and *r=0.25* (Escudero et al. 2006), *m=2* and *r=0.15* (Catarino et al. 2011), *m=2* and *r=0.20* (Mizuno et al. 2010;

Takahashi et al. 2009; Takahashi et al. 2010), and *m=2* and *r=0.50* (McIntosh et al. 2013), while studies on BOLD signals have found their optimal parameters values as *m=1,2 or 3* and *r=0.15* (Ferreira, Rocha, et al. 2012; Ferreira et al. 2013) and *m=1* and *r=0.35* (Yang, Huang, et al. 2013). The present methods used to evaluate this optimization are based on empirical approaches (Yang et al. 2013; Yang et al. 2013b), demonstrating that there's no guidelines for optimizing these parameters values. Hereupon, the interpretation of the MSE analysis output from BOLD signals must be careful by taking into account the following aspects: the low time series length, which limits the choice of scale factors; and the sampling rate for multislice acquisitions, since the influence from respiration and cardiovascular hemodynamics can't be totally excluded with the typically used sampling rates (TR ≈ 2s) in fMRI (Lowe et al. 1998).

Concerning the application of MSE analysis specifically to epilepsy, Ouyang and colleagues showed that EEG signals of rats are more complex in seizure-free state than in seizure state by performing a MSE analysis in epileptic rats (Ouyang et al. 2009). They demonstrated that the MSE method is able to classify epileptic EEG signals. Another study on human brain's MSE analysis was conducted by Protzner and colleagues in (Protzner et al. 2010). They compared the epileptic and healthy hippocampi's signal complexity through MSE analysis on iEEG signals based on the hypothesis that patients with epilepsy have reduced variability on epileptogenic tissue. Consequently, it was expected that the epileptogenic hippocampus showed lower MSE values than the healthy hippocampus. The results suggested that the brain signal variability could be a robust biomarker of neuronal system integrity in patients with epilepsy. Finally, to the best of my knowledge there are no studies that applied MSE analysis to epileptic BOLD signals.

3.2. Materials and Methods

The MSE method implemented in this project is a modified version of the original approach of (Costa et al. 2002). Throughout this section, the steps of the former, as well as, of the main differences between the two approaches are explained in detail. The algorithm of the original approach can be found at PhysioNet[3] (Goldberger et al. 2000).

[3] PhysioNet: MSE original approach algorithm (http://www.physionet.org/physiotools/mse/tutorial/)

3.2.1. Modified MSE: Algorithm implementation

Time-series coarse-graining

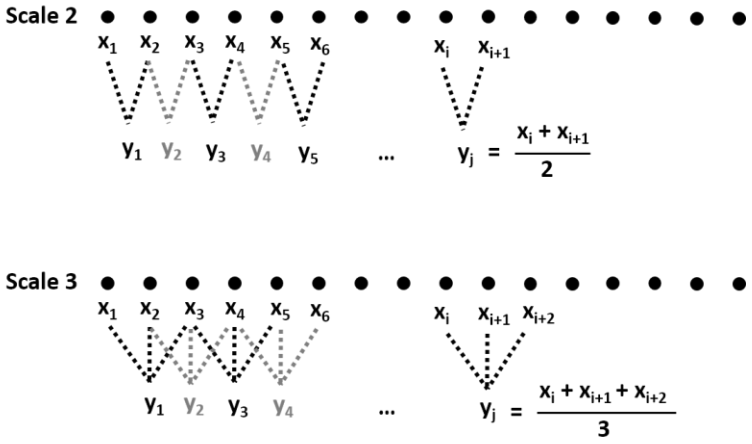

Fig. 16- Schematic illustration of the modified coarse-graining procedure where a moving average is applied to the original time-series for each scale factor. Adapted from (Costa et al. 2005).

This algorithm bases its analysis on one-dimensional time-series and the first step is to perform a coarse-graining of the original data. The original approach, see **2.1 Introduction**, of (Costa et al. 2002) is limited for short time-series, such as the case of typical BOLD time series, since the reliability of statistics required for the sample entropy computation (see **Sample entropy computation**) is severely compromised as the time series are further coarse-grained and consequently shorter. In order to overcome this shortcoming a new approach was developed (Tavares, Santos-Ribeiro, and Ferreira, unpublished results). Like in the original method, a set of coarse-grained time series were created using a moving average of scale factor τ time points, as represented in Fig. 16. Each point y_j in the new time series was obtained through Eq. 3.

$$\boldsymbol{y_j^{(\tau)} = \frac{\sum_{i=j}^{j+\tau-1} x_i}{\tau}, \quad 1 \leq j \leq N - \tau + 1} \qquad \textbf{Eq. 3}$$

where x_i represents the point i of the original time series, of length N, and τ the scale factor. The total length of each coarse-grained time series is given by $\boldsymbol{N - \tau + 1}$**.** With this approach it was guaranteed a larger number of scales in which the sample entropy computation was provided by reliable statistics.

Sample entropy computation

Once the coarse-graining process was completed the next step was to compute the sample entropy for each coarse-grained time series. An illustration of how this was accomplished is represented in

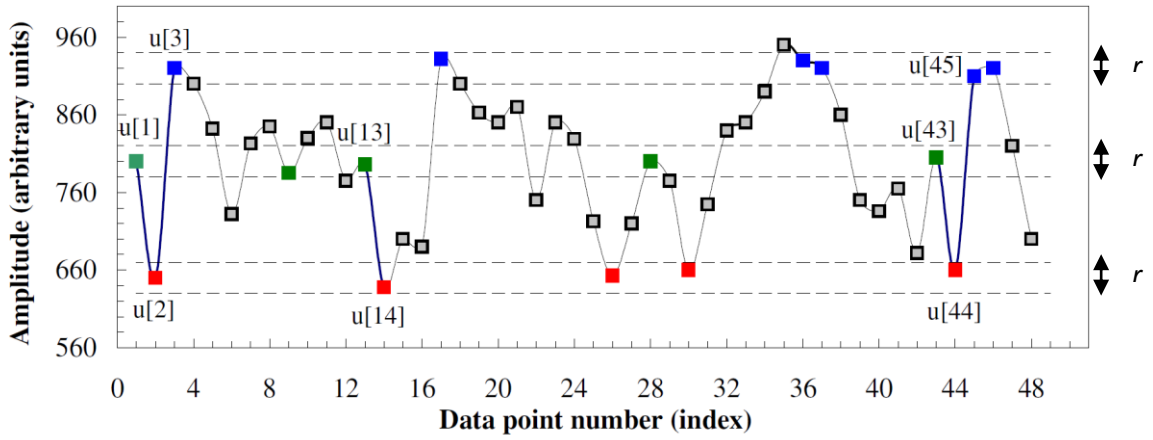

Fig. 17- Illustration of sample entropy computation. In this example, the pattern length *m* and the tolerance *r* are 2 and 20, respectively. Dotted horizontal lines around data points u[1], u[2] and u[3] represent u[1] ± r, u[2] ± r, and u[3] ± r, respectively. All green, red, and blue, points represent data points that match the data point u[1], u[2], and u[3], respectively. Adapted from (Costa et al. 2005).

Fig. 17. Considering a time series, *u*, the algorithm first defines a pattern of length *m*, defined by the user, and another of length *m+1*. Then, it searches for forward repetitions of each pattern in the time series and retain their number into two variables, *A* and *B*, for *m+1* and *m* pattern length, respectively. A pattern is considered to match the template if the absolute difference between all its elements is within a tolerance *r*. Thus, for the example depicted in Fig. 17, considering the pattern of length *m*=2 (green u[1] – red u[2]) and the correspondent pattern of length *m+1*=3 (green u[1] – red u[2] – blue u[3]), the number of repetitions for each case is 3 and 2, respectively. This matching analysis must be repeated for all possible templates of length *m* and *m+1* and in order to calculate A and B, the number of repetitions for each case are summed up. Finally, the sample entropy (*SampEn*) it is given by the conditional probability that two sequences that match each other for the first *m* data points also match for the next point (Richman & Moorman 2000) and is computed through Eq. 4.

$$\boldsymbol{SampEn(m,r) = -\ln\left(\frac{A^m(r)}{B^m(r)}\right)} \qquad \textbf{Eq. 4}$$

Complexity Index Computation

The final step of this algorithm was to compute the complexity index (CI), given by the sum of the sample entropy over all scales, an approach similar to that presented in (Yang, Huang, et al. 2013) and (Ferreira et al. 2013). Hereupon, a quantitative comparison between two different time series could be made in terms of its complexity behavior.

Optimal parameters choice

In the modified MSE algorithm there are two parameters that must be chosen by the user, the pattern length *m*, and the similarity factor or tolerance *r*. In order to determine which pair of parameters (*m*,*r*) were the most suitable for shorter time series (with length around 100-250 time points), a set of surrogate signals were created and compared in terms of their CI. Those surrogate signals consisted of white and 1/f noises, signals known to behave differently in terms of its regularity (see Fig. 15). The comparison made between these two signals aimed to find the parameters values that give the highest difference, which is given by the anisotropy index (AI), Eq. 5.

$$AI = \frac{\left| CI_{white\ noise} - CI_{\frac{1}{f}noise} \right|}{CI_{white\ noise} + CI_{\frac{1}{f}noise}} \times 100 \qquad \textbf{Eq. 5}$$

Hereupon, the choice process consisted of the following steps. First, 20 000 white Gaussian and 1/f noises time series (10 000 of each) were created using an intrinsic function of Matlab® and a function created by (Little et al. 2007), respectively. Second, the sample entropy profile over scales 1 to 20 was computed for each time series, and the mean and standard deviation of the sample entropy for each scale and each noise type was calculated. Third, the CI corresponding to white and 1/f noises were computed in order to obtain the AI. This process was repeated for *m* values of 2 and 3 and *r* values of 0.1 to 0.5 times the standard deviation of the coarse-grained time series being analyzed for entropy computation, in increments of 0.05. Forth, a score is attributed to each pair of parameters (*m*,*r*) according to the

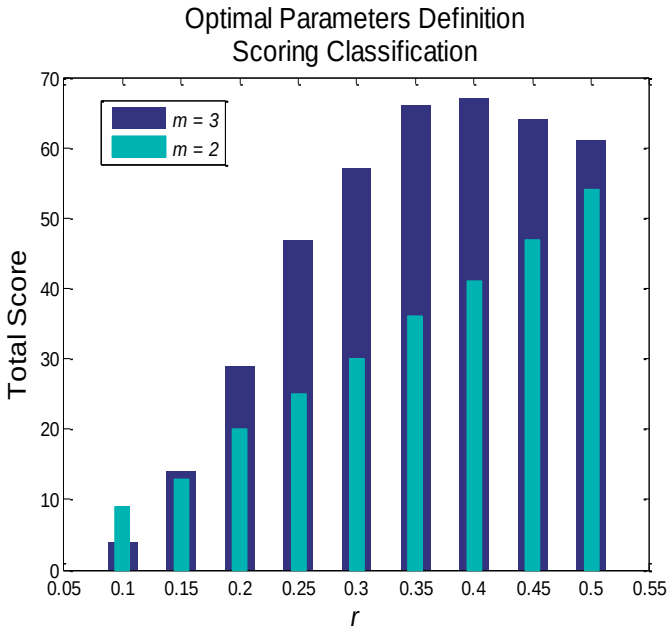

Fig. 18- Scoring classification for each possible pair of parameters (pattern length - *m*, tolerance - *r*) with a tested m = 2 (light blue) and 3 (dark blue) and r = 0.1 to 0.5 in steps of 0.05. Each bar represents the total score attributed to that case. The results showed that the optimal values for *m* and *r* are 3 and 0.4 times the standard deviation, respectively, with a total score of 67.

following criteria: (i) the highest score value is defined has the total number of cases, i.e., 2 *m* values times 9 *r* values that equals 18 total cases; (ii) the one corresponding to the highest AI is assigned with the highest score; (iii) the next case with the highest AI is assigned with the second highest score (e.g. 17), and so on, until no more cases remain. These four steps are repeated for original time series lengths from 100 to 250 time points in increments of 50 time points, and the score of each case (*m*,*r*) is accumulated. Finally, the best case is selected as the one with the overall highest score. The results (see Fig. 18) showed that the optimal values for *m* and *r* are 3 and 0.4 time the standard deviation, respectively, with a total score of 67. These values were used in the remaining MSE analysis.

3.2.2. Illustrative examples

The following examples were reproduced for illustrative purposes.

Comparison between sample entropy profiles of white and 1/f noise obtained using original and modified approaches. For this example, 200 white Gaussian and 1/f noises time series (100 of each) with 1 000 time points were created, in a similar way as described above (see **3.2.1 Modified MSE**: **Algorithm implementation**). Second, the sample entropy profile over scales 1 to 20 was computed for each time series, and the mean of the sample entropy (computed with *m*=3 and *r*=0.4) for each scale and each noise type was calculated. This process was repeated using the original and the modified approaches and the sample entropy for each case was plotted on the same figure. The main goal of this example was to compare the sample entropy profiles originated from these two approaches.

Comparison between sample entropy profiles of short white and 1/f noise time series obtained using original and modified approaches. For this example, 200 white Gaussian and 1/f noises time series (100 of each) with 100, 150, 200, and 250 time points were created, in a similar way as described above (see **3.2.1 Modified MSE: Algorithm implementation**). Second, the sample entropy profile (computed with *m*=3 and *r*=0.4) over scales 1 to 20 was computed for each time series, and the mean of the sample entropy for each scale and each noise type was calculated. Third, the CI corresponding to white and 1/f noises were computed. This process was repeated using the original and the modified approaches. The main goal of this example was to compare the sample entropy behavior over scales and its influence on CI computation when used either of these two approaches for short time series.

Comparison between sample entropy profiles and respective CI of white, 1/f and 1/f^2 noise, and sinusoidal time series obtained using modified approach. For this example, 300 white Gaussian, 1/f and 1/f^2 (another type of noise also known as Brownian or red noise that corresponds to the integration of the white noise, see Fig. 19) noises time series (100 of each) with 250 time points were created, in a similar way as described above (see **3.2.1 Modified MSE: Algorithm implementation**). In addition to these signals two sinusoidal time series, created from a Matlab® intrinsic function with frequencies of 0.01 Hz and 0.1 Hz, a sample frequency of 0.5 Hz and a length of 250 time points (see Fig. 19), was also created in order to represent a periodic signal. The choice of this length is justified by the maximum length of short time series simulated in the above example.

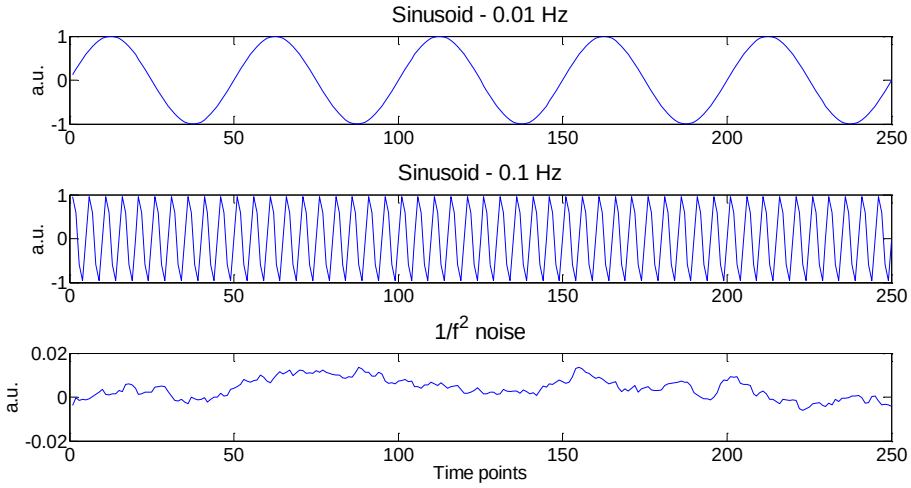

Fig. 19- Top: Sinusoidal time series with a frequency and sample frequency of 0.01 Hz and 0.5 Hz, respectively, and a length of 250 time points. **Bottom:** 1/f2 noise time series with a length of 250 time points.

The sample entropy profile (computed with *m*=3 and *r*=0.4) over scales 1 to 20 was computed for each time series, and the mean of the sample entropy for each scale and each noise type was calculated. Then, the CI corresponding to each signal type was computed. The main goal of this example was to compare the sample entropy behavior over scales and corresponding CI values when using a noise-like or periodic signal.

3.3. Results

Comparison between sample entropy profiles of white and 1/f noises obtained using original and modified approaches.

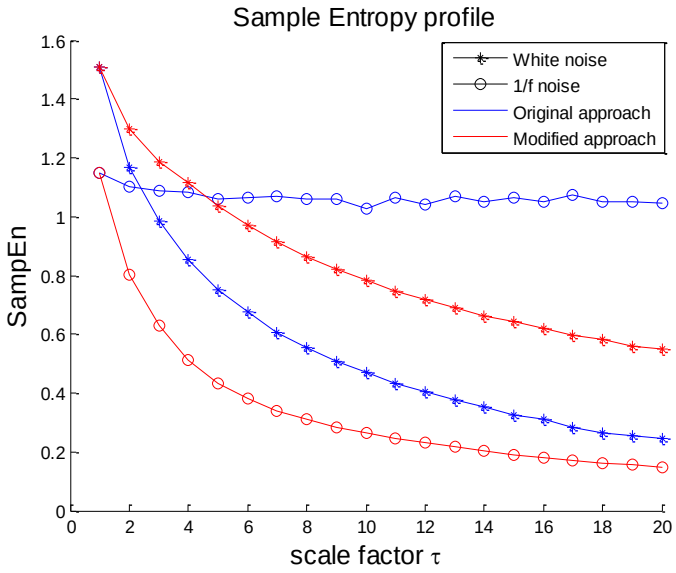

Fig. 20- Sample entropy profile (computed with m=3 and r=0.4) over scale for original time series of white (asterisk) and 1/f (circle) noises of length 1000 time points using the original (blue) and the modified (red) MSE algorithm.

Fig. 20 shows the sample entropy profile for white and 1/f noises using the original approach (in blue) and the modified approach (in red). The results demonstrate that sample entropy profile for the original method is different for the two types of noise: a 1/f noise time series have an approximately flat shape over scales, while a white noise time series decreases in a monotonic way. Also, for scales 1 and 2 the values of entropy for the white noise time series are greater than those for 1/f noise. However, as scale increases, those values become smaller than those for the 1/f noise.

On the other hand, when using the modified version of the MSE algorithm both sample entropy profiles monotonically decrease and the entropy values for white noise time series are greater than those for 1/f time series for all scales.

Lastly, for scale 1 the entropy value for both noises types are the same irrespectively of the MSE approach used.

Comparison between sample entropy profiles of short white and 1/f noise time series obtained using original and modified approaches.

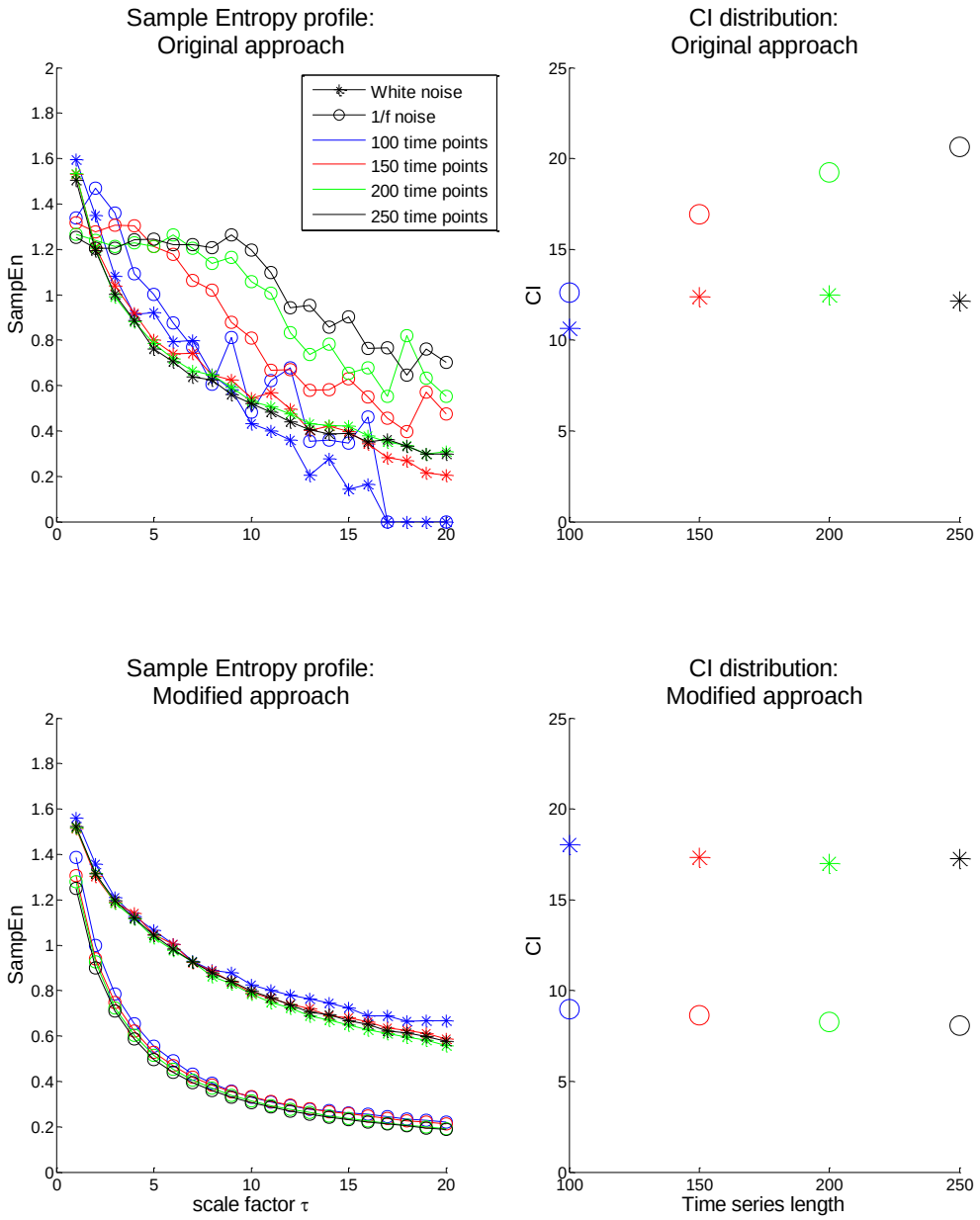

Fig. 21- Left: Sample entropy profile (computed with *m*=3 and *r*=0.4) over scale for original time series of white (asterisk) and 1/f (circle) noises with lengths in the range of 100 to 250 time points, in increments of 50, using the original (**Top**) and the modified (**Bottom**) MSE algorithm. **Right:** CI distribution in function of time series length correspondent to the sample entropy analysis presented at **left**.

Fig. 21 shows, on the left side, the sample entropy profile for white and 1/f noises using the original approach, on top, and the modified approach, on bottom, for time series of length 100, 150, 200, and 250 time points, in blue, red, green, and black, respectively. The results demonstrate that sample entropy profile for the original method have an instable behavior when compared to that originated from the modified approach as the length of the noise time series becomes shorter. Particularly, for time series of 100 data points' length the original MSE method compute sample entropy values with similar amplitude for white and 1/f noise time series over scales 3 to 20. This phenomena is, also, observable on the right side of Fig. 21 where the difference between the CI values, one for each type of noise time series, is consecutively greater as the length of the times series increases.

On the other hand, the sample entropy profiles and the corresponding CI values remain stable over scales independently of data length when it's used the modified version of the MSE algorithm.

Comparison between sample entropy profiles and respective CI of white, 1/f and 1/f² noise, and sinusoidal time series obtained using modified approach.

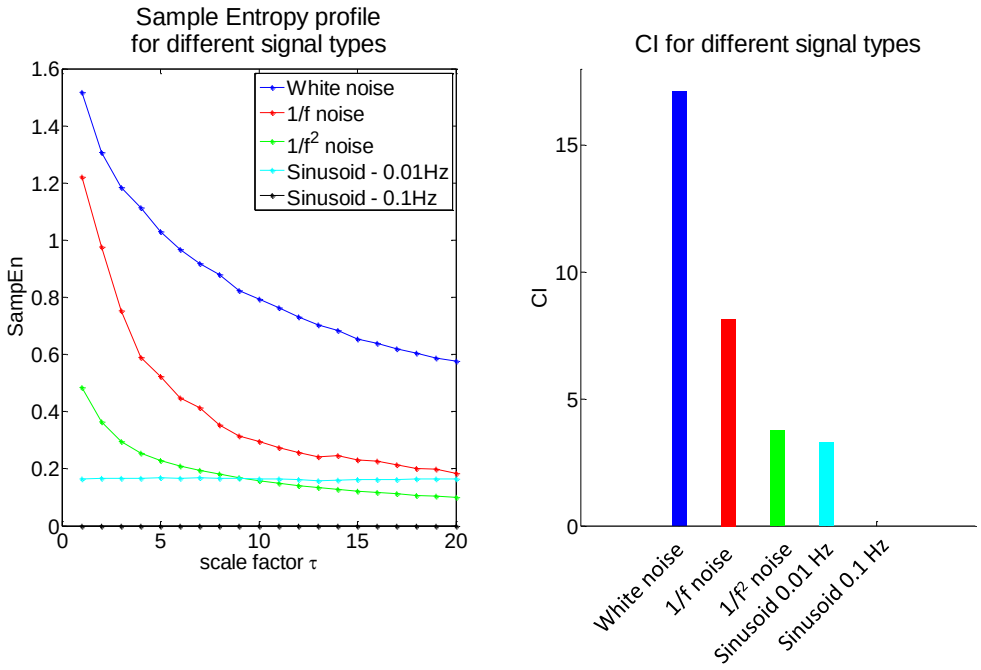

Fig. 22- Left: Sample entropy profile (computed with *m*=3 and *r*=0.4) over scale for time series of white (in blue), 1/f (in red) and 1/f² (in green) noises, and sinusoidal signals of 0.01 Hz (in cyan) and 0.1 Hz (in black) with a length of 250 time points using the modified MSE algorithm. **Right:** Corresponding CI values for each signal type presented at left. $CI_{White\ noise}$ = 17.2; $CI_{1/f\ noise}$ = 8.1; $CI_{1/f^2\ noise}$ = 3.8; $CI_{sinusoid\ 0.01\ Hz}$ = 3.2; $CI_{sinusoid\ 0.1\ Hz}$ = 0

Fig. 22 shows the sample entropy profile for white, 1/f and $1/f^2$ noises, and sinusoidal signal using the modified approach. The results demonstrate that sample entropy profile, computed using the modified approach, for the three types of noise has a similar shape, monotonically decreasing, but with lower overall sample entropy values from white to 1/f and $1/f^2$ noises, respectively. The sinusoidal signal of 0.01 Hz have an almost flat sample entropy profile with lower values in the range 0.155 to 0.166. Relatively to the 0.1 Hz sinusoidal signal the sample entropy is zero for all scales. The corresponding CI values are 17.2, 8.1, 3.8, 3.2, and 0 for white, 1/f, and 1/f2 noises and sinusoidal signals of 0.01 Hz and 0.1 Hz, respectively.

3.4. Discussion

This chapter describes a complexity analysis method based on the sample entropy property of the signal being analyzed over several scales, allowing the assessment and classification of the signal structure. The main advantage of this algorithm is its ability of distinguish two signals with different frequency dependency behaviors, a feature with high relevance when dealing with physiological signals.

The results shown in Fig. 20 for the original approach are consistent with those presented in (Costa et al. 2002; Costa et al. 2005). Since the white noise does not have complex structures, as the scale factor increase the coarse-grained time series tends to a fixed value, decreasing the sample entropy. On the other hand, 1/f noise is characterized by having equal energy in all octaves of frequency (Ward & Greenwood 2007) which mean that new information is given in each scale and. Therefore, when analyzing the sample entropy profile over scale of 1/f noise it is nearly flat with a constant value of entropy over scale.

For modified version of the MSE method the results in Fig. 20 show a different behavior of the sample entropy over scale for the two types of noise. This can be justified by a combination of the following factors. Back to the original definition of the sample entropy, this algorithm does not count for self matches, reducing possible biasing. From this point of view, lower values of sample entropy indicates more self-similarity in a time series (Richman & Moorman 2000). However, in this version of the MSE method, each coarse-grained time series is created using a moving average, implying an overlapping of information used in each average. Therefore, when the sample entropy is computed

for that coarse-grained data counting for self matches is implicit and a bias toward to low values of entropy may occur. Hereupon, it is, in fact, expected that the sample entropy profile monotonically decrease with scale.

Lastly, as expected, in Fig. 20, for scale 1 the entropy value for both noises time series are the same since the coarse-grained time series of scale factor 1 results in the original time series. For that case, the original and the modified MSE method are equivalent.

Fig. 21 shows results that demonstrate the advantage of the modified procedure of coarse-graining by comparing the sample entropy profile of noised time series with different lengths computed using both MSE methods. First of all, it is evident that when using the original approach the profile is extremely unstable for higher scales when the original time series are short. This statement is also confirmed by analyzing the CI distribution over the length: as the length decreases, the CI value from the two types of noise become closer, i.e., their difference becomes smaller.

On the other hand, the results show that the modified version of the coarse-graining procedure gives a sample entropy measure relatively independent of the original time series length. This fact demonstrates the utility and advantage of using this new approach when applying this complexity analysis to BOLD time series, since it is desirable to guarantee the most stability and reliability in all algorithm steps as possible.

Finally, the results shown in Fig. 22 demonstrate that, when using the modified approach of the MSE algorithm, the CI is higher for white noise-type time series than for colored noise-type signals. Periodic signals have the lowest CI value, as expected.

CHAPTER 4. DETRENDED FLUCTUATION ANALYSIS

4.1. Introduction

The fractal properties of a biological signal can be assessed using detrended fluctuation analysis (DFA) as it provides a measurement of statistical self-affinity (expressed by the scaling exponent, α) and can be applied to non-stationary signals. This method was first introduced by Peng and colleagues in (Peng et al. 1994) to study LRTC on DNA sequences. Since then this technique has been widely used in typical nonstationary biological signals (Peng et al. 1995; Parish et al. 2004; Monto et al. 2007; Ferreira et al. 2012a).

The DFA algorithm is illustrated in Fig. 23 and can be summarized in the following steps. First, it divides the entire time series of a given length into a selected number of windows, depending on the scale factor (Fig. 23 B). Second, within each window, the signal is integrated (Fig. 23 C) and linearly detrended (Fig. 23 D). Third, from the resulting time series, the root-mean-square (RMS) variation (Fig. 23 E) in each window is calculated, followed by determination of the characteristic size of fluctuation *F* in the given timescale, which is given by the mean of RMS variation (some authors perform the median of RMS variation to exclude the possible effects of large-amplitude artifacts that may bias the mean considerably (Monto et al. 2007)) of all windows of that scale. Fourth, a double logarithmic plot of these fluctuations against scales is done in order to evaluate whether this relationship is linear, indicating the presence of power-law (fractal) scaling ($F \sim (scale)^{\alpha}$). Lastly, the slope of this relationship, which corresponds to the scaling exponent, α, is determined using least squares fit (see Fig. 23 F) (Peng et al. 1995).

The quantitative measure of LRTC existent in the time series is provided by the scaling exponent. A value of α=0.5 corresponds to a signal that is completely uncorrelated, like white noise. On the other hand, when α=1 we're dealing with 1/f type signal meaning that the LRTC becomes independent of time with infinite range. If the analyzed signal have LRTC and power-law scaling, then it is expected that the scaling exponent lies within $0<\alpha<0.5$ or $0.5<\alpha<1$. The former represents an inverse relationship and indicates short-range correlations, such that large and small energy fluctuations are likely to be followed by small and large energy fluctuations, respectively, in other words, it represents anti-correlations. The latter means that the data are correlated in a direct way and indicates long-range correlations, such that large and small energy fluctuations are likely to be

followed by large and small energy fluctuations, respectively. As the scaling exponent increases from α=0.5 toward α=1, the temporal correlations in the time series are more persistent, i.e., decay more slowly with time. In contrast, when α>1 the correlations no longer exhibit power-law scaling and decay more rapidly. These cases are classified as fractional Brownian motion and, in particular, α=1.5 corresponds to Brownian or red noise (Peng et al. 1995; Parish et al. 2004; Monto et al. 2007; Eke et al. 2002).

Concerning the application of DFA specifically to epilepsy, Parish and colleagues studied the LRTC in EEG signals of healthy and pathologic human hippocampus by hypothesizing that the energy fluctuations in human hippocampus show LRTC with power-law scaling, and that these correlations differ between epileptogenic and non-epileptogenic hippocampi (Parish et al. 2004). Their results showed that the epileptogenic hippocampus have more persistent LRTC than the non-epileptogenic one and this may be due to the fact that the pathologic condition, epilepsy, increases the synchrony in the neuronal network.

Monto and colleagues performed another study on human brain DFA analysis basing their assumptions on the fact that in epileptic brain areas, the presence of intermittent abnormalities, interictal events and seizures, suggest a defect in stability of ongoing neuronal activity (Monto et al. 2007). Therefore, they hypothesized that epileptogenic cortical areas can be identified by quantifying the LRTC of the interictal iEEG activity. Thus an enhanced scaling exponent for epileptic regions was expected similarly to Parish work. Their results showed that the LRTC are abnormally strong near the seizure onset area suggesting, they argued, an association between the epileptic focus and the significant changes in network behavior. The justification of the authors for that observation relies on the following aspects: it could be due to a compensatory mechanism around the epileptogenic focus or it could be a persistent abnormality in this network due to exposure of neuronal networks to epileptic activity. Indeed, clustering of periods of oscillatory activity may result in strong LRTC, leading to a more probable period of high level activity when another such period first arises. This reflects the capacity of a network to be stable. In epilepsy, this phenomena of imminent instability could be a sign related to the susceptibility to seizure initiation. The studies presented above are focused on EEG signals. To the best of my knowledge there are no studies that applied DFA to epileptic BOLD signals.

4.2. Materials and Methods

The DFA algorithm implemented in this project is based on the approach presented in (Peng et al. 1995).

4.2.1. Algorithm implementation

Time series division into windows

As in MSE analysis, the DFA algorithm bases its analysis on one-dimensional time series, y, which were, as a first step, divided into windows, y_w, of length N_W and which can be overlapped (see Fig. 23 B).

Computations within in each window

After the time series division, the second step was to perform three operations within each window. The first and second ones correspond to the integration and to the linear detrending of the time series y_w, which result was here denoted by dy_w (see Fig. 23 C and D). This detrending process was accomplished by performing least squares fit and subtracting it from y_w. The last operation was to compute the RMS variation (see Fig. 23 E) according to Eq. 6.

$$\boldsymbol{RMS\ variation} = \sqrt{\frac{1}{N_w}\sum_i \left(\boldsymbol{dy_{w_i}}\right)^2} \qquad \textbf{Eq. 6}$$

Fluctuations profile over window length

Once the RMS variation of each dy_w was computed, the forth step was to calculate the characteristic size of fluctuation F for that specific window length N_W according to Eq. 7.

$$\boldsymbol{F} = \sqrt{\frac{1}{\#\boldsymbol{windows}}\sum_i (\boldsymbol{RMS\ variation_i})^2} \qquad \textbf{Eq. 7}$$

These four steps were repeated for each N_W in order to construct a double logarithmic plot of F against N_W and determine the scaling exponent (α) as the slope of the least squares fit between the $\log(F)$ and $\log(N_W)$ (see Fig. 23 F).

Optimal parameters choice

Similarly to the modified MSE method, in DFA algorithm there are two parameters that needed to be defined. The first one was with respect to the window length and the second one to the overlapping between the windows. Concerning the former, the number of N_W is dependent on the following factors: its minimum, which here is defined as 4 data points in order to guarantee a good performance of the linear detrending step; its maximum N_W; and the fact that both minimum and

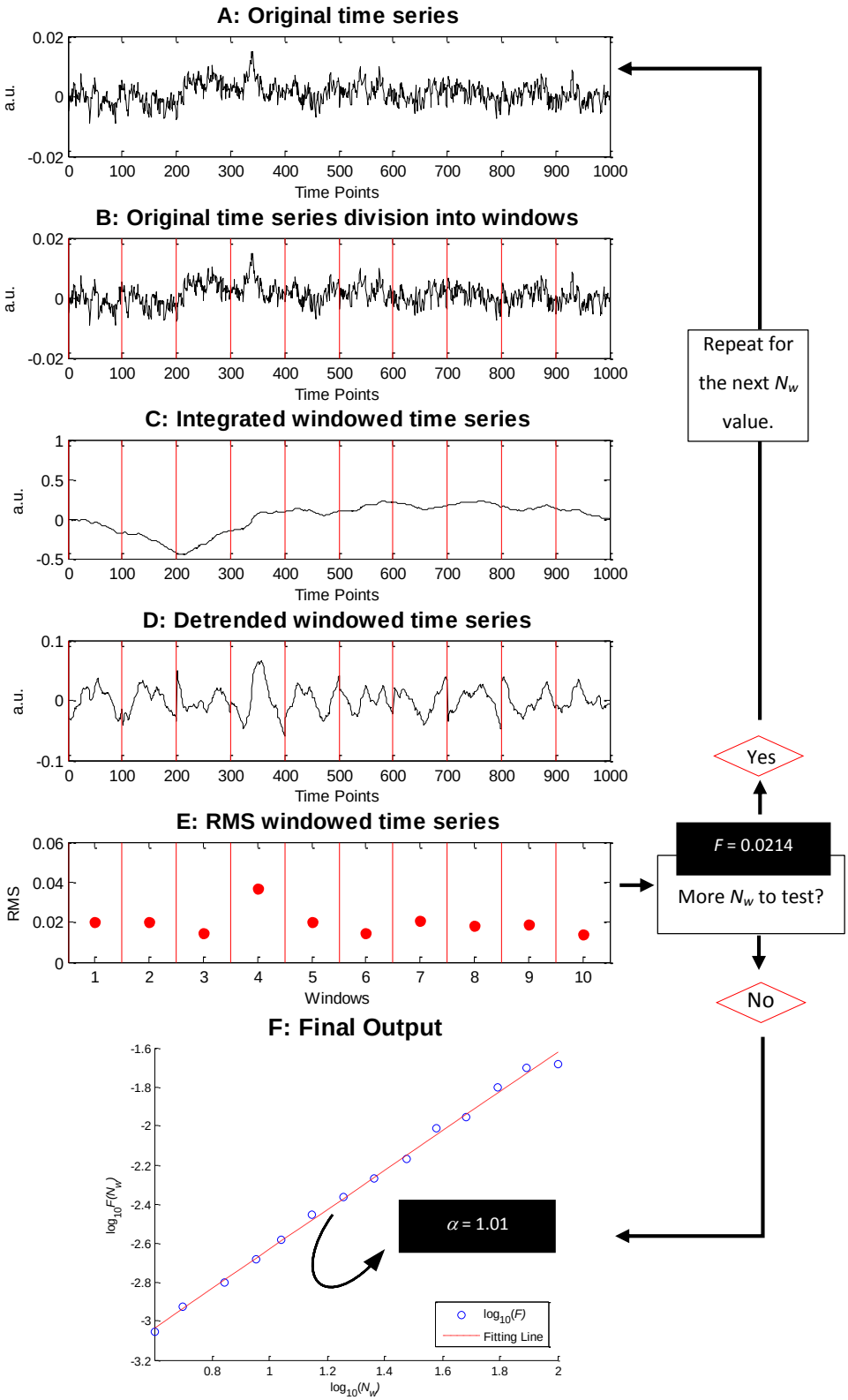

Fig. 23- Illustration of DFA algorithm steps. For this example a 1/f noise time series was created with a length of 1000 time points. The steps **A** to **E** represents the procedure for a window length, N_w, of 100 data points. **F** represents the final output when the previous steps were repeated for all N_w values. α: scaling exponent; F: RMS fluctuation.

maximum N_w's must be logarithmically separated in order to guarantee an equal weight to all time-scales when performing the linear fit on the double logarithmic scale.

A maximum N_W greater than 10 % of the total length of the original time series can decrease the accuracy of the estimation of fluctuations since the number of corresponding windows are low. This is an important limitation concerning the analysis of BOLD signals which have typically a length of 100-250 time points. Nonetheless, this imitation can be overcome with the introduction of an overlap between the windows, increasing the number of windows into which the original time series is divided.

Therefore, in order to find the best combination of the maximum percentage, p_{max}, of the original time series length and the overlap percentage between the windows, a similar scoring strategy as that for modified MSE (see **3.2. Materials and Methods - Optimal parameters choice**) was followed using the same surrogate signals (white and 1/f noises). The test was run for p_{max} values from 10 to 50 % in increments of 10 % and for overlap percentages values from 0 to 50 % in increments of 10 %.

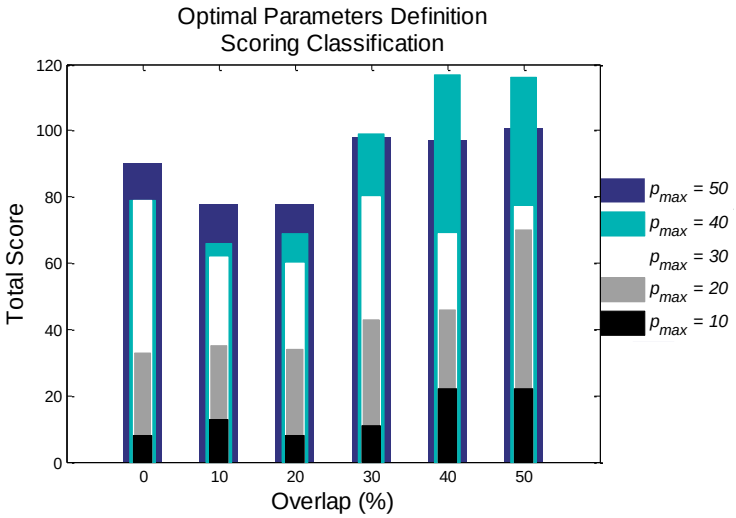

Fig. 24- Scoring classification for each possible pair of parameters (maximum percentage - p_{max}, overlap) with a tested range 50 % (dark blue), 40 % (light blue), 30 % (white), 20 % (gray), and 10 % (black) for p_{max} and 0 to 50 % in steps of 10 % for the overlap. Each bar represents the total score attributed to that case. The results showed that the optimal values for p_{max} and overlap are both 40 % with a total score of 117.

The AI in this case is computed using the mean of α (scaling exponent) across each noise time series where α replaces the CI on the discussion of the modified MSE approach. As for the modified MSE, the best case is selected as the one with the highest overall score and used in the remaining DFA analysis.

The results (see Fig. 24) showed that the optimal values for p_{max} and overlap are both 40 % with a total score of 117. These values are used in the remaining DFA analysis.

4.2.2. Illustrative examples

The following examples were reproduced for illustrative purposes.

Comparison between α values of white and 1/f noises. For this example, the same noise time series as those of the first example of MSE illustration, with 1000 time points each, were used (see **3.2.2 Illustrative examples**). The DFA algorithm was applied to each dataset and the mean fluctuations profiles across each type of noise was computed (using p_{max} and overlap equal to 40 %). The main goal of this example was to compare the fluctuations profile of the two types of noise and to observe the typical α values for each noise type.

Comparison between α values of short white and 1/f noises time series. For this example, the same noise time series as those of the second example of MSE illustration, with 100, 150, 200, and 250 time points, were used (see **3.2.2 Illustrative examples**). The DFA algorithm was applied to each dataset and the mean α across each type of noise was computed (using p_{max} and overlap equal to 40 %). Then, the AI corresponding to white and 1/f noises were computed. The main goal of this example was to assess the influence of short time series length on the AI between the two types of noise.

Comparison between α values of white, 1/f and $1/f^2$ noise, and sinusoidal time series. For this example, the same time series as those for the third example of MSE algorithm, with 250 time points each, were used (see **3.2.2 Illustrative examples**). The DFA algorithm was, then, applied to each dataset and the mean fluctuations profile across each type of signal (using p_{max} and overlap equal to 40 %) and the corresponding α values were computed. The main goal of this example is to compare the fluctuations profile and corresponding α values when using a noise-like or periodic signal.

4.3. Results

Comparison between α values of white and 1/f noises.

Fig. 25 shows the fluctuations profiles over window length in a double logarithmic plot for both white and 1/f noise time series. Also in the figure are shown the α values, which correspond to the slope of the fitting line, for the white (red, α = 0.51) and 1/f (blue, α = 0.96) noises and the corresponding AI with the value of 30.5 %.

Comparison between α values of short white and 1/f noises time series.

Fig. 26 shows the α values for short time series lengths (100 (blue), 150 (red), 200 (green), and 250 (black) time points) for both white (asterisk) and 1/f (circle) noises. Also in the figure are shown the corresponding AI values. The results show a nearly constant value for the scaling exponent of the two types of noise ($\alpha_{\text{white noise}}$ = 0.54 ± 0.01; $\alpha_{1/f\ \text{noise}}$ = 0.93 ± 0.01). Concerning the AI results, it is observed that AI values decrease with the decrease of the time series length.

Comparison between α values of white, 1/f and 1/f² noise, and sinusoidal time series.

Fig. 27 shows the fluctuations profiles over window length in a double logarithmic plot for white, 1/f and 1/f² noises, and sinusoidal signal. Also in the figure are shown the α, which correspond to the slope of the fitting line, for the white (in blue, α = 0.52), 1/f (in red, α = 0.94), and 1/f2 (in green, α = 1.3) noise, and for the sinusoidal signal of 0.01 Hz and 0.1 Hz (in cyan, α = 1.6, and in black, α = 0.093, respectively).

In Fig. 28 the influence of sample frequency and sinusoidal frequency on the α value is shown. It is demonstrated that the value for the DFA parameters decreases as the sample and sinusoidal frequencies also decrease.

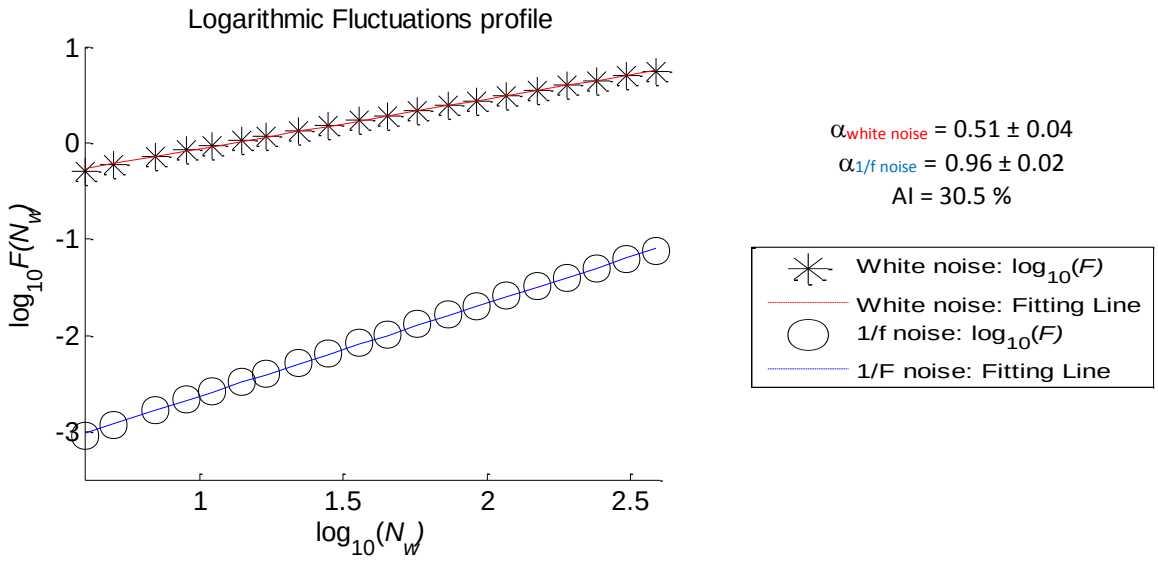

Fig. 25- Double logarithmic plot of fluctuations (computed with p_{max} and overlap equal to 40 %) over window length for white (asterisk) and 1/f (circle) noise time series of length 1000 time points using the DFA algorithm. The fitting line for each fluctuations profile is represented at red for white and at blue for 1/f noises.

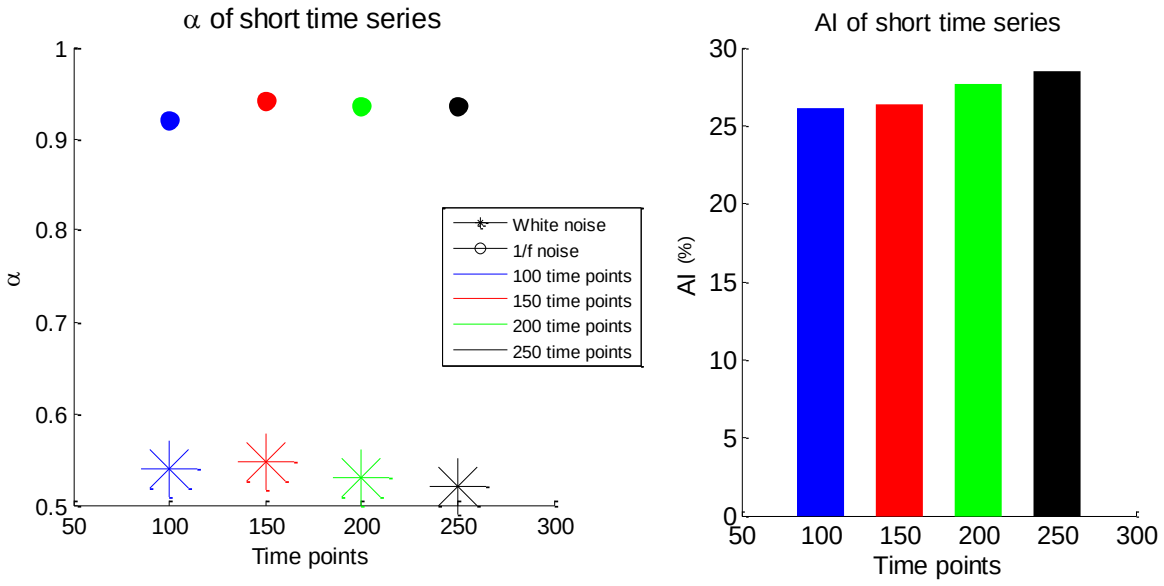

Fig. 26- Left: α value (computed with p_{max} and overlap equal to 40 %) for time series of white (asterisk) and 1/f (circle) noise with lengths of the time series in the range of 100 to 250 time points, in increments of 50, using the DFA algorithm. **Right:** AI distribution in function of time series length correspondent to the α values presented at the left.

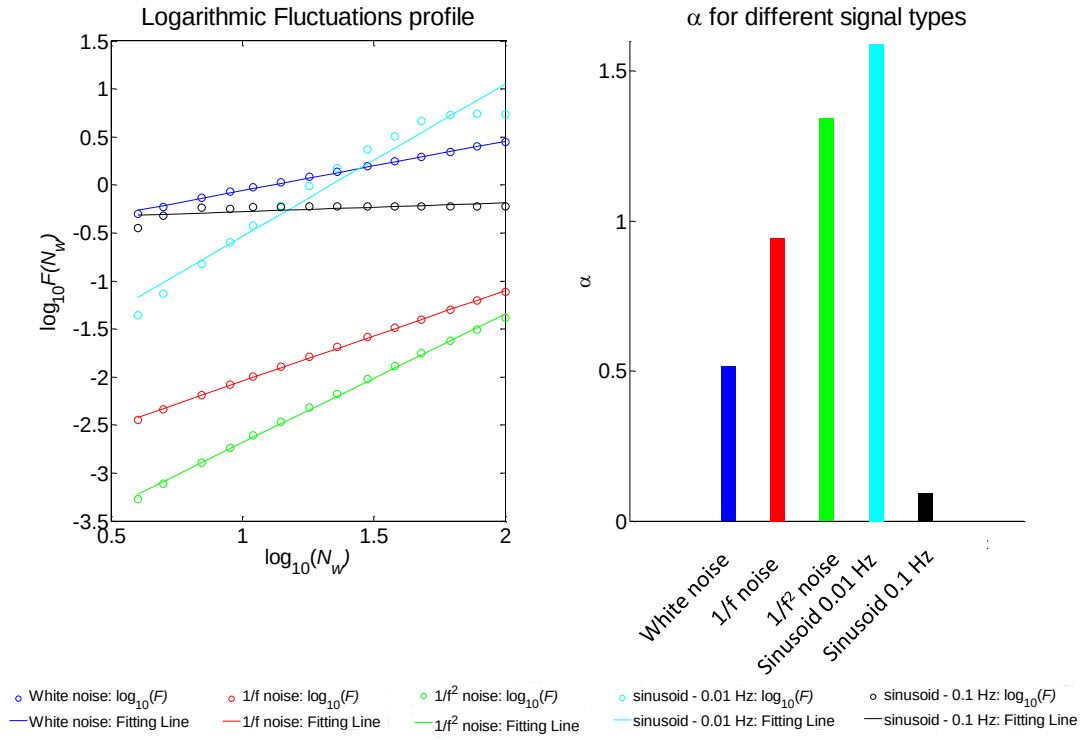

Fig. 27- Left: Double logarithmic plot of fluctuations (computed with p_{max} and overlap equal to 40 %) over window length for time series of white (in blue), 1/f (in red) and 1/f² (in green) noises, and sinusoidal signal of 0.01 Hz (in cyan) and 0.1 Hz (in black) with a length of 250 time points using DFA algorithm. **Right:** Corresponding α values for each signal type presented at left. $\alpha_{White\ noise} = 0.52$; $\alpha_{1/f\ noise} = 0.94$; $\alpha_{1/f^2\ noise} = 1.3$; $\alpha_{sinusoid\ 0.01\ Hz} = 1.6$; $\alpha_{sinusoid\ 0.1\ Hz} = 0.093$.

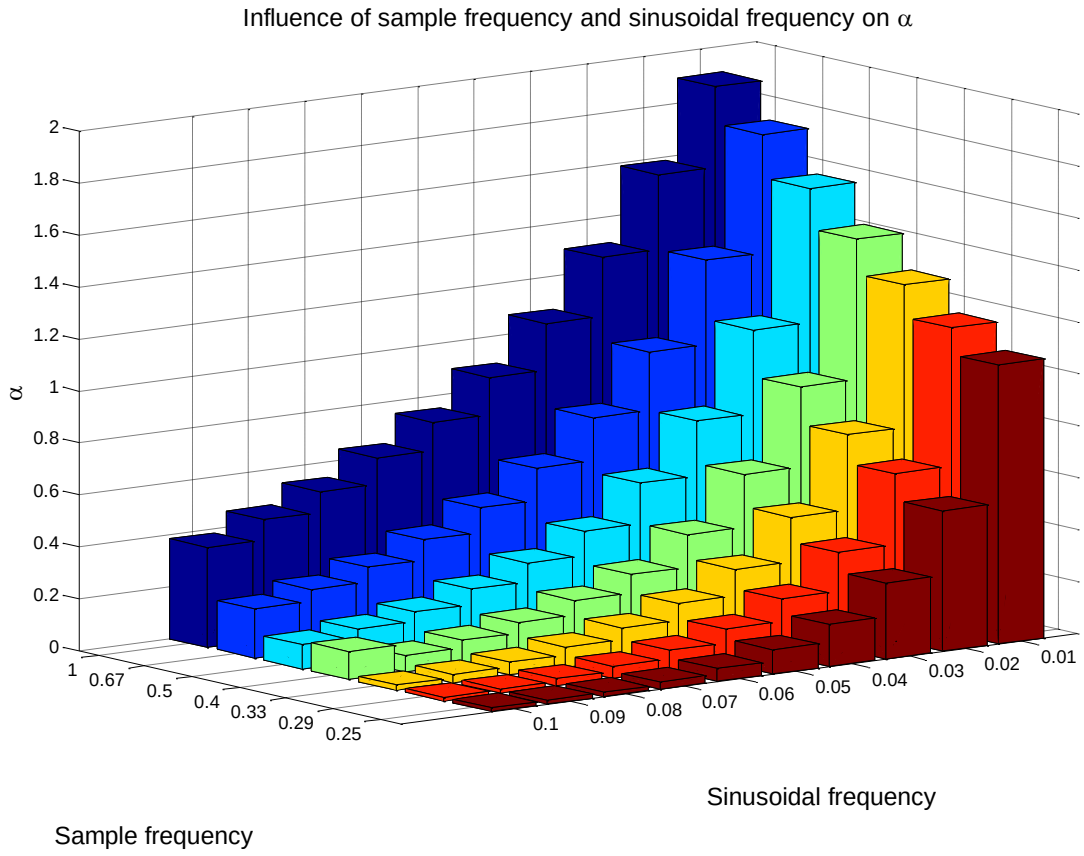

Fig. 28- Influence of sample frequency and sinusoidal frequency (in Hz) on α value.

4.4. Discussion

This chapter describes another complexity analysis method based on the fractal properties of the signal being analyzed, allowing the assessment and classification of the signal structure in terms of its self-similarity. The main advantage of this algorithm is based on its ability to analyze non-stationary time series, as those that translate physiologic information, and, as in the MSE method, its capacity to distinguish two signals with different fractal properties, a feature with high relevance when dealing with physiological signals.

Concerning what is shown in Fig. 25, the results are consistent with what it is expected for these two type of noise (Peng et al. 1995): a α close to 1 for time series with 1/f noise behavior and close to 0.5 for uncorrelated time series, like white noise. For both cases the fluctuations increase with the increase of the window length, a result consistence with previous studies (Peng et al. 1994; Peng et al. 1995; Monto et al. 2007; Parish et al. 2004).

The influence of short time series on the final output of the DFA algorithm was assessed by comparing the α of white and 1/f noise time series with a number of time points that are typical of BOLD time series. The results, shown on Fig. 26, demonstrate that the AI between the two types of noises tends to decrease with shorter time series, meaning that the distinction is greater for longer time series. Nonetheless, the difference between the AI for 1000 time points (AI=30.5 %) and 100 time points (AI=26.1 %) is smaller than 7.8 %.

The typical values for the α of white, 1/f, and $1/f^2$ noises, and periodic signal are shown in Fig. 27 and Fig. 28. Values of α are lower for white noise-type time series than for colored noise-type signals. Although a monotonic relation cannot be state for periodic signals, since the α value depends on the sampling frequency (equivalent to the repetition time on fMRI acquisitions) and of the signal itself. This is due to the fact that the RMS fluctuations of sinusoidal signals have a crossover at window lengths that depend on the signal period, dividing the fluctuations profile in two main lines: one representing a scaling behavior of $\alpha \approx 2$ and another flat region with $\alpha \approx 0$ (more details about this phenomena can be found in (Hu et al. 2001)). Fig. 27 shows the two extreme examples of this effect on α value. A sinusoid with frequency of 0.01 Hz and with a sampling frequency of 0.5 Hz has a crossover at logarithmic window length of 1.8. On the other hand a sinusoid with a frequency of 0.1 Hz and with the same sample frequency has a crossover at logarithmic window length 0.8. Therefore, it expected that a periodic signal has an α value influenced by its period or frequency.

Regarding the interpretation of the DFA algorithm output there are some pitfalls that need to be taken into account. In order to use the scaling exponent as a signal classifier it is required a linear relationship on the double logarithmic plot between the fluctuations and the windows length (Peng et al. 1994; Eke et al. 2012), once only in that case it can be said that there is a presence of self-similarity in the signal (remember that the a linear relationship means a power law scaling of the fractal properties of the signal, see **4.1 Introduction**). Finding a value for the scaling exponent is always possible, the acceptance of it depends on the uncertainty degree that is accepted in this type of analysis.

CHAPTER 5. EPILEPTIC PATIENTS STUDY

5.1. Introduction

5.1.1. Types of epilepsy

Epilepsy is actually a generalist word to designate a set of neurological diseases whose root denomination is epilepsy (Fisher et al. 2005). There is a set of epilepsies characterized by different origins, behaviors and developments that influences the method used in its analysis. In this study two kinds of epilepsy disorders will be study as an example of the application of the developed analysis method: temporal lobe epilepsy (TLE) and focal cortical dysplasia epilepsy (FCDE).

The TLE is a type of epilepsy with origins in the temporal lobe structures and characterized by peculiar sensory symptoms like smelling an inexistent odor or a disturbance of memory. This disorder is by far the most studied type of epilepsy in the scientific community due to its large number of cases in both children and adults. The most common cause of this disorder is the mesial temporal sclerosis which affects usually structures located in the medial and lateral temporal cortex, in particular the hippocampus, parahippocampus gyrus and the amygdala (Holmes et al. 2013). In this kind of epilepsy the source of epileptogenic activity is usually a heterogeneous zone surrounded by an 'irritative zone'. This zone is characterized by its capacity to modulate the activity from the source and spread it like a interplay core between extended neuronal networks (Curtis et al. 2012; Monto et al. 2007).

The FCDE is characterized by a malformation in the brain cortex that is usually focal and may vary in size and location. This type of epilepsy have its origin in tissue intrinsically epileptogenic, namely the dysplasia. Almost half of intractable epilepsy cases are due to these cortex malformations and normally the only feasible treatable is the surgical resection. The main symptom associated with this disease is epilepsy (Kabat & Król 2012).

5.1.2. Epileptic activity and its influence on functional brain connectivity

For either of the cases discussed above the functional relations between the epileptogenic focus and the remaining regions of the brain are an important topic of discussion. It is not expected that a delimited brain region has an inherent electric activity if this does not have an outcome, i.e., spread or influence another brain regions activity. In other words, brain regions are functionally interconnected and in a dynamic way creating networks (Hutchison et al. 2013).

Thus, it is expected that an epileptogenic focus has repercussions on the electric activity behavior of all the brain regions that are related to the source either by creating new networks (epileptic networks) or influencing existing ones (Morgan et al. 2010; Morgan et al. 2012; Holmes et al. 2012; Bernhardt et al. 2013).

5.1.3. Revisiting methodological hypotheses

The two main hypotheses (see **Chapter 1: Introduction and Objectives**) of this methodological work are the following: the epileptogenic focus has a distinct behavior from the remaining brain parenchyma (Morgan et al. 2007; Victoria L Morgan et al. 2008; Morgan et al. 2010; Federico et al. 2005; Bagshaw et al. 2004; Salek-Haddadi et al. 2006; Kobayashi et al. 2005) and the complexity of that focus is lower than that of healthy parenchyma (Monto et al. 2007; Parish et al. 2004; Protzner et al. 2010). In the first one, the 2dTCA algorithm was used to find brain regions whose temporal behavior is distinct from others. In the second one, the BOLD signal of these potential foci were analyzed with MSE and DFA algorithms in order to study their complexity characteristics, namely its entropy and LRTC.

Therefore, in terms of the complexity parameters (CI for MSE and α for DFA), it is expected that an epileptogenic BOLD signal has a lower CI than a non-epileptogenic signal, more specifically a CI value near the typical values for sinusoidal signals than those of noise (see Fig. 22). Regarding the α its value may vary with the frequency of the stimulus (see **Chapter 4: 4.4 Discussion** and Fig. 27 and Fig. 28). Thus, in a plane of AI of CI against AI of α (with anisotropy computed between epileptogenic and non-epileptogenic signals) it is expected to find anisotropy values in the 3rd and 4th quadrants (see bottom right chart in Fig. 29).

Since studies supporting these hypotheses were based on data from patients with TLE, this method will be tested first on two patients with TLE. Then, a patient with FCDE will be tested in order to verify if the assumptions made for TLE patients stand also for FCDE patients.

5.2. Materials and Methods

5.2.1. Sample characterization

Patient	Gender/Age (years)	Type of epilepsy	Focus localization
1	M/60	Unilateral TLE	Left temporal lobe
2	M/19	Bilateral TLE	Bilateral with right temporal-parietal predominance
3	F/33	FCDE	Right precentral gyrus

Table 1- Epileptic patients sample characterization: gender, age, type of epilepsy, and localization of its epileptogenic focus. F: female; M: male; TLE: temporal lobe epilepsy; FCDE: focal cortical dysplasia epilepsy.

In this study 3 epileptic patients were studied, including 1 with unilateral TLE, 1 with bilateral TLE, and 1 with FCDE. A summary of patients characteristics is presented in Table 1, including gender, age, type of epilepsy, and localization of the epileptogenic focus.

For patients 1 and 2: MRI imaging of was performed using a Magneton Avanto 1.5T MRI scanner (Siemens, Erlanger, Germany) prior to surgery. Functional scanning was performed using T2* weighted single-shot spin echo sequence with echo planar images readout (SS-SE-EPI) (matrix = 64 x 64, voxel size =3.44 mm x 3.44 mm x 5.5 mm, 21 interleaved slices, TE = 50 ms, TR = 2 s, 150 volumes). These data was kindly made available by Hospital São José, Centro Hospitalar de Lisboa Central, E.P. E.

For patient 3: MRI imaging of was performed using a GE Genesis Signa 1.5T MSRI scanner (General Electrical, Waukesha, WI, U.S.A.) prior to surgery. Functional scanning was performed using T2* weighted single-shot spin echo sequence with echo planar images readout (SS-SE-EPI) (matrix = 64 x 64, voxel size = 3.75 x 3.75 mm x 5 mm, 26 ascending slices, TE = 50 ms, TR = 2.5 s, 140 volumes). These data was kindly made available by Hospital Júlio de Matos, Centro Hospitalar de Lisboa Central, E.P. E.

5.2.2. Pipeline Analysis

This section describes the steps of the analysis of the epileptic patients' dataset. In this study the three methods presented on the previous Chapters (2dTCA, MSE and DFA) are combined in order to produce an output able to define a brain region as a likely epileptogenic focus. A flowchart that summarizes the pipeline is presented on Fig. 29.

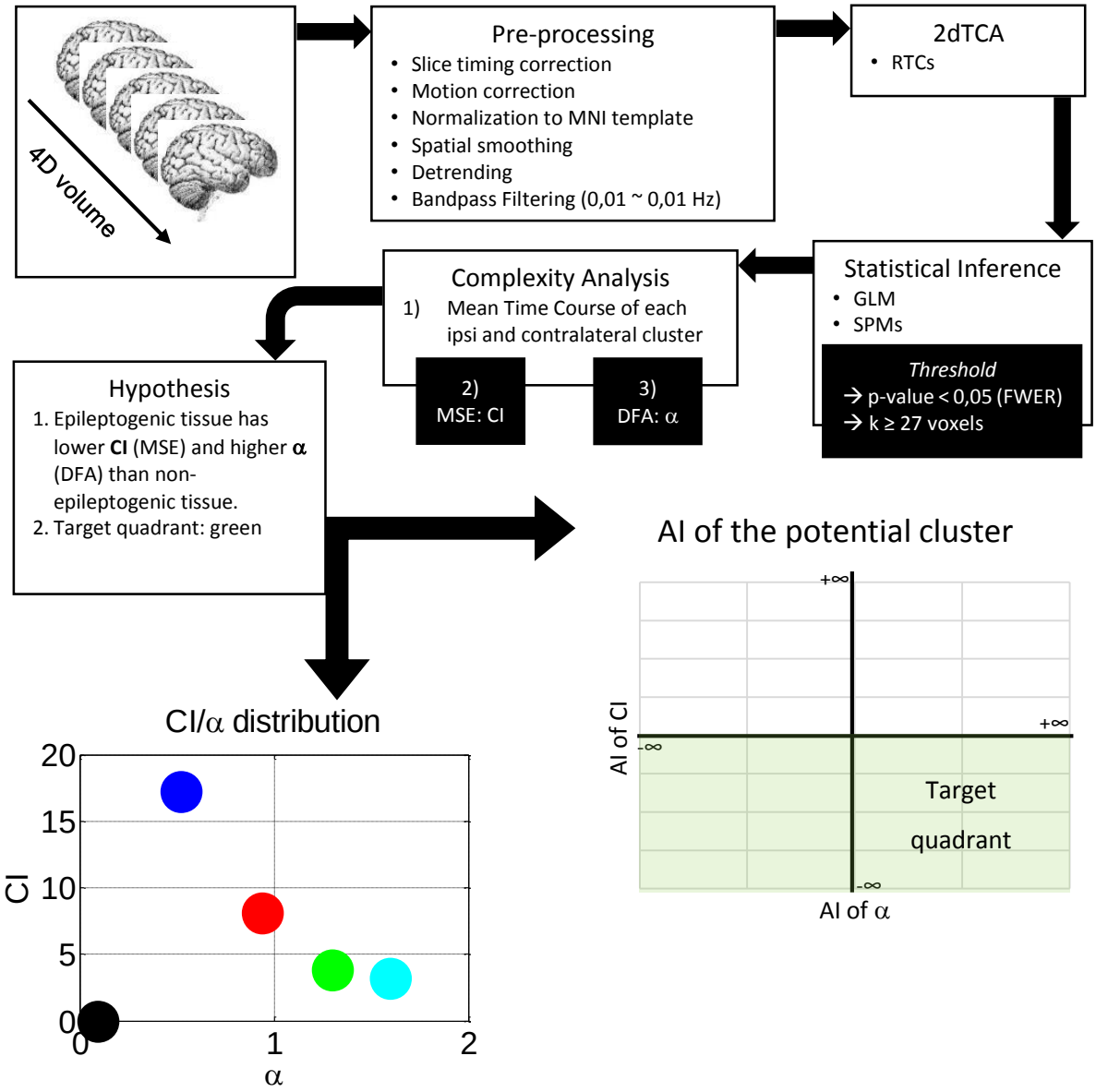

Fig. 29- Flowchart illustrating the pipeline analysis of real subject data, namely, epileptic patients' dataset. α: scaling exponent; AI: Anisotropy index; CI: Complex Index; DFA: Detrended Fluctuation Analysis; GLM: General Linear Model; FEWR: Family-Wise Error Rate; k: extended threshold; MSE: Multiscale Entropy; RTC: Reference Time Course; SPM: Statistical Parametric Map. Circles on CI/α distribution: blue: white noise; red: 1/f noise; green: $1/f^2$ noise; cyan: sinusoid of 0.01 Hz; black: sinusoid of 0.1 Hz.

Data pre-processing

The first important step on real data study was to perform a careful pre-processing of the fMRI volumes or scans. This was accomplish using DPARSF[4] toolbox (Chao-Gan & Yu-Feng 2010) and

[4] Data Processing Assistant for Resting-State fMRI (http://rfmri.org/DPARSF)

included slice timing correction for interleaved or ascending slice acquisition, realignment due to movement effects (from which 6 motion parameters were obtained), normalization to MNI[5] space (Tzourio-Mazoyer et al. 2002) using the echo planar imaging (EPI) template provided by DPARSF (and from which a picture showing the brain regions covered by this normalization was obtained), data spatial smoothing with a Gaussian 4 mm FWHM kernel, detrending, and filtering using a bandpass filter with lower and upper cutoff frequencies of 0.01 and 0.1 Hz, respectively. Additionally, a brain mask of gray matter (more specifically an AAL[6] mask (Tzourio-Mazoyer et al. 2002)) was used in order to mask out voxels that do not correspond to gray matter.

Localization of candidate epileptogenic foci

After the pre-processing, RTCs were obtained using the 2dTCA algorithm and, together with the six motion parameters and the global time course, were statistically analyzed (see **Chapter 2: 2.2.2 Algorithm implementation – t-maps *creation***). The obtained SPMs (one for each RTC) were individually analyzed and thresholded using a Family-Wise Error Rate (FWER) with a p-value<0.05.

Then, an extended threshold k of 27 voxels was applied in order to define clusters of voxels with activation (derived from each RTC). More details about SPM thresholding can be found on **Appendix A**.

The next step was to analyze each thresholded SPM and classify each cluster as a potential epileptogenic focus or a dubious one, which was accomplished in the following way: potential clusters were defined as those who cover a delimited brain region (typically with less than 200 voxels of extend, depending on the voxel real size). Dubious clusters were those which covered brain regions unlikely to belong to delimited epileptogenic tissue: being too large (with more than 200/300 voxels in size) and localized on questionable regions (like those whose scan volumes does not cover, which can be defined by visual inspection of the pictures for normalization checking).

Before the complexity analysis was performed, the SPMs with more than one potential cluster underwent a visual inspection in order to verify if those clusters belong to a known brain network (like the DMN and the Visual Network (VN)) or if they represent contralateral regions. If so, the SPM was classified as potential confound in the remaining analysis.

[5] Montreal Neurological Institute
[6] Automated Anatomical Labeling

The localization of all the brain regions covered by each cluster was accomplished using xjView toolbox[7].

Complexity analysis: cluster's mean time series classification

The next step was to extract the mean time series of each cluster and that of its contralateral cluster, which was defined as the sagittal mirror region of the ipsilateral cluster. This average was taken across all the voxels contained in each cluster. In cases where the ipsilateral cluster position covered also the medial or sagittal brain line, and therefore, part of the two brain hemispheres, the voxels that were superimposed by the two clusters (ipsi and contralateral) were excluded from the analysis. This avoided comparison between results that were from the same region.

In order to determine if each cluster was likely an epileptogenic focus or not, its mean time series was analyzed in terms of its complexity and compared to that of the contralateral cluster. Hereupon, the MSE and DFA algorithms were applied to each mean time series (from each ispi and contralateral cluster) and the CI and α, respectively, were extracted. Then, the AI was computed for each complexity output between the ipsi and contralateral cluster complexity result using Eq. 8, where cp means complexity parameter. This equation differs from Eq. 5 as it accounts not only for the magnitude of the difference, but also for the sign of the difference.

$$\mathbf{AI_{cp}} = \frac{\mathbf{cp_{ipsilateral\ cluster} - cp_{contralateral\ cluster}}}{\mathbf{cp_{ipsilateral\ cluster} + cp_{contralateral\ cluster}}} \times \mathbf{100} \qquad \textbf{Eq. 8}$$

This process was repeated for each cluster and the AI values for all cases were plotted on the same figure: the AI for CI on the Y-axis and the AI for α on the X-axis (see bottom right chart in Fig. 29). The goal of this plot was to discriminate which cluster had an AI in the quadrant of interest (the 3rd and 4th quadrants, see green shadow on bottom right chart of Fig. 29).

Additionally, the mean of CI and α of each cluster of a given RTC was computed for all analyzed RTC's SPM and the distributions of CI against α for all analyzed RTC's SPM were plotted (see bottom left chart on Fig. 29). The goal of this plot was to locate as a whole each SPM in the complexity plane.

Finally, the cluster was classified as a target if its AI values were on the 3rd or 4th quadrants, i.e., if AI_{CI} has negative values. Within these quadrants the cluster which have the smallest AI_{CI} was the first likely to belong to epileptogenic tissue. The second cluster with the smallest AI_{CI} is the second likely to belong to epileptogenic tissue and so on.

[7] http://www.alivelearn.net/xjview

Additional analysis

In addition to the complexity assessment, a correlation analysis was also performed to each cluster in two ways. The first one was to compute the Pearson's linear correlation matrix between each ispi and contralateral cluster's mean time series using an intrinsic Matlab® function. The goal of this step was to assess the main temporal relations between each cluster.

The second one was to perform a voxel-wise functional connectivity analysis between the cluster's mean time series and the time series of each other voxel of the brain. This functional connectivity was assessed simply by the same correlation coefficient used to the first additional analysis step and was performed using REST[8] toolbox (Song et al. 2011). This toolbox performs a variable transformation of the computed correlation coefficient to the normal distribution, a z-score, using a Fisher's z transform (more details about this transformation can be found in (Press et al. 1988)). This is accomplished using Eq. 9.

$$z = 0.5 \times \log \frac{1+r}{1-r} \qquad \textbf{Eq. 9}$$

In order to determine which voxels were statistically significant in this analysis a significance level of 5% (corresponding to two standard deviations of all voxels' z-score) was used to threshold the z-score brain map. The goal of this step is to assess the main temporal relations between each cluster and the remaining brain regions (or voxels).

Validation of found epileptogenic focus

The final step of the real data study on epileptic patients was the validation of the epileptogenic focus found through the described approach. In order to do that clinical information available for each patient is confronted to the obtained results and the focus is validated if both information match.

[8] Resting-State fMRI Data Analysis Toolkit (http://restfmri.net/forum/index.php)

5.3. Results

The results of the real data analysis for those patients described in **5.2.1 Sample characterization** are presented in this section.

5.3.1. Patient 1 – Unilateral Temporal Lobe Epilepsy (TLE): left TLE

Fig. 30 shows the histogram of the distribution of the number of voxels across the values of the transient spike selection limit. The results show that 4.1% of the voxels are above the 3% of signal change and 74.4% of the voxels are between the lower and upper boundaries (0.5 and 3% of signal change, respectively; see red dashed lines on Fig. 30).

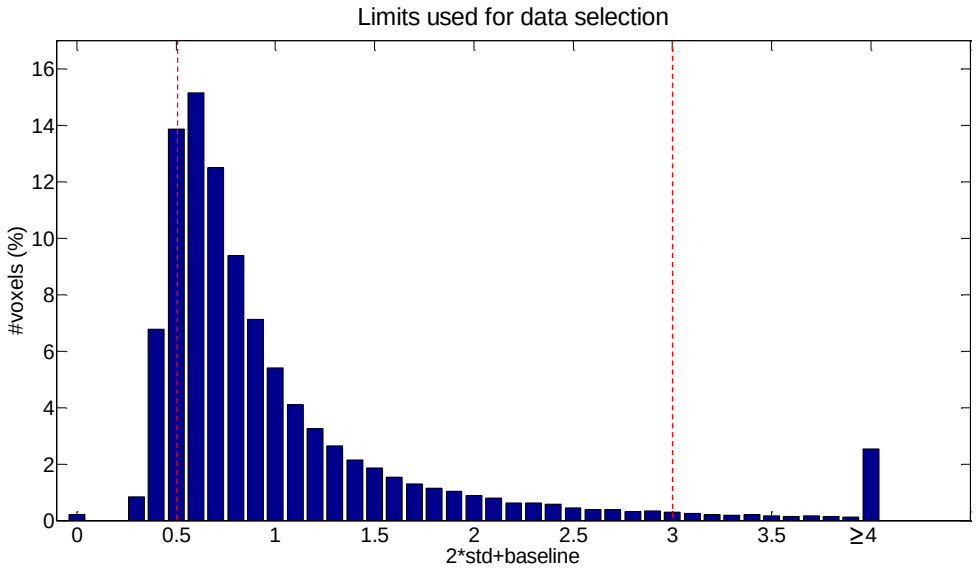

Fig. 30- Histogram showing the distribution of the number of voxels with a given value of the transient spike selection limit [2 standard deviations (std) above the baseline] for patient 1. Red dashed lines represents the lower and upper boundaries of allowed signal change (see **Chapter 2: 2.2.2 Algorithm implementation – Candidate voxels selection**).

The result of the bi-dimensional histogram mapping and its diagonal profile are shown on Fig. 31. Each column of this histogram represents a RTC, and a total of 140 RTCs were found on this patient.

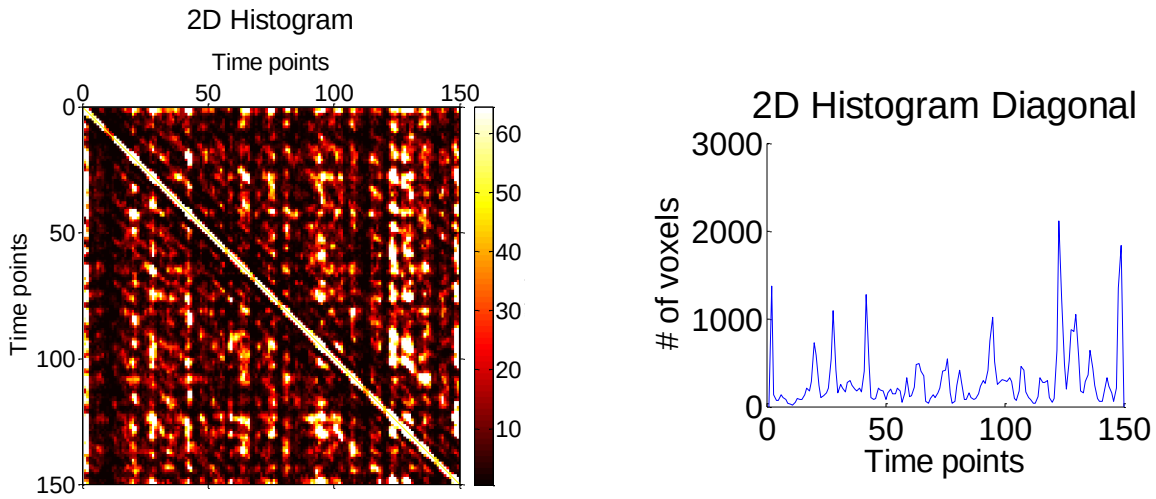

Fig. 31- Results for patient 1. **Left:** bi-dimensional histogram with the counting of transient spikes over the time. Each column represents a preliminary RTC. **Right** diagonal profile representing the number of voxels which maximum occurs in each time point.

After performing the RTCs number reduction and its normalization, 16 RTCs remained for statistical analysis. From those 16 RTCs only 4 (RTC_1, RTC_5, RTC_7, and RTC_15) resulted in a SPM (using a FWER correction with p-value<0.05 and k-threshold of 27 voxels). Fig. 32 shows each map with the corresponding RTC. Each label on the left of the matrix has the form of '**Idx**: RTC**#_size**' or '**Idx**: RTC**#_size**_c', where **Idx** represents the index of the label, **#** the number of the RTC that produced the SPM, **size** stands for the size of the cluster being analyzed, and c means contralateral cluster. This labeling stands for all patients. The temporal profile of the remaining RTCs are presented in **Appendix C**. The maps from RTC 1 and RTC 15 show extensive and diffuse activation on anterior and posterior brain areas, respectively, thus, these maps were excluded from further analysis. RTC_5's map shows four well defined activated regions, comprising the following brain regions: left temporal cortex, left superior occipital cortex, left lingual gyrus and right parahippocampal gyrus. Finally, the map corresponding to RTC_7 show one activation spot on the calcarine fissure. The content, regarding the number and size of clusters, of each SPM are presented in Table 2 . Each cluster are reported individually in **Appendix C**.

RTC	# clusters	Size of clusters
5	4	30 (2 clusters), 31, 36
7	1	38

Table 2- Number and size of the clusters presented in each SPM of patient 1.

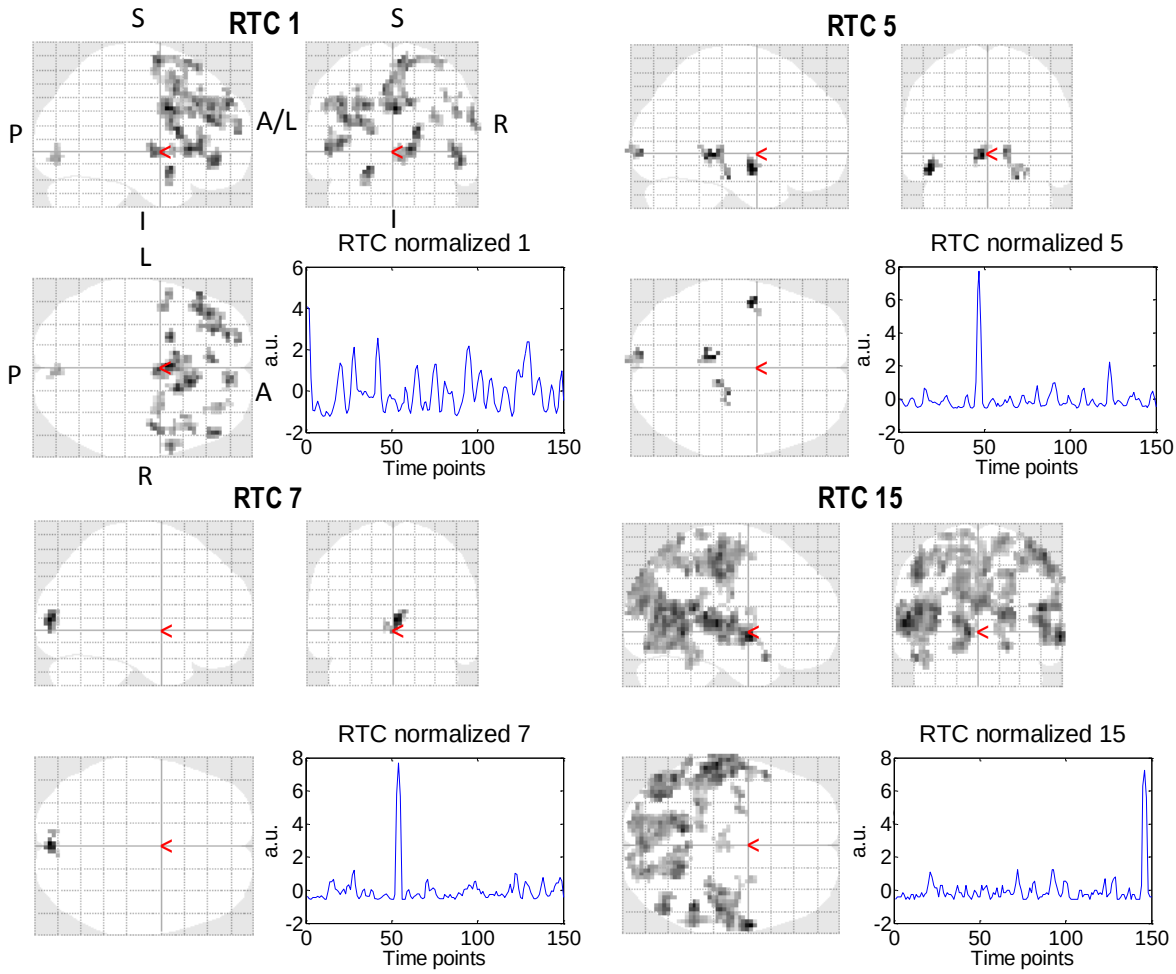

Fig. 32- Activation maps from RTC_1, RTC_5, RTC_7 and RTC_15 obtained using 2dTCA (FEWR correction, p-value<0.05, k-threshold=27 voxels) and corresponding RTCs' temporal profiles. Results for patient 1. S: superior; I: inferior; A: anterior; P: posterior; R: right; L: left.

The correlation between each ipsi and contralateral clusters of RTC_5 and RTC_7 are shown in Fig. 33. Regarding the RTC_5, the results show positive correlations between the ipsilateral, between ipsi and contralateral, and, also, between contralateral (although weaker) clusters' mean time courses. The ipsilateral cluster obtained from RTC_7's map has a strong positive correlation with the corresponding contralateral cluster mean time course.

The distribution of the mean CI and α across each cluster of RTC_5 and the CI and α for the ipsi and contralateral cluster of RTC_7 is shown in Fig. 34. RTC_5 has a higher mean CI and a lower mean α than RTC_7. Comparing the ipsi and contralateral clusters' mean complexity parameters, it is shown that the major difference is assigned to the RTC_5 (contralateral CI > ipsilateral CI) and the minor difference is assigned to the RTC_7 (contralateral CI ≈ ipsilateral CI).

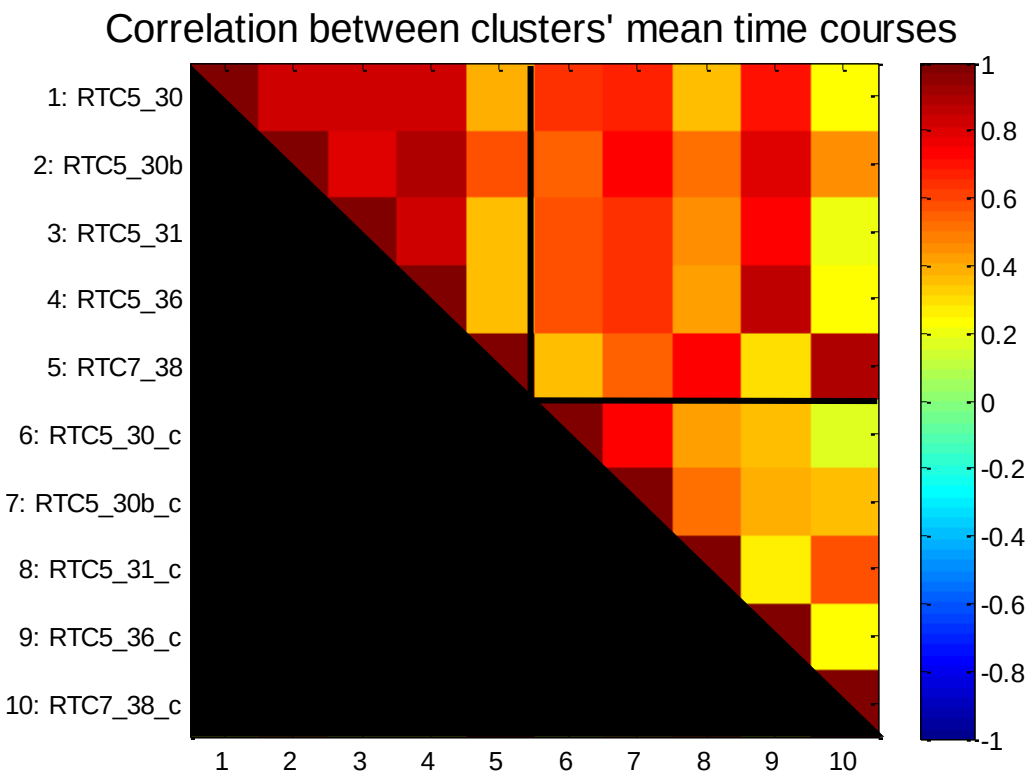

Fig. 33- Correlation matrix between ipsi and contralteral clusters of all RTCs that produced SPMs with significant activation. Results for patient 1. Each label on the left of the matrix as the form of '**Idx**: RTC**#_size**' or '**Idx**: RTC**#_size**_c', where **Idx** represents the index of the label, **#** the number of the RTC that produced the SPM, **size** stands for the size of the cluster being analyzed, and c means contralateral cluster. On the bottom of the matrix are the labels with the same indexes as those presented on the left.

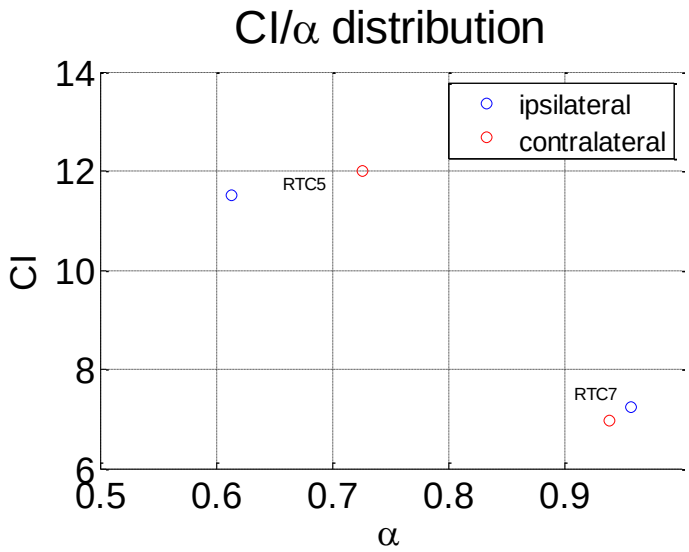

Fig. 34- Distribution of the mean CI and α across each cluster of RTC 5 and the CI and α for the ipsi and lateral cluster of RTC 7. At blue are the mean parameters for ipsilateral clusters and at red are the mean parameters for contralateral clusters. Results for patient 1.

The cluster RTC7_38 was excluded from further analysis (reason: localization on brain midline). The mean time course of the cluster considered for further analysis and the corresponding RTC temporal profile are presented in **Appendix C**.

Anisotropy analysis of each cluster considered for further analysis is shown in Fig. 35. The ones whose anisotropy fall on target regions (see bottom right chart on Fig. 29) are RTC5_30, RTC5_30b, and RTC5_36. Analyzing the CI/α distribution in Fig. 36, it is shown that contralateral clusters of RTC5_30, RTC5_30b, and RTC5_36 have higher α value than those of ipsilateral ones. Once α anisotropy analysis of the three clusters show a similar value (around -3), the potential epileptogenic focus was chosen according to the larger absolute CI anisotropy. Then chosen cluster is RTC5_30.

Lastly, Fig. 37 shows the functional connectivity analysis results of RTC5_30 (the potential epileptogenic focus chosen by complexity analysis) in z-score and thresholded at ±0.51. The results demonstrate that there are positive correlations between the RTC5_30 region (left middle and superior temporal gyrus), and right and left temporal poles, regions of the limbic system (right thalamus, right caudate nucleus, left and right parahippocampal gyrus, left and right hippocampus), right and left insula, right anterior cingulate and paracingulate gyri, left calcarine, right Heschl gyrus, left and right Rolandic operculum. Also negative correlations were observed between RTC5_30 and right lingual gyrus, right precuneus, right precentral gyrus, and left and right supplementary motor areas.

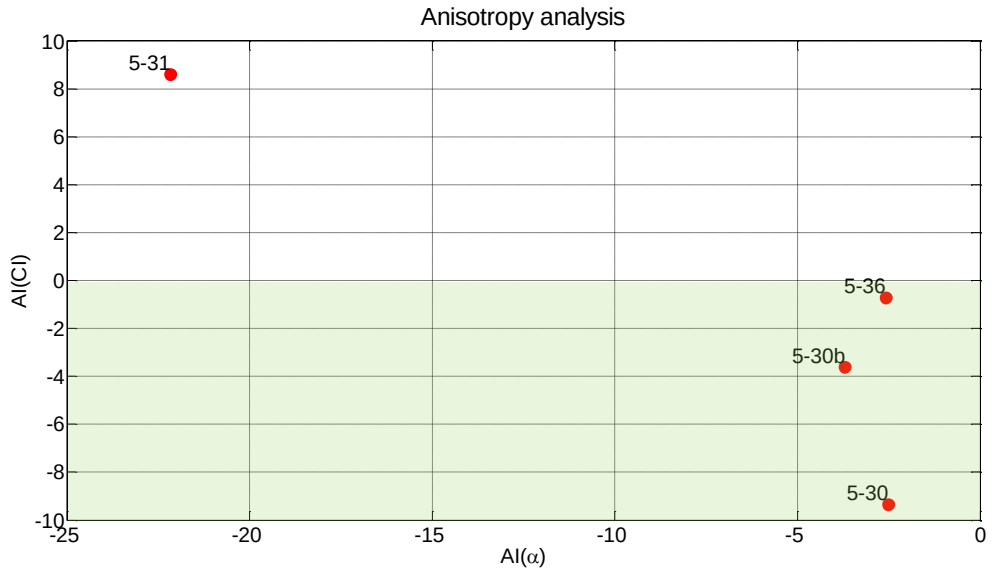

Fig. 35- Anisotropy analysis of each cluster considered for further analysis. At green is the target region. Each red point is labeled in the following way: 'Number of the RTC'-'Size of the RTC'. Results for patient 1.

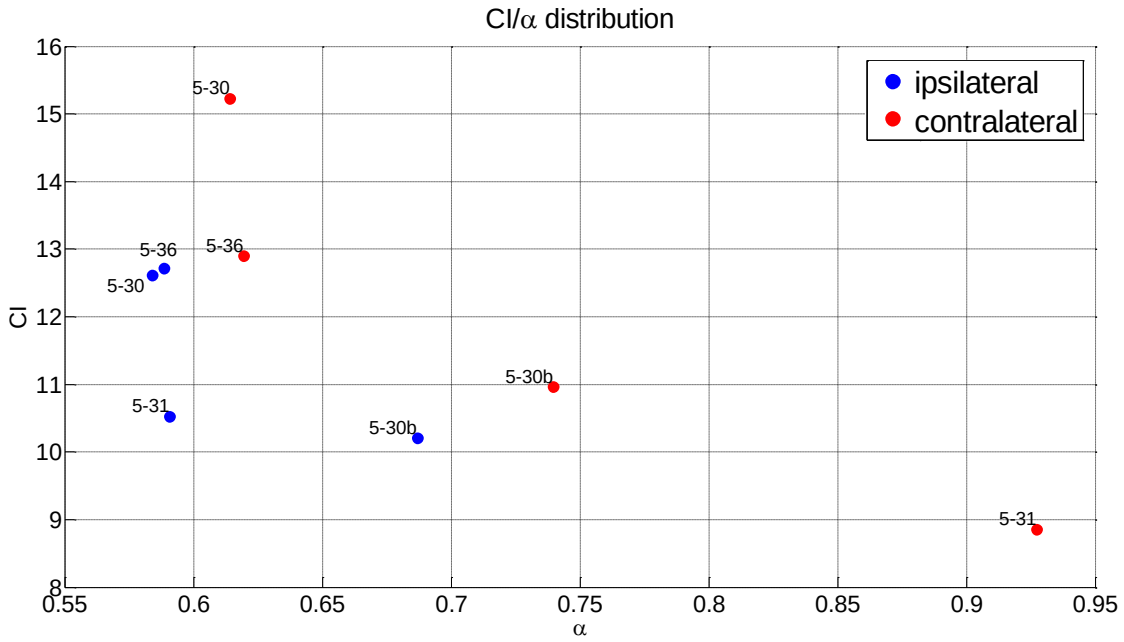

Fig. 36- CI/α distribution of each cluster considered for further analysis. Each red point is labeled in the following way: 'Number of the RTC'-'Size of the RTC'. Results for patient 1.

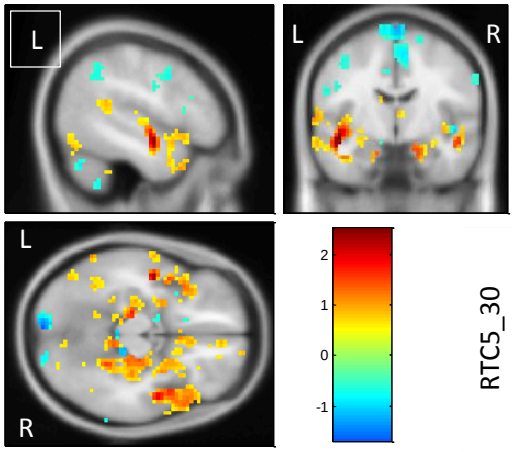

Fig. 37- Functional connectivity maps of RTC5_30 (the potential epileptogenic focus chosen by complexity analysis) in z-score and thresholded at ±0.51. Results for patient 1. L: left; R: right.

5.3.2. Patient 2 – Bilateral TLE: with right temporo-parietal predominance

Fig. 38 shows the histogram of the distribution of the number of voxels across the values of the transient spike selection limit. The results show that 2.8% of the voxels are above the 3% of signal change and 71.6% of the voxels are between the lower and upper boundaries (0.5 and 3% of signal change, respectively; see red dashed lines on Fig. 38).

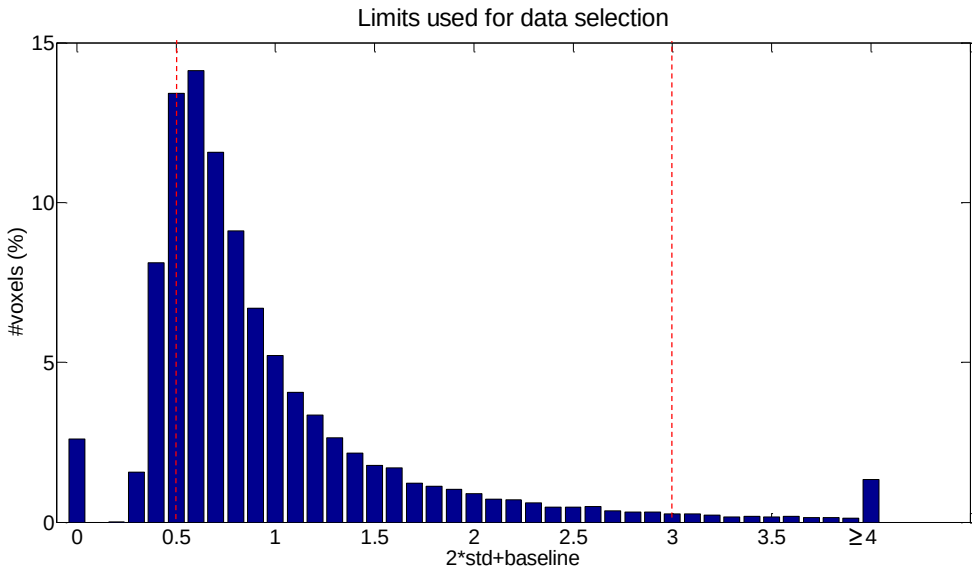

Fig. 38- Histogram showing the distribution of the number of voxels with a given value of the transient spike selection limit [2 standard deviations (std) above the baseline] for patient 2. Red dashed lines represents the lower and upper boundaries of allowed signal change (see **Chapter 2: 2.2.2 Algorithm implementation – Candidate voxels selection**).

The result of the bi-dimensional histogram mapping and its diagonal profile are shown on Fig. 39. Each column of this histogram represents a RTC, a total of 140 RTCs.

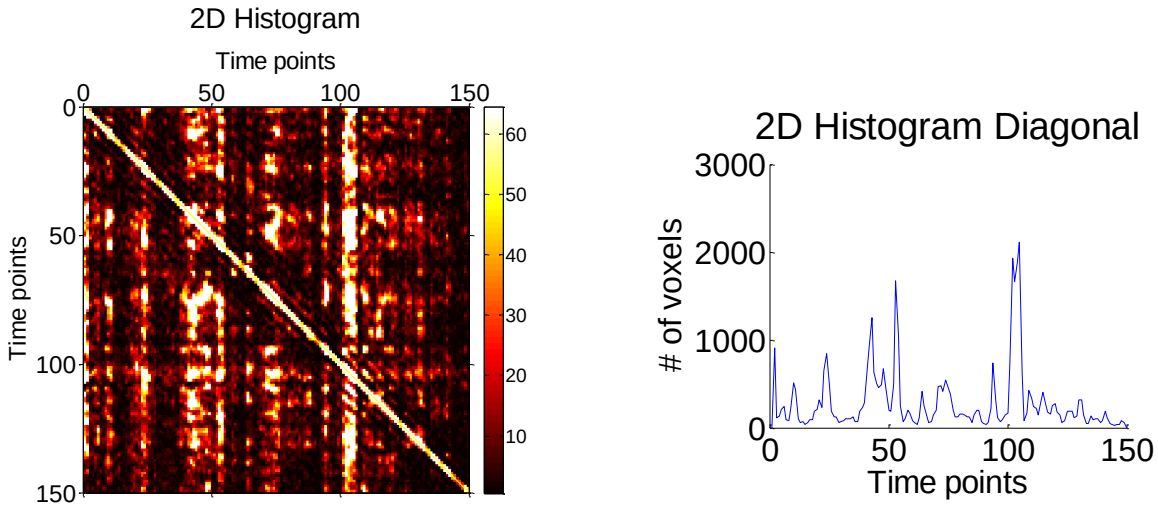

Fig. 39- Results for patient 2. **Left:** bi-dimensional histogram with the counting of transient spikes over the time. Each column represents a preliminary RTC. **Right** diagonal profile representing the number of voxels which maximum occurs in each time point.

After performing the RTCs number reduction and its normalization 15 RTCs remained for statistical analysis. From those 15 RTCs only 6 (RTC_1, RTC_2, RTC_3, RTC_5, RTC_10, and RTC_14) resulted in a SPM (using a FWER correction with p-value<0.05 and k-threshold of 27 voxels). Fig. 40 shows each map with the corresponding RTC. The temporal profile of the remaining RTCs are presented in **Appendix C**. The map from RTC_1 shows extensive activation comprising bilateral sensoriomotor areas, superior frontal lobe, median cingulate and paracingulate gyri, and precuneus. Due to the extent of activation this map, it was excluded from further analysis. RTC_2's map shows one single brain region with significant activation on the right superior temporal gyrus. The map corresponding to RTC_3 shows activation in three defined regions comprising the right inferior frontal gyrus, left middle occipital gyrus, and right inferior temporal gyrus. RTC_5's map activation covers left middle and superior temporal gyri, left inferior and superior frontal gyri, left precental region, and left cuneus and precuneus regions. RTC_10's map shows activation in right inferior frontal, in right inferior parietal gyri, and in right supramarginal gyrus. Finally, the map corresponding to RTC_14 shows activation mainly in the right temporal lobe. The content, regarding the number and size of clusters, of each SPM are presented in Table 3 . Each cluster are reported individually in **Appendix C**.

RTC	# clusters	Size of clusters
2	1	58
3	3	50, 93, 100
5	8	28, 28b, 35, 44, 76, 113, 125, 140
10	2	33, 92
14	3	27, 48, 115

Table 3- Number and size of the clusters presented in each SPM of patient23.

The correlation between each ipsi and contralateral clusters of RTC_2, RTC_3, RTC_5, RTC_10 and RTC_14 are shown in Fig. 41. In general, ipsilateral clusters of the same RTC's map show strong positive correlations between them and with corresponding contralateral clusters. The ipsilateral cluster of RTC_2 shows positive correlations with the ipsilateral clusters of RTC_5 that, in turn, show positive correlations with contralateral clusters of RTC_14.

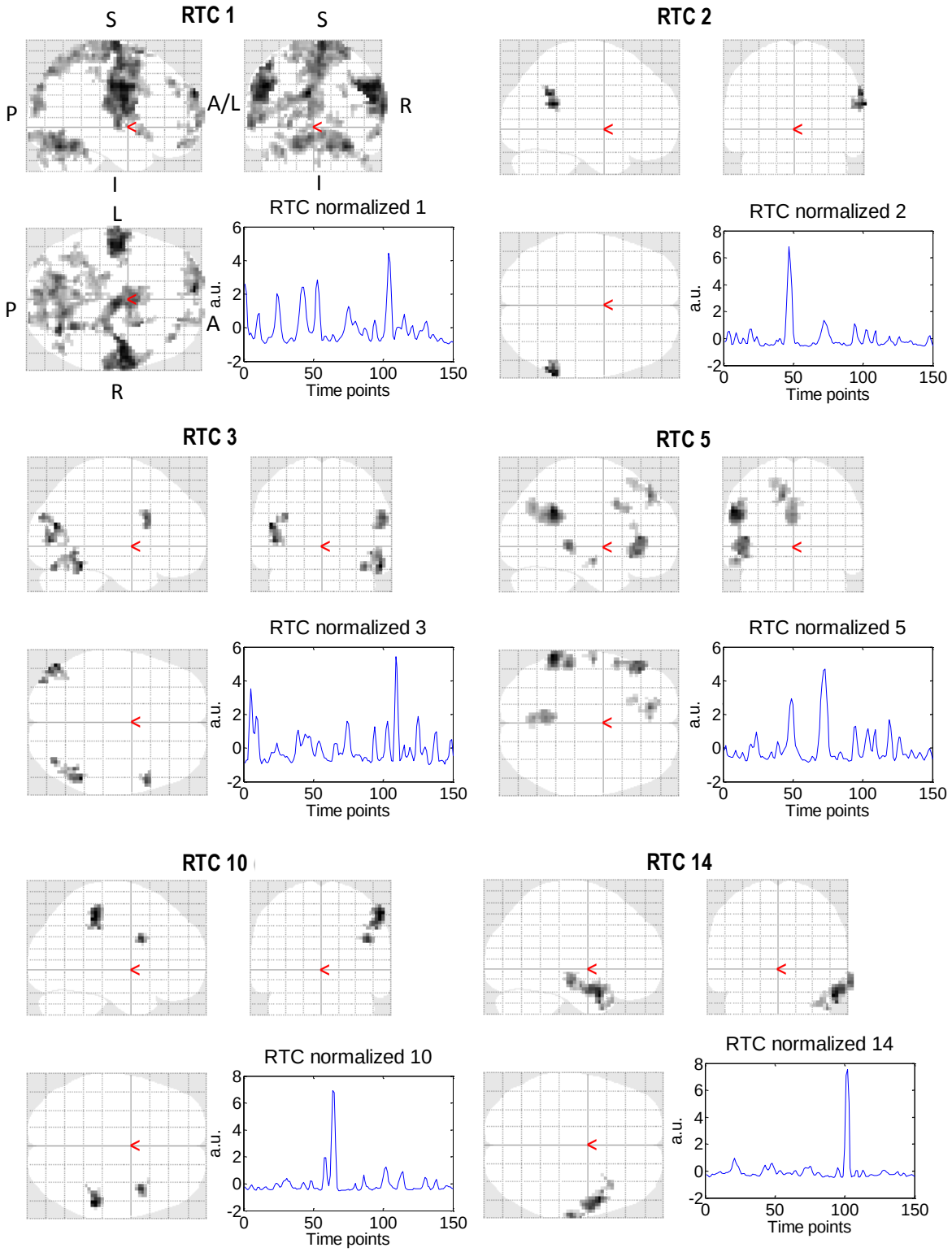

Fig. 40- Activation maps from RTC_1, RTC_2, RTC_3, RTC_5, RTC_10, and RTC_14 obtained using 2dTCA (FEWR correction, p-value<0.05, k-threshold=27 voxels) and corresponding RTCs' temporal profiles. Results for patient 2. S: superior; I: inferior; A: anterior; P: posterior; R: right; L: left.

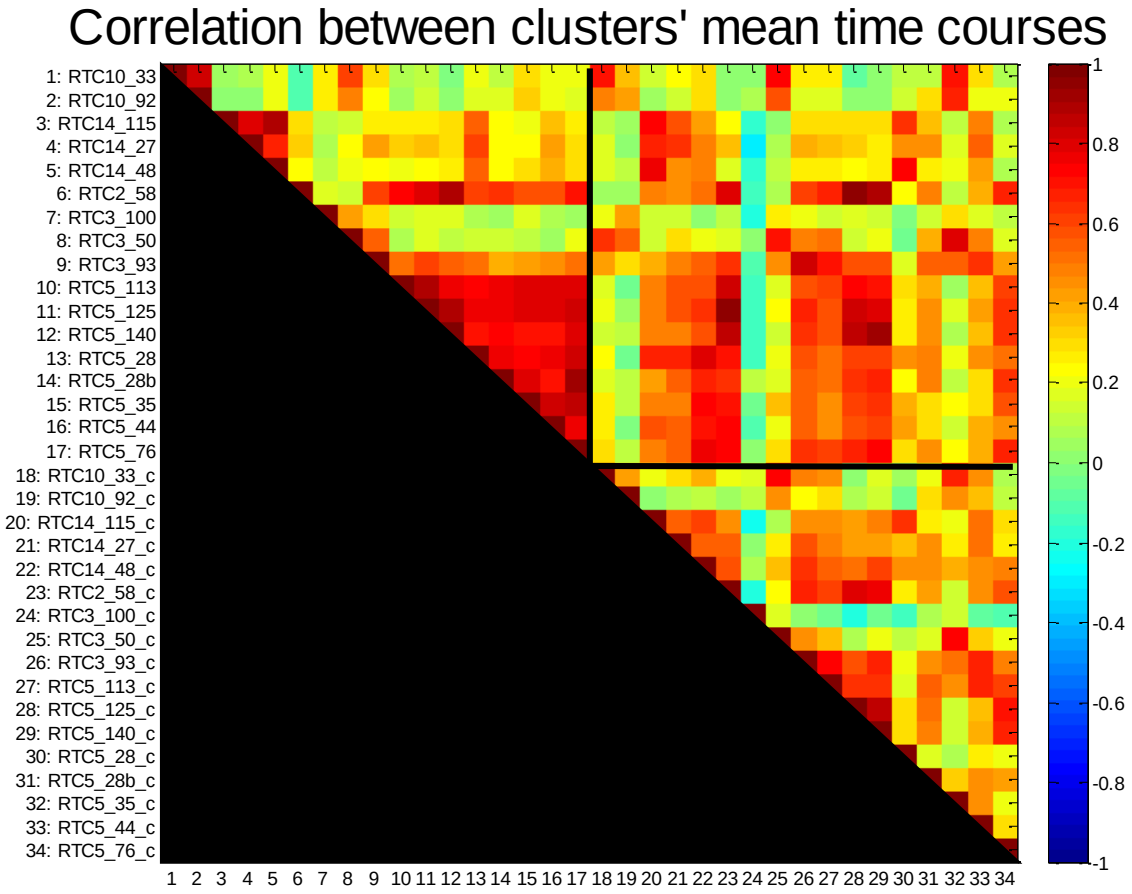

Fig. 41- Correlation matrix between ipsi and contralteral clusters of all RTCs that produced SPM with significant activation. Results for patient 2. Each label on the left of the matrix as the form of '**Idx**: RTC**#_size**' or '**Idx**: RTC**#_size**_c', where **Idx** represents the index of the label, **#** the number of the RTC that produced the SPM, **size** stands for the size of the cluster being analyzed, and c means contralateral cluster. On the bottom of the matrix are the labels with the same indexes as those presented on the left.

The distribution of the mean CI and α across each cluster of RTC_3, RTC_5, RTC_10, and RTC_14 and the CI and α for the ipsi and contralateral clusters of RTC_2 is shown in Fig. 42. RTC_2, RTC_5, and RTC_10 show both contralateral CI higher and α lower than ispsilateral one. The opposite result is shown for RTC_14. Regarding he RTC_3's CI is higher for ipsilateral cluster than for that of contralateral one, with a constant α. Also, the major difference between ispi and contralateral clusters' mean complexity parameters is assigned to RTC_10.

The following clusters were excluded from further analysis: RTC2_58 (reason: it is contralateral to RTC5_125), RTC3_50 (reason: it is contralateral to RTC5_113), and RTC3_100 (reason: it is contralateral to RTC5_125). Also, all clusters of RTC 14 were excluded since the single spike of the corresponding RTC and clusters' mean time course corresponds to a motion artefact (see movement

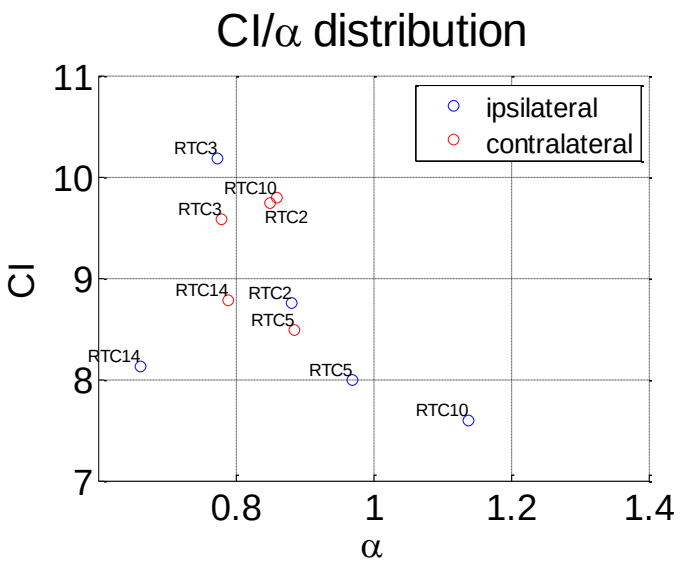

Fig. 42- Distribution of the mean CI and α across each cluster of RTC_3, RTC_5, RTC_10, and RTC_14 and the CI and α for the ipsi and contralateral cluster of RTC_2. At blue are the mean parameters for ipsilateral clusters and at red are the mean parameters for contralateral clusters. Results for patient 2.

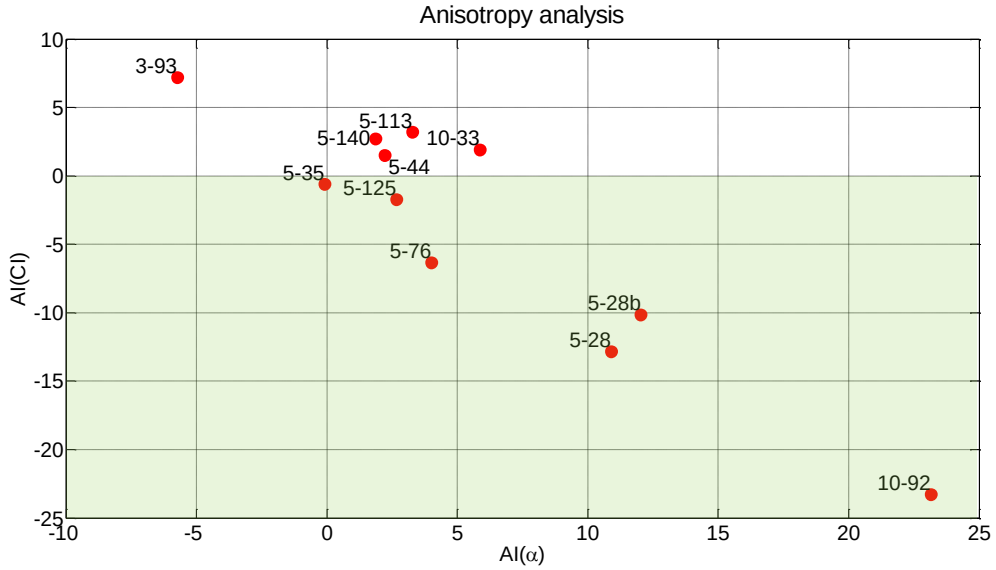

Fig. 43- Anisotropy analysis of each cluster considered for further analysis. At green is the target region. Each red point is labeled in the following way: 'Number of the RTC'-'Size of the RTC'. Results for patient 2.

parameters and mean time course of the RTC_14's clusters plot in **Appendix C**). The mean time courses of the clusters considered for further analysis and the corresponding RTC temporal profiles are presented in **Appendix C**.

Anisotropy analysis of each cluster considered for further analysis is shown in Fig. 43. The clusters whose anisotropy fall on target regions (see bottom right chart on Fig. 29) are RTC5_35, RTC5_125, RTC5_76, RTC5_28b, RTC5_28, and RTC10_92. Analyzing the CI/α distribution in Fig. 44, it is shown that the contralateral cluster of RTC10_92 has higher CI and lower α values than those of the remaining RTCs which AI fall on target regions. Therefore, the potential epileptogenic focus was chosen as the one which has lower CI anisotropy and, at the same time, higher α anisotropy, i.e., RTC10_92.

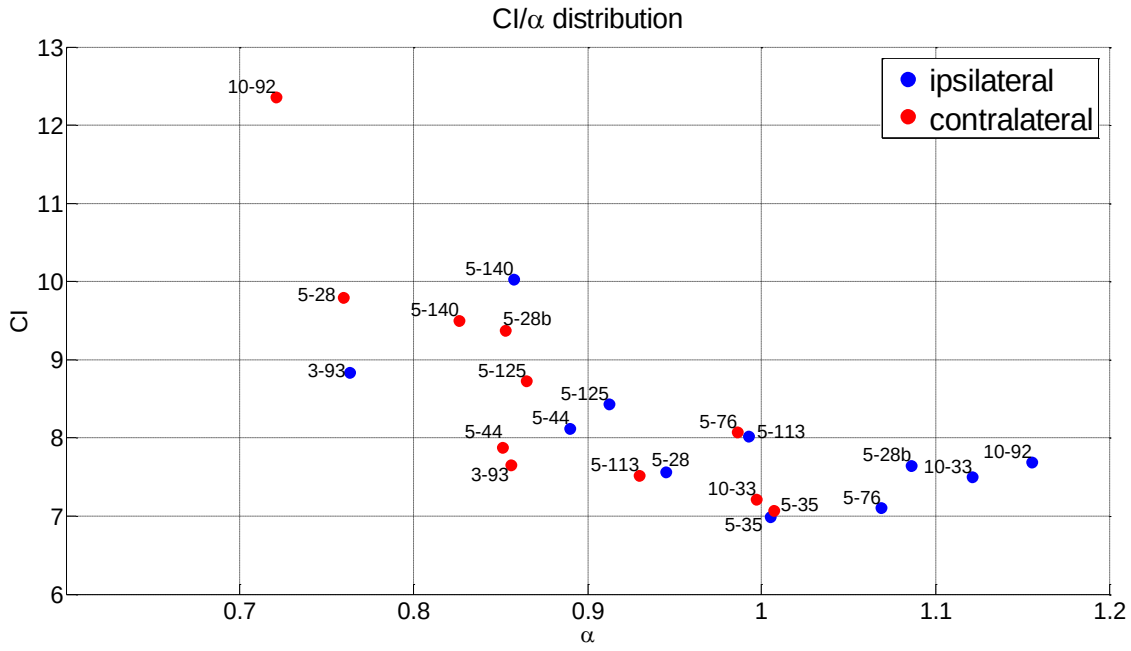

Fig. 44- CI/α distribution of each cluster considered for further analysis. Each red point is labeled in the following way: 'Number of the RTC'-'Size of the RTC'. Results for patient 2.

Lastly, Fig. 45 shows the functional connectivity analysis results of RTC10_92 (the potential epileptogenic focus chosen by complexity analysis) in z-score and thresholded at ±0.4. The results demonstrate that there are some positive correlations between RTC10_92 cluster and its contralateral region and also correlation with opercular and orbital parts of right inferior frontal gyrus, left and right median and anterior cingulates and paracingulates gyri, left and right inferior temporal gyri and right superior temporal gyrus.

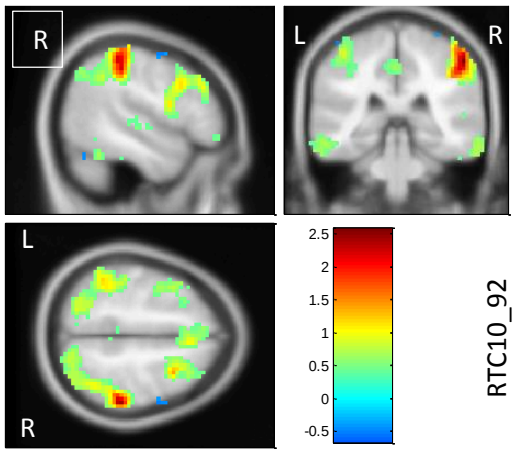

Fig. 45- Functional connectivity maps of RTC10_92 (the potential epileptogenic focus chosen by complexity analysis) in z-score and thresholded at ±0.4. Results for patient 2. L: left; R: right.

5.3.3. Patient 3 – Focal Cortical Dysplasia Epilepsy (FCDE): right precentral gyrus

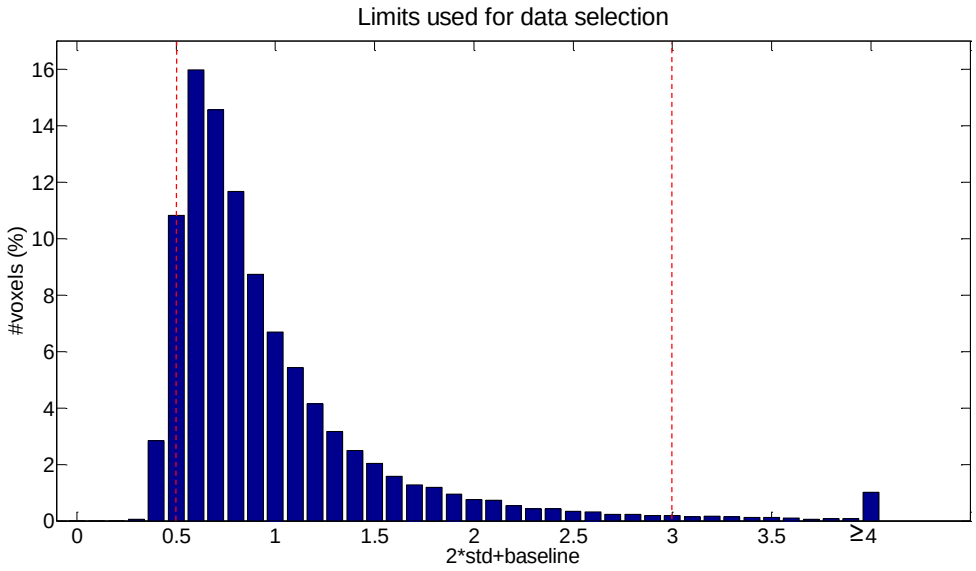

Fig. 46- Histogram showing the distribution of the number of voxels with a given value of the transient spike selection limit [2 standard deviations (std) above the baseline] for patient 3. Red dashed lines represents the lower and upper boundaries of allowed signal change (see **Chapter 2: 2.2.2 Algorithm implementation – Candidate voxels selection**).

Fig. 46 shows the histogram of the distribution of the number of voxels across the values of the transient spike selection limit. The results show that 2.1% of the voxels are above the 3% of signal change and 96.1% of the voxels are between the lower and upper boundaries (0.5 and 3% of signal change, respectively; see red dashed lines on Fig. 46).

The result of the bi-dimensional histogram mapping and its diagonal profile are shown on Fig. 47. Each column of this histogram represents a RTC, a total of 140 RTCs.

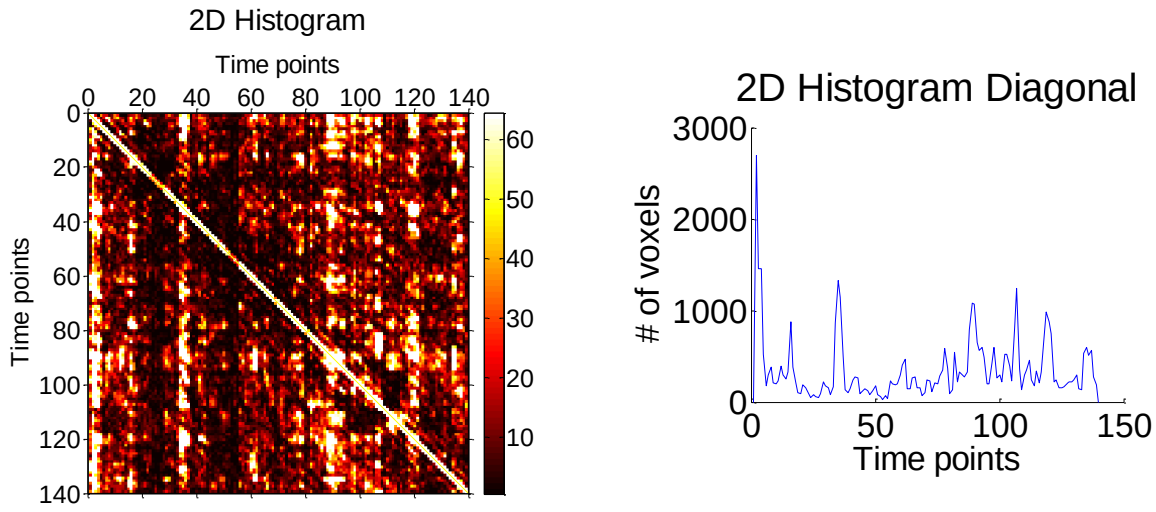

Fig. 47- Results for patient 3. **Left:** bi-dimensional histogram with the counting of transient spikes over the time. Each column represents a preliminary RTC. **Right** diagonal profile representing the number of voxels which maximum occurs in each time point.

After performing the RTCs number reduction and its normalization 11 RTCs remained for statistical analysis. From those 11 RTCs only 4 (RTC_1, RTC_3, RTC_4, and RTC_11) resulted in a SPM (using a FWER correction with p-value<0.05 and k-threshold of 27 voxels). Fig. 48 shows each map with the corresponding RTC. The temporal profiles of the remaining RTCs are presented in **Appendix C**. Particularly, for RTC_1 the map shows activation in posterior-inferior brain regions, including the cerebellum. The RTC_3's map shows an extensive activation comprising bilateral sensoriomotor areas. The map of RTC_4 shows three activated regions, comprising left and right inferior and superior parietal gyri, right angular gyrus, and right precentral gyrus. The map of RTC_11 shows two clusters on the left cerebrum, namely on the left middle frontal gyrus, left angular gyrus, left inferior parietal gyrus, and precuneus. The content, regarding the number and size of clusters, of each SPM are presented in Table 4 . Each cluster is reported individually in **Appendix C**.

RTC	# clusters	Size of clusters
1	6	28, 34, 42, 80, 81, 132
3	5	64, 136, 170, 275, 354
4	3	55, 87, 123
11	2	39, 166

Table 4- Number and size of the clusters presented in each SPM of patient 3.

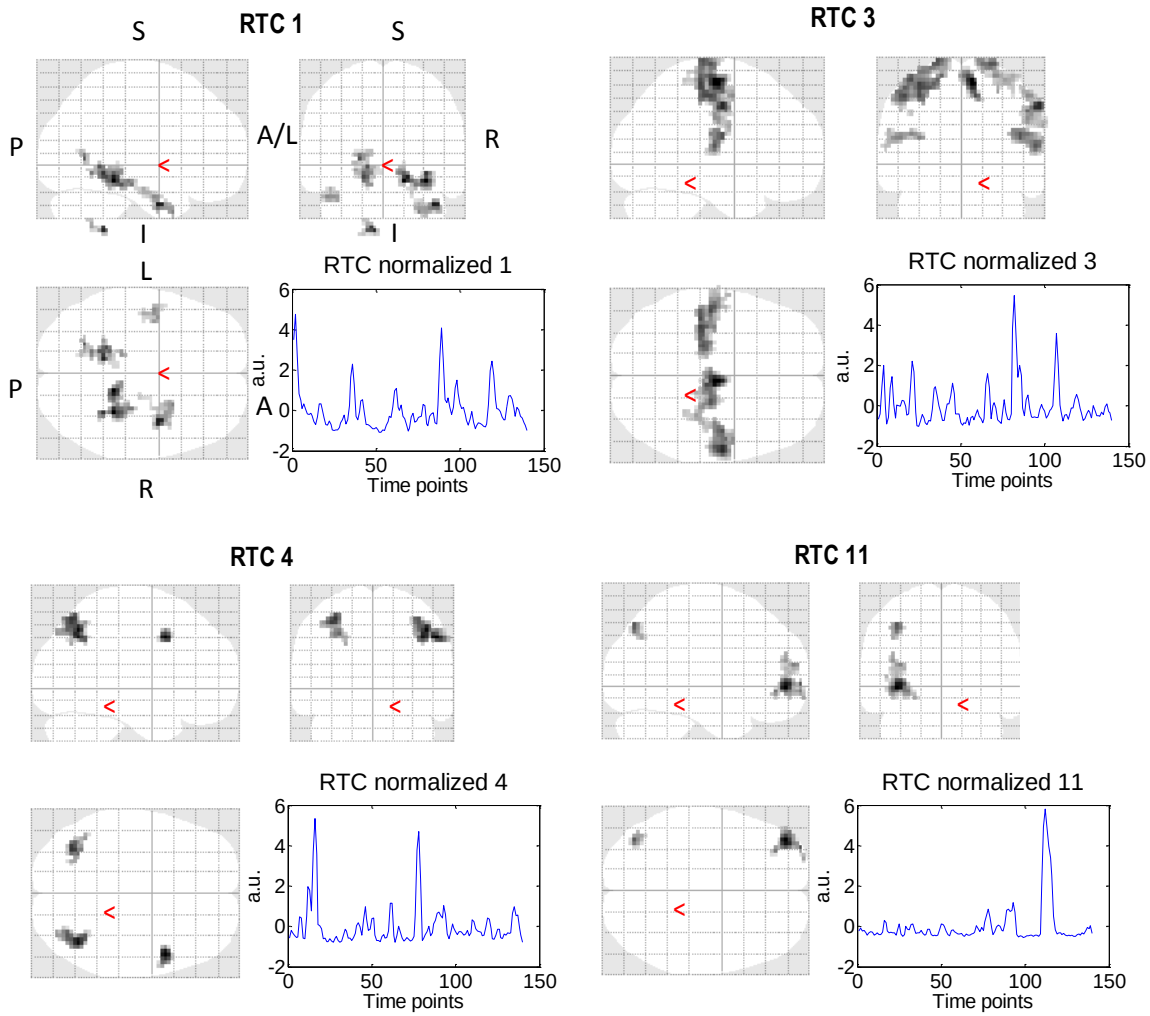

Fig. 48- Activation maps from RTC_1, RTC_3, RTC_4 and RTC_11 obtained using 2dTCA (FEWR correction, p-value<0.05, k-threshold=27 voxels) and corresponding RTCs' temporal profiles. Results for patient 3. S: superior; I: inferior; A: anterior; P: posterior; R: right; L: left.

The correlation between each ipsi and contralateral clusters are shown in Fig. 49. Regarding the RTC 1, the results show positive correlations between the ipsilateral clusters' mean time courses and, also, between those of ipsi and some contralateral clusters (RTC1_132_c, RTC1_28_c and RTC1_81_c). It is also shown negative correlations between ipsilateral clusters' mean time course and that of a contralateral cluster (RTC_1_80). Concerning the RTC_3, the results show strong positive correlations between the ipsi and contralateral clusters' mean time courses. Lastly, the ipsi and contralateral clusters' mean time courses of RTC_4 and RTC_11 show positive correlations between them.

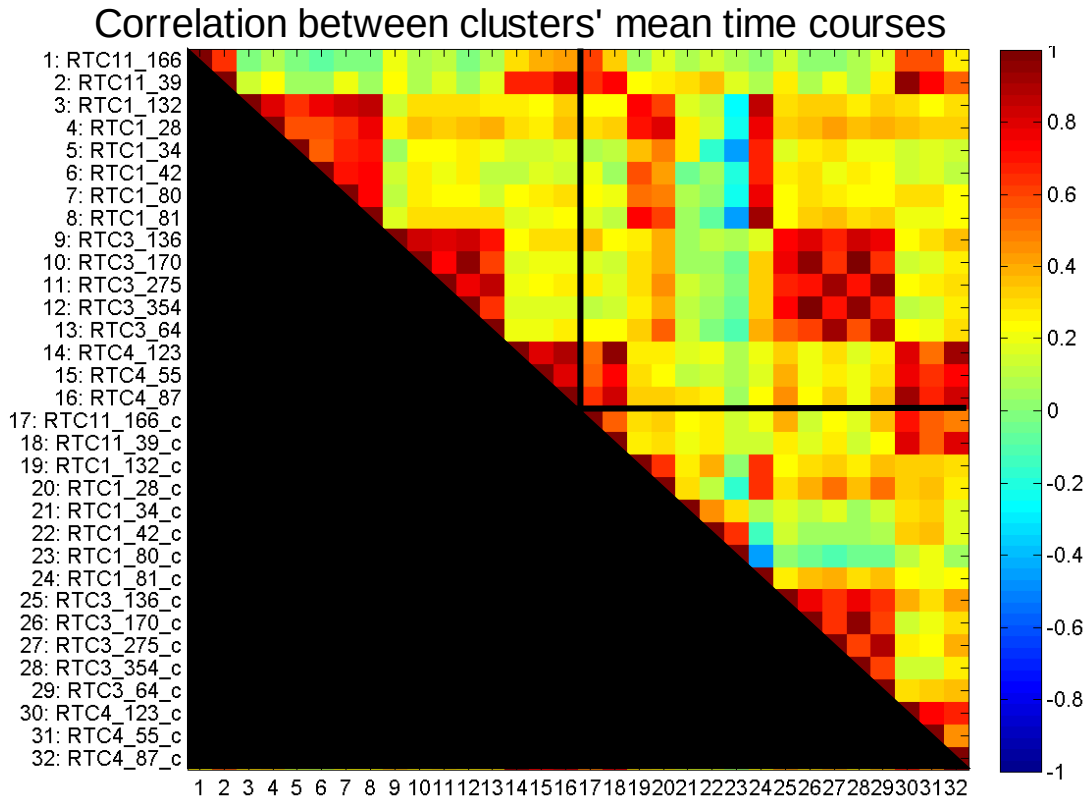

Fig. 49- Correlation matrix between ipsi and contralteral clusters of all RTCs that produced SPM with significant activation. Results for patient 3. Each label on the left of the matrix as the form of '**Idx**: RTC**#_size**' or '**Idx**: RTC**#_size**_c', where **Idx** represents the index of the label, **#** the number of the RTC that produced the SPM, **size** stands for the size of the cluster being analyzed, and **c** means contralateral cluster. On the bottom of the matrix are the labels with the same indexes as those presented on the left.

In Fig. 50 the distribution of the mean CI and α across each cluster of RTC_1, RTC_3, RTC_4, and RTC_11 is shown. RTC_1 has a higher mean CI and a lower mean α than RTC_3 that, in turn, have a higher CI and lower α than RTC_4 and RTC_11. These last two have a similar complexity parameters values. Comparing the ipsi and contralateral clusters' mean complexity parameters, it is shown that the major difference is assigned to the RTC_1 (contralateral CI < ipsilateral CI) and the minor difference is assigned to the RTC_3 (contralateral CI ≈ ipsilateral CI).

The following clusters were excluded from further analysis: RTC1_80 (reason: localization on cerebellum), RTC1_81 (reason: it is contralateral to RTC1_132), all clusters from RTC 3 (reason: these clusters represents contralateral regions), and RTC4_87 (reason: it is contralateral to RTC4_123). The mean time course of the clusters considered for further analysis and the corresponding RTC temporal profiles are presented in **Appendix C**.

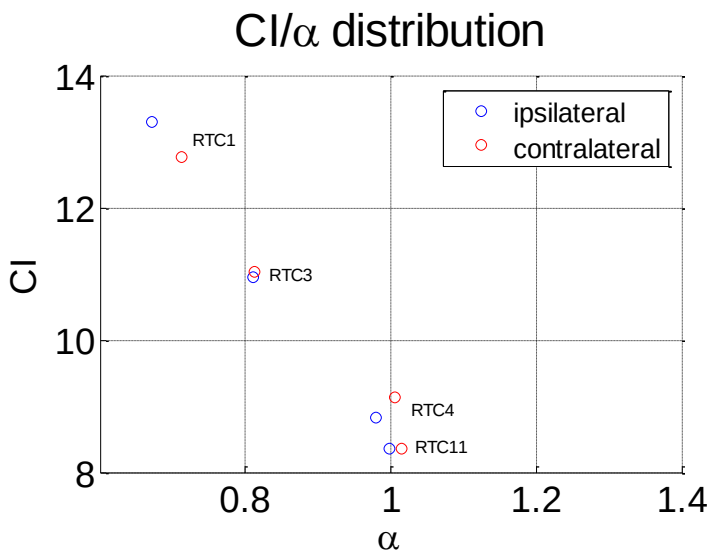

Fig. 50- Distribution of the mean CI and α across each cluster of RTCs 1, 3, 4, and 11. At blue are the mean parameters for ipsilateral clusters and at red are the mean parameters for contralateral clusters. Results for patient 3.

Anisotropy analysis of each cluster considered for further analysis is shown in Fig. 51. The ones whose anisotropy fall on target regions (see bottom right chart on Fig. 29) are RTC1_28 and RTC11_39. Analyzing the CI/α distribution in Fig. 52, it is shown that RTC11_39 have lower CI values (either for ispi and contralateral clusters) than those of RTC1_28. Thus, from this two clusters, the chosen potential epileptogenic focus is RTC11_39.

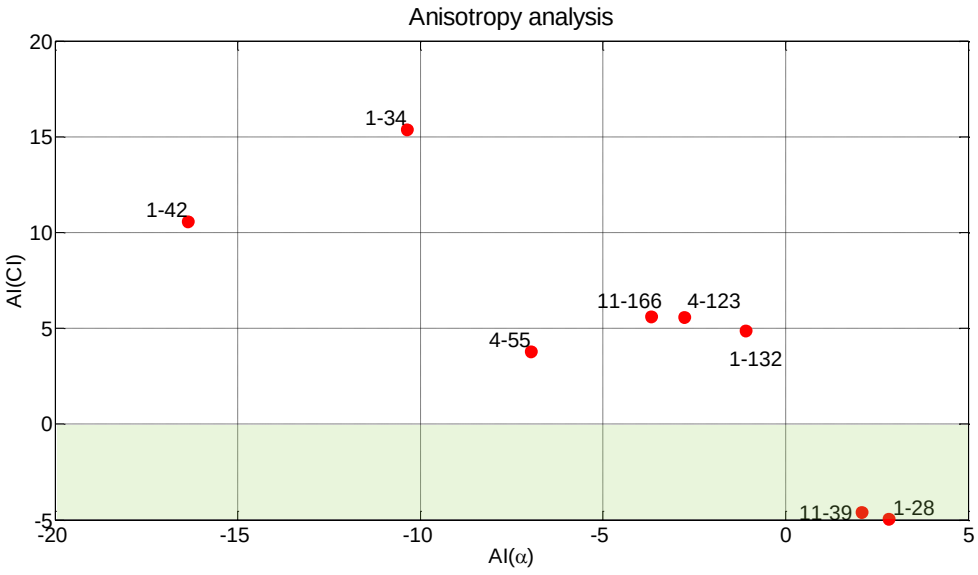

Fig. 51- Anisotropy analysis of each cluster considered for further analysis. At green is the target region. Each red point is labeled in the following way: 'Number of the RTC'-'Size of the RTC'. Results for patient 3.

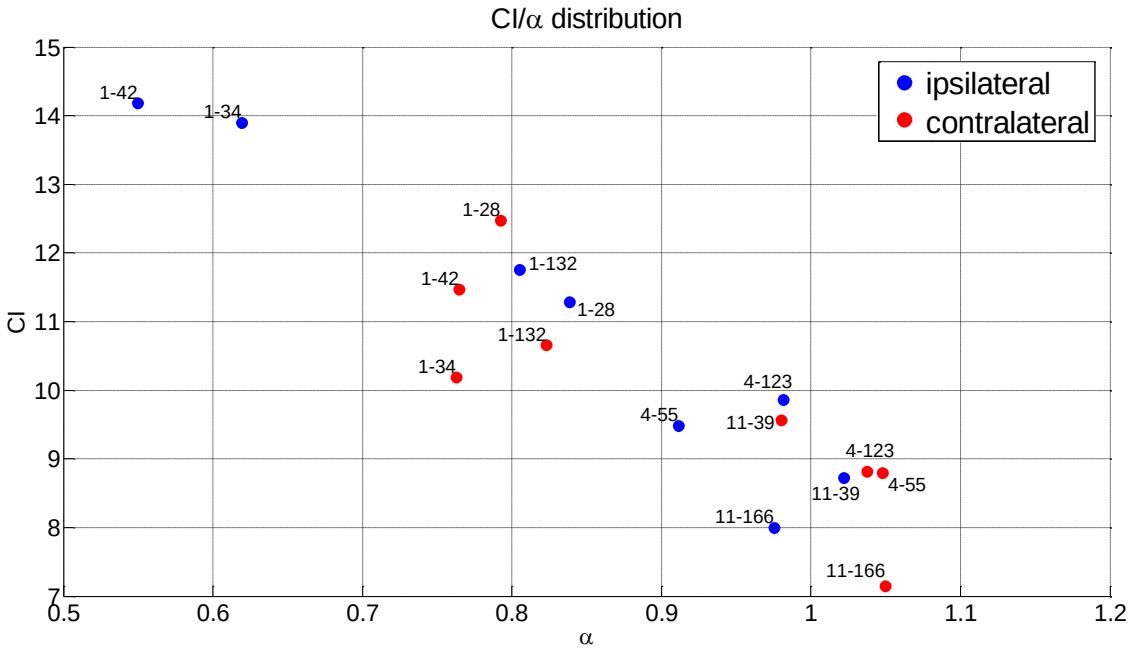

Fig. 52- CI/α distribution of each cluster considered for further analysis. Each red point is labeled in the following way: 'Number of the RTC'-'Size of the RTC'. Result for patient 3.

Lastly, Fig. 53 shows the functional connectivity analysis results of RTC11_39 (the potential epileptogenic focus chosen by complexity analysis) and RTC4_55 (the cluster that best described the anatomical brain region with lesion) in z-score and thresholded at ±0.36 and ±0.46, respectively. The results demonstrate positive correlations between the same brain regions in the two maps, including left and right angular gyri, left and right precuneus, left and right precentral gyri, and left and right middle and superior frontal gyri.

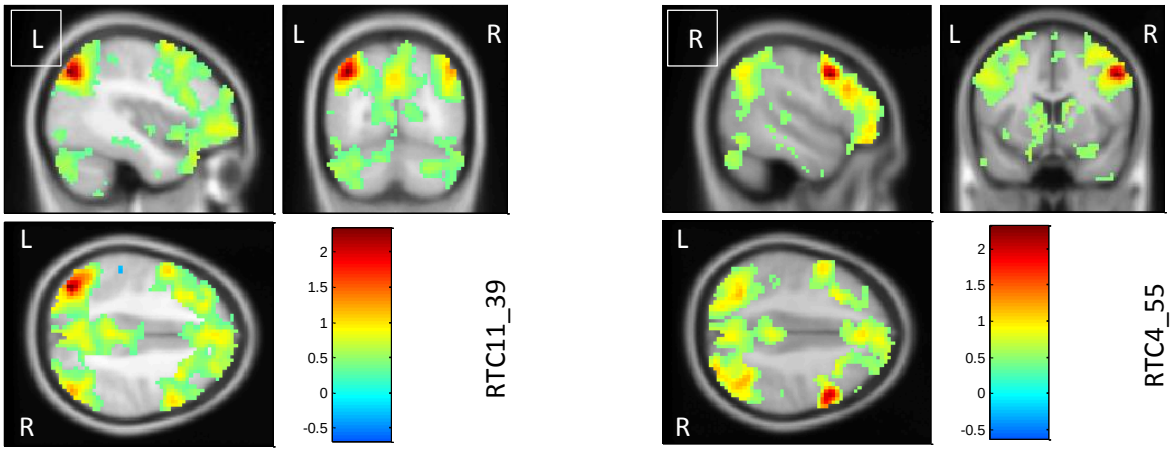

Fig. 53- Functional connectivity maps of RTC11_39 (the potential epileptogenic focus chosen by complexity analysis) and RTC4_55 (the cluster that best described the anatomical brain region with lesion) in z-score and thresholded at ±0.36 and ±0.46, respectively. Results for patient 3. L: left; R: right.

5.4. Discussion

In this section, a discussion about each patient results individually will take place followed by a general discussion about the methodological outcome of the present work.

5.4.1. Patient 1 – Unilateral TLE: left TLE

The analysis of the transient spike selection limits distribution (Fig. 30) showed that only 4.1 % of the 54837 of the voxels have a maximum signal change with a magnitude higher than 3 %. This indicates that, overall, data have a low amount of signal artefacts.

Concerning the maps of activation corresponding to the RTCs that showed significant activation, two of them showed extensive activation: RTC 1 and RTC 15. These results might be explained either by artefacts or by a synchronization of a network or networks. In fact, RTC 1 temporal profile have some spikes that are coincident with the ones present in the motion parameters plot (see **Appendix C**). Also, the distribution of activated brain regions of this RTC does not resemble any known network. Thus, this map might be derived from movement artefacts. On the other hand, the activation map corresponding to RTC 15 shows contiguous activation on brain regions assigned to visual areas (Shirer et al. 2012). As this map covers part of the temporal lobe, where epileptogenic activity is present, it could be associated to a synchrony of the visual network with the source of the epileptic activity.

The complexity analysis of the RTC 5 showed that RTC5_30 was the most likely epileptogenic focus having an ipsilateral CI value lower than the contralateral one and a CI anisotropy lower than the remaining clusters in the analysis (Fig. 35 and Fig. 36). This analysis showed also that ipsilateral RTC5_30 have α lower than the contralateral one, a result similar to that found for RTC4_55 of patient 3 with FCDE. In addition, the region covered by the cluster RTC5_30 overlapped the clinical information about the origin of the epileptic activity, the left temporal lobe, and anatomical imaging findings.

The analysis of the functional connectivity of this cluster showed negative correlations between RTC5_30 and sensoriomotor areas (right precentral gyrus and left and right supplementary motor areas). It also showed positive correlations with regions that might be associated with an epileptic network conducted by the epileptogenic focus. These results support the idea that the epileptogenic focus may spread its activity to regions functionally connected to it influencing them either in a positive or in a negative way.

5.4.2. Patient 2 – Bilateral TLE: with right temporo-parietal predominance

The distribution of the limits for transient spike selection of each voxel (Fig. 38) showed that only 2.8 % of the 54837 of the voxels have a maximum signal change with a magnitude higher than 3 %. As for patients 1, this indicates that, overall, data have a low amount of signal artefacts.

The number of RTC's maps with significant activation was higher for this patient than for the others (6 RTCs comparatively to 4 RTCs). The map corresponding to RTC 1 showed extensive activation among regions that resembles the sensoriomotor network (Shirer et al. 2012). RTC 14 represents an example showing the ability of 2dTCA algorithm to sort out temporal profiles derived from artefacts events. Even when these events have characteristics within the limits imposed (a transient spike that have a magnitude 2 standard deviations above the baseline and with a percentage change between 0.5 and 3 %), this algorithm is able to separate them from another type of activity, allowing the user to exclude them from further analysis.

The complexity analysis of RTCs' clusters for this patient showed that RTC10_92 is the most likely epileptogenic focus having an ipsilateral CI value lower than the contralateral one and a CI anisotropy higher, in magnitude, than the remaining clusters in the analysis (Fig. 43 and Fig. 44). This was in agreement with clinical information which says that there is a prevalence of the epilepsy on the right temporal-parietal region (RTC10_92 comprises the right inferior parietal and supramarginal gyri). The functional connectivity analysis (Fig. 45) showed what might be the epileptic network generated by the epileptogenic focus, which comprises bilateral parietal and temporal regions, being consistent with the fact that this patient has bilateral TLE.

5.4.3. Patient 3 – FCDE: right precentral gyrus

Fig. 47 showed only 2.1 % of the 54837 voxels have a maximum signal change with a magnitude higher than 3 %. As for patient 1 and 2, this is a good indicator that data have a low amount of signal artefacts.

Regarding the RTCs that showed significant activation in the corresponding map, there is one, RTC 3, that showed activation in the sensorimotor areas, resembling the sensorimotor network (Shirer et al. 2012). The reason that this network is extensively activated even with the patient in resting state condition could be the fact that the epileptogenic focus of this patient is located on the right precentral gyrus, a primary motor area, which is covered by the network discussed above. The activity from this focus could influence all the other brain regions associated with this network. The

same line of reasoning could be used to interpret the results of the clusters' mean time courses complexity analysis.

Fig. 50 showed that in average the clusters from RTC4 and 11 have a lower CI and higher α than those of RTC1 and 3. On the other hand, anisotropy analysis (Fig. 51) showed that differences between ipsi and contralateral cluster complexity located in the region of interest (green shadow in the plot) occurs for RTC1_28 and RTC11_39. Further, a careful analysis of the complexity parameters (Fig. 52) demonstrated that RTC11_39 have lower CI and higher α than those of RTC1_28. This is in agreement with the results shown in Fig. 50. The most likely epileptogenic focus was chosen according to the hypothesis that epileptogenic BOLD signal have a lower entropy than the remaining BOLD signals. However, clinical information says that the brain lesion responsible for this epileptogenic activity lies on right precentral gyrus and not on left parietal cortex, respectively, RTC4_55 and RTC11_39.

The analysis of functional connectivity of RTC11_39 (the likely epileptogenic focus found by the method) and RTC4_55 (the one containing the brain region known to have a lesion) shows correlations between the same brain regions. This might mean that these two clusters belong to the same network possibly conducted by the epileptogenic activity generated from the focus. Also, the complexity analysis of RTC4_55 shows that the contralateral cluster, in the left hemisphere as RTC11_39, has lower CI and higher α than those of ipsilateral cluster.

Furthermore, the complexity values of ipsilateral RTC4_55 are similar to those of contralateral RTC11_39. On the other hand, the complexity values of contralateral RTC4_55 are similar to those of ipsilateral RTC11_39. This could further indicate that RTC4_55 and RTC11_39 belong to the same epileptic network which encompasses the right precentral gyrus known as the epileptogenic focus.

5.4.4. General Discussion

In this thesis project a biomarker for epileptic tissue identification was developed. This was accomplished by implementing and testing a method able to localize an epileptogenic focus using a non-invasive technique: BOLD signals from fMRI. It detects and aggregates brain regions with similar transient activity and characterize them in terms of its complexity using a combination of three distinct algorithms: 2dTCA, MSE and DFA. To the best of my knowledge this was the first work combining such techniques applied to epileptogenic fMRI data.

The methodology was tested using data from three epileptic patients with three types of epilepsy: unilateral temporal lobe epilepsy, bilateral temporal lobe epilepsy, and focal cortical dysplasia epilepsy. This study was an example of the interpretation process that could be done using the developed methodology. 2dTCA was used to find brain regions with different temporal behavior (with characteristics of interest) and then MSE and DFA were able to classify the same brain regions in terms of its complexity sorting them as a likely epileptogenic or non-epileptogenic focus.

Overall, the results showed that epileptogenic tissue has a temporal behavior different from non-epileptogenic one. The results obtained for TLE patients showed that the epileptogenic focus have lower entropy of BOLD signals than the corresponding contralateral regions, thus supporting the main findings in (Protzner et al. 2010). The EEG study on TLE patients of Protzner and colleagues showed that epileptogenic tissue has a lower complexity (lower entropy) than non-epileptogenic tissue. They also showed that in some patients the interictal activity passed from the ipsi to the contralateral brain hemisphere, which could justify the functional connectivity results.

The hypothesis of LRTC applied to epileptic BOLD signals could not be verified with the study conducted in this work due to the inconsistency of the results. The main findings of Parish et al (2004) and Monto et al. (2007) EEG studies, which says that LRTC are stronger in the epileptogenic focus, were only found in the patient with bilateral TLE.

Furthermore, in this study it was even possible to associate brain regions likely either to belong to epileptic networks or to influence other brain networks related to the epileptic activity onset. This could explain the LRTC results.

On the other hand, the complexity hypothesis was not verified for the FCDE patient. Although it was found a cluster covering the brain region with dysplasia, the complexity analysis showed that the entropy was higher for regions contralateral to the epileptogenic focus than for the epileptogenic focus itself. Indeed, the hypotheses on which this project is based are related to TLE and there is no signature assigned to FCDE concerning the MSE and DFA methods. Hereupon, a study with a sample of FCDE patients is suggested in order to classify the BOLD signals of brain regions with dysplasia in terms of entropy (MSE) and LRTC (DFA).

The fact that the cluster that covers the brain region with dysplasia correlates with other brain regions, including the contralateral to that cluster, could, also, explain these results. The dynamics of that network may influence the complexity properties of the BOLD signals of all the regions involved.

An issue concerning the suitability of this method is related to shape and amplitude of HRF. Here it is assumed that this function have the same profile across subjects and brain areas. However, the opposite has been already proven (Handwerker et al. 2004) and this assumption may be a confounding effect mainly when dealing with pathologic signals, such as epileptogenic ones. Indeed, different types of epilepsy are usually characterized by different shapes of interictal spikes (Curtis et al. 2012) that would give origin to different shapes, frequencies, and amplitudes of the corresponding BOLD signal changes. Furthermore, some studies demonstrated that interictal events can induce either an enhance or decrease of the corresponding BOLD signal (Cunningham et al. 2012; Pittau et al. 2013) or even would not produce any BOLD response (Leal et al. 2006). Therefore, a rigorous approach namely in the detection of transient spikes related to epileptic activity would take into account these different criteria.

Another limitation regarding the methodology respects the analysis of clusters, found from statistical analysis, which covers brain regions in the midline of the brain. In these cases the comparison between complexity parameters of ipsi and contralateral clusters is not possible, leading to the exclusion of such regions from further analysis.

Moreover it should be remembered that this method deals with the problem of the epileptogenic focus localization which have a different behavior depending on the lesion location, the dynamics of the 'irritative zone' (in the cases of TLE), and the type of the epilepsy. Therefore, it is expected that this type of analysis is not suitable for all epilepsy cases or otherwise it has to be optimized for each epilepsy type or patient.

Regarding future work, there are many issues that could be improved in this methodology. The first one concerns the data pre-processing. Ideally, fMRI data should be corrected for physiologically effects (respiratory and cardiac noises). Then, the effects of pre-processing steps should be investigated: the influence of removing the nuisance covariables (such as head motion, white matter signal, global mean signal, and cerebrospinal fluid signal) and the influence to normalize the data to MNI space or remain in the subject-specific space. Concerning the detection of activity of interest in the BOLD signal, criteria comprising the issues discussed above should be included in order to improve the specificity and sensitivity of selections of voxels. A method that automatically merges the information in the statistical parametric maps, the correlations matrices of ispi and contralateral clusters, the anisotropy analysis, the complexity parameters distributions, and, finally, in the functional connectivity analysis would be defined in order to reduce the analysis time.

CLOSING REMARKS

In this report it was introduced a new approach for the localization of the epileptogenic focus. The present methods to do this assessment are based on techniques that have low spatial resolution, such as sEEG, PET, and SPECT, or techniques with improved spatial resolution but extremely invasive, such as iEEG. An alternative, purposed in this work, is based on BOLD signals analysis, using fMRI, a noninvasive technique with high spatial resolution.

This approach was based on the hypotheses that the epileptogenic focus shows a BOLD temporal profile distinct from the remaining brain parenchyma, either during ictal and interictal activity, and that the epileptogenic focus BOLD signals show lower complexity than healthy parenchyma. Therefore, 2dTCA, a data-driven technique was used to identify brain regions that have similar BOLD profiles. Then a complexity analysis, using MSE analysis and DFA, was taken to identify which of those brain regions correspond to an epileptogenic focus. This methodological combination aimed to provide a definition of a biomarker for epileptogenic tissue identification in order to assist on the diagnostic, monitoring and treatment of epilepsy.

The developed method was tested a study of three patients with epilepsy (with three types of epilepsy: and unilateral and bilateral temporal lobe epilepsies, and focal cortical dysplasia epilepsy). In all of them the epileptogenic focus found by the method match the clinical information or at least belongs to a network that encompasses the lesion that onsets the epileptic activity.

The preliminary results shown in this work open a new perspective on the possible approaches to fMRI data processing concerning epilepsy. Improving this method in order to extended its application to all possible cases of focal, or at least, multifocal epilepsies would be a big step for assisting the diagnostic, monitoring and treatment of epilepsy.

Furthermore, despite this work focused on the epilepsy application, this methodology could also be used to study the BOLD signal dynamics of healthy subjects in order to investigate, for instance resting-state networks, and characterize them in terms of its complexity.

REFERENCES

Andino, S.L.G. et al., 2000. Measuring the complexity of time series: an application to neurophysiological signals. *Human Brain Mapping*, 11(1), pp.46–57. Available at: http://www.ncbi.nlm.nih.gov/pubmed/10997852 [Accessed December 5, 2013].

Avanzini, G. et al., 2013. Do seizures and epileptic activity worsen epilepsy and deteriorate cognitive function? *Epilepsia*, 54 Suppl 8, pp.14–21. Available at: http://www.ncbi.nlm.nih.gov/pubmed/24571112 [Accessed May 26, 2014].

Bagshaw, A.P. et al., 2004. EEG-fMRI of focal epileptic spikes: Analysis with multiple haemodynamic functions and comparison with gadolinium-enhanced MR angiograms. *Human Brain Mapping*, 22(3), pp.179–192. Available at: http://dx.doi.org/10.1002/hbm.20024.

Bernhardt, B.C. et al., 2013. Imaging structural and functional brain networks in temporal lobe epilepsy. *Frontiers in Human Neuroscience*, 7, p.624. Available at: http://www.pubmedcentral.nih.gov/articlerender.fcgi?artid=3787804&tool=pmcentrez&rendertype=abstract [Accessed October 19, 2013].

Catarino, A. et al., 2011. Atypical EEG complexity in autism spectrum conditions: a multiscale entropy analysis. *Clinical Neurophysiology*, 122(12), pp.2375–83. Available at: http://www.clinph-journal.com/article/S1388-2457(11)00314-2/abstract [Accessed November 25, 2013].

Cauda, F. et al., 2010. Functional connectivity of the posteromedial cortex. O. Sporns, ed. *PLoS One*, 5(9), p.11. Available at: http://dx.plos.org/10.1371/journal.pone.0013107 [Accessed August 12, 2014].

Chao-Gan, Y. & Yu-Feng, Z., 2010. DPARSF: A MATLAB Toolbox for "Pipeline" Data Analysis of Resting-State fMRI. *Frontiers in Systems Neuroscience*, 4, p.13. Available at: http://www.pubmedcentral.nih.gov/articlerender.fcgi?artid=2889691&tool=pmcentrez&rendertype=abstract [Accessed October 19, 2013].

Clare, S., 1997. *Functional MRI: Methods and Applications*, Nottingham: University of Nottingham. Available at: http://users.fmrib.ox.ac.uk/~stuart/thesis/fmri.pdf [Accessed November 28, 2013].

Cordes, D. et al., 2002. Hierarchical clustering to measure connectivity in fMRI resting-state data. *Magnetic Resonance Imaging*, 20(4), pp.305–317. Available at: http://www.sciencedirect.com/science/article/pii/S0730725X02005039 [Accessed September 25, 2014].

Costa, M., Goldberger, A. & Peng, C.-K., 2005. Multiscale entropy analysis of biological signals. *Physical Review E*, 71(2), p.021906. Available at: http://link.aps.org/doi/10.1103/PhysRevE.71.021906 [Accessed October 24, 2013].

Costa, M., Goldberger, A. & Peng, C.-K., 2002. Multiscale Entropy Analysis of Complex Physiologic Time Series. *Physical Review Letters*, 89(6), p.068102. Available at: http://link.aps.org/doi/10.1103/PhysRevLett.89.068102 [Accessed October 21, 2013].

Cunningham, C.B.J. et al., 2012. Intracranial EEG-fMRI analysis of focal epileptiform discharges in humans. *Epilepsia*, 53(9), pp.1636–48. Available at: http://www.ncbi.nlm.nih.gov/pubmed/22881457 [Accessed May 29, 2014].

Curtis, M. de, Jefferys, J.G.R. & Avoli, M., 2012. Interictal Epileptiform Discharges in Partial Epilepsy. In *Jasper's Basic Mechanisms of the Epilepsies*. National Center for Biotechnology Information (US). Available at: http://www.ncbi.nlm.nih.gov/books/NBK98179/ [Accessed September 15, 2014].

Eke, A. et al., 2002. Fractal characterization of complexity in temporal physiological signals. *Physiological Measurement*, 23(1), pp.R1–R38. Available at: http://stacks.iop.org/0967-3334/23/i=1/a=201 [Accessed August 30, 2014].

Eke, A. et al., 2012. Pitfalls in Fractal Time Series Analysis: fMRI BOLD as an Exemplary Case. *Frontiers in Physiology*, 3, p.417. Available at: http://www.pubmedcentral.nih.gov/articlerender.fcgi?artid=3513686&tool=pmcentrez&rendertype=abstract [Accessed August 31, 2014].

Escudero, J. et al., 2006. Analysis of electroencephalograms in Alzheimer's disease patients with multiscale entropy. *Physiological Measuremente*, 27(11), pp.1091–106. Available at: http://iopscience.iop.org/0967-3334/27/11/004 [Accessed November 18, 2013].

Federico, P. et al., 2005. Cortical/subcortical BOLD changes associated with epileptic discharges: an EEG-fMRI study at 3 T. *Neurology*, 64(7), pp.1125–30. Available at: http://www.ncbi.nlm.nih.gov/pubmed/15824333 [Accessed September 26, 2014].

Ferreira, H.A. et al., 2013. Complexity analysis of resting-state networks. In *ESMRMB 2013 Congress 30th Annual Scientific Meeting of the European Society for Magnetic Resonance in Medicine and Biology October 3-5, 2013, Toulouse, France*.

Ferreira, H.A., Rocha, A.R., et al., 2012. Multiscale entropy analysis of blood-oxygen level dependent brain signals. In *ESMRMB 2012 Congress 29th Annual Scientific Meeting of the European Society for Magnetic Resonance in Medicine and Biology October 4-6, 2012, Lisboa, Portugal*.

Ferreira, H.A., Fernandes, C.D., et al., 2012. Use of Wavelet Transforms and Detrended Fluctuation Analysis in the evaluation of human skin microcirculation. *Biomedical and Biopharmaceutical Research*, (9), pp.79–86.

Fisher, R.S. et al., 2005. Epileptic Seizures and Epilepsy: Definitions Proposed by the International League Against Epilepsy (ILAE) and the International Bureau for Epilepsy (IBE). *Epilepsia*, 46(10), pp.1698–9; author reply 1701–2. Available at: http://www.ncbi.nlm.nih.gov/pubmed/16190948.

Foley, E. et al., 2014. Magnetoencephalography in the study of epilepsy and consciousness. *Epilepsy & Behavior*, 30, pp.38–42. Available at:

http://www.sciencedirect.com/science/article/pii/S1525505013004666 [Accessed September 27, 2014].

Fox, M.D. et al., 2005. The human brain is intrinsically organized into dynamic, anticorrelated functional networks. *Proceedings of the National Academy of Sciences of the United States of America*, 102(27), pp.9673–8. Available at: http://www.pubmedcentral.nih.gov/articlerender.fcgi?artid=1157105&tool=pmcentrez&rendertype=abstract.

Friston, K. et al., 1995. Statistical parametric maps in functional imaging: a general linear approach. *Human Brain Mapping*, 2, pp.189–210. Available at: http://onlinelibrary.wiley.com/doi/10.1002/hbm.460020402/full [Accessed August 28, 2014].

Gao, J.-H. & Yee, S.-H., 2003. Iterative temporal clustering analysis for the detection of multiple response peaks in fMRI. *Magnetic Resonance Imaging*, 21(1), pp.51–3. Available at: http://www.ncbi.nlm.nih.gov/pubmed/12620546.

Glover, G.H., 1999. Deconvolution of impulse response in event-related BOLD fMRI. *NeuroImage*, 9(4), pp.416–29. Available at: http://www.ncbi.nlm.nih.gov/pubmed/10191170.

Goldberger, A.L. et al., 2000. PhysioBank, PhysioToolkit, and PhysioNet : Components of a New Research Resource for Complex Physiologic Signals. *Circulation*, 101(23), pp.e215–e220. Available at: http://circ.ahajournals.org/content/101/23/e215.abstract [Accessed July 10, 2014].

Goldberger, A.L., Peng, C.-K. & Lipsitz, L. a, 2002. What is physiologic complexity and how does it change with aging and disease? *Neurobiology of Aging*, 23(1), pp.23–6. Available at: http://www.ncbi.nlm.nih.gov/pubmed/11755014.

Hamandi, K. et al., 2005. fMRI temporal clustering analysis in patients with frequent interictal epileptiform discharges: comparison with EEG-driven analysis. *NeuroImage*, 26(1), pp.309–16. Available at: http://www.ncbi.nlm.nih.gov/pubmed/15862232 [Accessed September 14, 2013].

Handwerker, D.A., Ollinger, J.M. & D'Esposito, M., 2004. Variation of BOLD hemodynamic responses across subjects and brain regions and their effects on statistical analyses. *NeuroImage*, 21(4), pp.1639–51. Available at: http://www.ncbi.nlm.nih.gov/pubmed/15050587 [Accessed August 17, 2014].

Hassanpour, H., Mesbah, M. & Boashash, B., 2004. EEG spike detection using time-frequency signal analysis. *Acoustics, Speech, and Signal Processing*, 5, pp.V–421 – V–424. Available at: http://ieeexplore.ieee.org/xpls/abs_all.jsp?arnumber=1327137 [Accessed November 27, 2013].

Holmes, G., Sirven, J. & Fisher, R.S., 2013. Temporal Lobe Epilepsy. *Epilepsy Foundation*. Available at: http://www.epilepsy.com/learn/types-epilepsy-syndromes/temporal-lobe-epilepsy [Accessed September 14, 2014].

Holmes, M. et al., 2012. Resting state functional connectivity of the hippocampus associated with neurocognitive function in left temporal lobe epilepsy. *Human Brain Mapping*, 000(January).

Available at: http://www.ncbi.nlm.nih.gov/pubmed/23124719 [Accessed September 23, 2013].

Hu, K. et al., 2001. Effect of trends on detrended fluctuation analysis. *Physical Review E*, 64(1), p.011114. Available at: http://link.aps.org/doi/10.1103/PhysRevE.64.011114 [Accessed September 3, 2014].

Hutchison, R.M. et al., 2013. Dynamic functional connectivity: promise, issues, and interpretations. *NeuroImage*, 80, pp.360–78. Available at: http://www.ncbi.nlm.nih.gov/pubmed/23707587 [Accessed September 16, 2013].

Jezzard, P., 1999. Functional Mapping Methods. *FMRIB.* Available at: http://www.fmrib.ox.ac.uk [Accessed November 28, 2013].

Jezzard, P., Matthews, P.M. & Smith, S.M., 2001. *Functional MRI: an introduction to methods*, Oxford University Press.

Josephs, O., Turner, R. & Friston, K., 1997. Event-Related fMRI. *Human Brain Mapping*, 248, pp.243–248.

Kabat, J. & Król, P., 2012. Focal cortical dysplasia - review. *Polish Journal of Radiology*, 77(2), pp.35–43. Available at: http://www.pubmedcentral.nih.gov/articlerender.fcgi?artid=3403799&tool=pmcentrez&rendertype=abstract.

Keogh, B.P. et al., 2005. BOLD-fMRI of PTZ-induced seizures in rats. *Epilepsy Research*, 66(1-3), pp.75–90. Available at: http://www.sciencedirect.com/science/article/pii/S0920121105001348 [Accessed September 25, 2014].

Khatamian, Y.B., Fahoum, F. & Gotman, J., 2011. Limits of 2D-TCA in detecting BOLD responses to epileptic activity. *Epilepsy research*, 94(3), pp.177–188. Available at: http://www.ncbi.nlm.nih.gov/pubmed/21353479 [Accessed December 6, 2013].

Kim, S. & Mountz, J.M., 2011. SPECT Imaging of Epilepsy: An Overview and Comparison with F-18 FDG PET. *International Journal of Molecular Imaging*, 2011, p.9.

Ko, D.Y. et al., 2014. Epileptiform Discharges. *Medscape*. Available at: http://emedicine.medscape.com/article/1138880-overview [Accessed September 27, 2014].

Kobayashi, E. et al., 2005. Intrinsic epileptogenicity in polymicrogyric cortex suggested by EEG-fMRI BOLD responses. *Neurology*, 64(7), pp.1263–6. Available at: http://www.ncbi.nlm.nih.gov/pubmed/15824359 [Accessed September 26, 2014].

Kurths, J., Schwarz, U. & Witt, A., 1996. Measures of complexity in signal analysis. In *July 10 - 13, 1995, 3rd Technical Conference on Nonlinear Dynamics (Chaos) and Full Spectrum*. pp. 1–19. Available at: http://link.aip.org/link/?APCPCS/375/33/1 [Accessed October 23, 2013].

Leal, A. et al., 2007. Analysis of the generators of epileptic activity in early-onset childhood benign occipital lobe epilepsy. *Clinical Neurophysiology*, 118(6), pp.1341–7. Available at:

http://www.sciencedirect.com/science/article/pii/S138824570700051X [Accessed November 27, 2013].

Leal, A. et al., 2008. Origin of frontal lobe spikes in the early onset benign occipital lobe epilepsy (Panayiotopoulos syndrome). *Clinical Neurophysiology*, 119(9), pp.1985–91. Available at: http://www.sciencedirect.com/science/article/pii/S1388245708005336 [Accessed November 27, 2013].

Leal, A. et al., 2006. The BOLD effect of interictal spike activity in childhood occipital lobe epilepsy. *Epilepsia*, 47(9), pp.1536–42. Available at: http://www.ncbi.nlm.nih.gov/pubmed/16981870 [Accessed October 25, 2013].

Leite, M., Leal, A. & Figueiredo, P., 2013. Transfer Function between EEG and BOLD Signals of Epileptic Activity. *Frontiers in Neurology*, 4, p.1. Available at: http://www.pubmedcentral.nih.gov/articlerender.fcgi?artid=3554836&tool=pmcentrez&rendertype=abstract [Accessed October 18, 2013].

Little, M.A. et al., 2007. Exploiting nonlinear recurrence and fractal scaling properties for voice disorder detection. *BioMedical Engineering OnLine*, 6(1), p.23. Available at: http://www.biomedical-engineering-online.com/content/6/1/23 [Accessed August 18, 2014].

Liu, Y. et al., 2000. The temporal response of the brain after eating revealed by functional MRI. *Nature*, 405(6790), pp.1058–62. Available at: http://www.ncbi.nlm.nih.gov/pubmed/10890447.

Lopes, R. et al., 2012. Detection of epileptic activity in fMRI without recording the EEG. *NeuroImage*, 60(3), pp.1867–79. Available at: http://www.pubmedcentral.nih.gov/articlerender.fcgi?artid=3753286&tool=pmcentrez&rendertype=abstract [Accessed November 11, 2013].

Lowe, M.J., Mock, B.J. & Sorenson, J.A., 1998. Functional Connectivity in Single and Multislice Echoplanar Imaging Using Resting-State Fluctuations. *NeuroImage*, 7(2), pp.119–132. Available at: http://www.sciencedirect.com/science/article/pii/S1053811997903153 [Accessed December 5, 2013].

De Martino, F. et al., 2007. Classification of fMRI independent components using IC-fingerprints and support vector machine classifiers. *NeuroImage*, 34(1), pp.177–94. Available at: http://www.sciencedirect.com/science/article/pii/S1053811906009244 [Accessed September 25, 2014].

McIntosh, A.R. et al., 2013. Spatiotemporal Dependency of Age-Related Changes in Brain Signal Variability. *Cerebral Cortex*, p.bht030–. Available at: http://cercor.oxfordjournals.org/content/early/2013/02/07/cercor.bht030.long [Accessed November 25, 2013].

Mizuno, T. et al., 2010. Assessment of EEG dynamical complexity in Alzheimer's disease using multiscale entropy. *Clinical Neurophysiology*, 121(9), pp.1438–46. Available at: http://www.clinph-journal.com/article/S1388-2457(10)00313-5/abstract [Accessed December 5, 2013].

Monto, S. et al., 2007. Epileptogenic neocortical networks are revealed by abnormal temporal dynamics in seizure-free subdural EEG. *Cerebral Cortex*, 17(6), pp.1386–93. Available at: http://www.ncbi.nlm.nih.gov/pubmed/16908492 [Accessed November 11, 2013].

Morgan, V.L. et al., 2008. Development of 2dTCA for the detection of irregular, transient BOLD activity. *Human Brain Mapping*, 29(1), pp.57–69. Available at: http://www.pubmedcentral.nih.gov/articlerender.fcgi?artid=2719759&tool=pmcentrez&rendertype=abstract [Accessed September 14, 2013].

Morgan, V.L. et al., 2012. Lateralization of temporal lobe epilepsy using resting functional magnetic resonance imaging connectivity of hippocampal networks. *Epilepsia*, 53(9), pp.1628–35. Available at: http://www.pubmedcentral.nih.gov/articlerender.fcgi?artid=3436984&tool=pmcentrez&rendertype=abstract [Accessed October 16, 2013].

Morgan, V.L. et al., 2004. Resting functional MRI with temporal clustering analysis for localization of epileptic activity without EEG. *NeuroImage*, 21(1), pp.473–481. Available at: http://linkinghub.elsevier.com/retrieve/pii/S105381190300541X [Accessed September 14, 2013].

Morgan, V.L. & Gore, J.C., 2009. Detection of irregular, transient fMRI activity in normal controls using 2dTCA: comparison to event-related analysis using known timing. *Human Brain Mapping*, 30(10), pp.3393–405. Available at: http://www.pubmedcentral.nih.gov/articlerender.fcgi?artid=2748174&tool=pmcentrez&rendertype=abstract [Accessed September 14, 2013].

Morgan, V.L., Gore, J.C. & Abou-Khalil, B., 2007. Cluster analysis detection of functional MRI activity in temporal lobe epilepsy. *Epilepsy Research*, 76(1), pp.22–33. Available at: http://www.pubmedcentral.nih.gov/articlerender.fcgi?artid=2003336&tool=pmcentrez&rendertype=abstract [Accessed September 14, 2013].

Morgan, V.L., Gore, J.C. & Abou-Khalil, B., 2010. Functional epileptic network in left mesial temporal lobe epilepsy detected using resting fMRI. *Epilepsy Research*, 88(2-3), pp.168–178. Available at: http://linkinghub.elsevier.com/retrieve/pii/S0920121109003246 [Accessed November 9, 2013].

Morgan, V.L., Gore, J.C. & Szaflarski, J.P., 2008. Temporal clustering analysis: What does it tell us about the resting state of the brain? *Medical Science Monitor*, 14(7), pp.CR345–CR352. Available at: http://www.ncbi.nlm.nih.gov/pmc/articles/PMC2553434/ [Accessed September 18, 2013].

Mountz, J., 2007. PET/CT neuroimaging applications for epilepsy and cerebral neoplasm. *Applied Radiology*, pp.44–52. Available at: http://www.appliedradiology.mobi/uploadedfiles/Issues/2007/11/Articles/AR_11-07_Mountz2.pdf [Accessed November 27, 2013].

Ouyang, G., Dang, C. & Li, X., 2009. Multiscale entropy analysis of EEG signals in epileptic rats. *Biomedical Engineering: Applications, Basis and Communications*, 21(03), pp.149–155. Available at: http://www.worldscientific.com/doi/abs/10.4015/S1016237209001209 [Accessed March 10, 2014].

Parish, L.M. et al., 2004. Long-range temporal correlations in epileptogenic and non-epileptogenic human hippocampus. *Neuroscience*, 125(4), pp.1069–76. Available at: http://www.ncbi.nlm.nih.gov/pubmed/15120866 [Accessed October 24, 2013].

Peng, C. et al., 1994. Mosaic Organization of DNA molecules. *Physical Review E*, 49(2), pp.1685–1689.

Peng, C. et al., 1995. Quantification of scaling exponents and crossover phenomena in nonstationary heartbeat time series. *Americam Institute of Physics: CHAOS*. Available at: http://link.aip.org/link/?cha/5/82/1 [Accessed December 6, 2013].

Pincus, S., 1991. Approximate entropy as a measure of system complexity. *Proceedings of the National Academy of Science*. Available at: http://www.pnas.org/content/88/6/2297.full.pdf [Accessed December 5, 2013].

Pittau, F. et al., 2013. Negative BOLD response to interictal epileptic discharges in focal epilepsy. *Brain Topography*, 26(4), pp.627–40. Available at: http://www.ncbi.nlm.nih.gov/pubmed/23793553 [Accessed June 24, 2014].

Pizarro, R. et al., 2012. TCA and functional connectivity analysis using resting fMRI in epilepsy patients. *F1000Posters*, 3(959). Available at: http://f1000.com/posters/browse/summary/1090797 [Accessed December 5, 2013].

Press, W.H. et al., 1988. Numerical recipes in C: the art of scientific computing. Available at: http://apps.nrbook.com/c/index.html. [Accessed September 11, 2014].

Protzner, B. et al., 2010. Hippocampal signal complexity in mesial temporal lobe epilepsy: a noisy brain is a healthy brain. *Archives Italiennes de Biologie*, 148(3), pp.289–97. Available at: http://www.ncbi.nlm.nih.gov/pubmed/21175015.

Richman, J.S. & Moorman, J.R., 2000. Physiological time-series analysis using approximate entropy and sample entropy. *American Journal of Physiology - Heart and Circulatory Physiology*, 278(6), pp.H2039–2049. Available at: http://ajpheart.physiology.org/content/278/6/H2039 [Accessed December 5, 2013].

Rodionov, R. et al., 2007. Independent component analysis of interictal fMRI in focal epilepsy: comparison with general linear model-based EEG-correlated fMRI. *NeuroImage*, 38(3), pp.488–500. Available at: http://www.ncbi.nlm.nih.gov/pubmed/17889566.

Salek-Haddadi, A. et al., 2006. Hemodynamic correlates of epileptiform discharges: an EEG-fMRI study of 63 patients with focal epilepsy. *Brain Research*, 1088(1), pp.148–66. Available at: http://www.ncbi.nlm.nih.gov/pubmed/16678803 [Accessed September 23, 2014].

Shirer, W.R. et al., 2012. Decoding subject-driven cognitive states with whole-brain connectivity patterns. *Cerebral Cortex*, 22(1), pp.158–65. Available at: http://www.pubmedcentral.nih.gov/articlerender.fcgi?artid=3236795&tool=pmcentrez&rendertype=abstract [Accessed March 19, 2014].

Smith, S.M., 2004. Overview of fMRI analysis. *British Journal of Radiology*, 77(suppl_2), pp.S167–S175. Available at: http://bjr.birjournals.org/cgi/doi/10.1259/bjr/33553595 [Accessed September 16, 2013].

Somorjai, R.L. & Jarmasz, M., 2003. Exploratory analysis of fMRI data by fuzzy clustering: philosophy, strategy, tactics, implementation. In *Exploratory analysis and data modeling in functional neuroimaging*. Cambridge, MA, USA: MIT Press, pp. 17–48. Available at: http://dl.acm.org/citation.cfm?id=949823.949828 [Accessed November 29, 2013].

Song, X.-W. et al., 2011. REST: a toolkit for resting-state functional magnetic resonance imaging data processing. B. J. Harrison, ed. *PLoS One*, 6(9), p.e25031. Available at: http://dx.plos.org/10.1371/journal.pone.0025031 [Accessed July 10, 2014].

Sugiura, M. et al., 2004. Different roles of the frontal and parietal regions in memory-guided saccade: A PCA approach on time course of BOLD signal changes. *Human Brain Mapping*, 23(3), pp.129–139. Available at: http://dx.doi.org/10.1002/hbm.20049.

Takahashi, T. et al., 2009. Age-related variation in EEG complexity to photic stimulation: a multiscale entropy analysis. *Clinical Neurophysiology*, 120(3), pp.476–83. Available at: http://www.clinph-journal.com/article/S1388-2457(09)00009-1/abstract [Accessed November 30, 2013].

Takahashi, T. et al., 2010. Antipsychotics reverse abnormal EEG complexity in drug-naive schizophrenia: A multiscale entropy analysis. *NeuroImage*, 51(1), pp.173–182. Available at: http://www.sciencedirect.com/science/article/pii/S1053811910001576 [Accessed December 5, 2013].

Thornton, R.C. et al., 2010. Imaging haemodynamic changes related to seizures: comparison of EEG-based general linear model, independent component analysis of fMRI and intracranial EEG. *NeuroImage*, 53(1), pp.196–205. Available at: http://www.ncbi.nlm.nih.gov/pubmed/20570736 [Accessed August 9, 2013].

Tzourio-Mazoyer, N. et al., 2002. Automated anatomical labeling of activations in SPM using a macroscopic anatomical parcellation of the MNI MRI single-subject brain. *NeuroImage*, 15(1), pp.273–89. Available at: http://www.ncbi.nlm.nih.gov/pubmed/11771995 [Accessed July 10, 2014].

Wahlberg, P. & Lantz, G., 2000. Methods for robust clustering of epileptic EEG spikes. *Biomedical Engineering, IEEE*, 47(7). Available at: http://biomagnet.uni-muenster.de/PDF_library/000342.pdf [Accessed November 29, 2013].

Wang, Z. et al., 2012. Spontaneous EEG-Functional MRI in Mesial Temporal Lobe Epilepsy: Implications for the Neural Correlates of Consciousness. *Epilepsy Research and Treatment*, 2012, p.385626. Available at: http://www.pubmedcentral.nih.gov/articlerender.fcgi?artid=3420502&tool=pmcentrez&rendertype=abstract [Accessed September 18, 2013].

Ward, L. & Greenwood, P., 2007. 1/f noise. *Scholarpedia*, 2(12), p.1537. Available at: http://www.scholarpedia.org/article/1/f_noise [Accessed August 22, 2014].

WHO, 2012. World Health Organization. Available at: www.who.int [Accessed September 27, 2014].

Yang, A.C., Wang, S.-J., et al., 2013. Cognitive and neuropsychiatric correlates of EEG dynamic complexity in patients with Alzheimer's disease. *Progress in Neuro-Psychopharmacology and Biological Psychiatry*, 47C, pp.52–61.

Yang, A.C., Huang, C.-C., et al., 2013. Complexity of spontaneous BOLD activity in default mode network is correlated with cognitive function in normal male elderly: a multiscale entropy analysis. *Neurobiology of Aging*, 34(2), pp.428–38. Available at: http://www.ncbi.nlm.nih.gov/pubmed/22683008 [Accessed December 5, 2013].

Yang, X. et al., 2012. A comparison of distributional considerations with statistical analysis of resting state fMRI at 3T and 7T. In *Proc. SPIE*. pp. 1–10. Available at: http://proceedings.spiedigitallibrary.org/proceeding.aspx?articleid=1285127 [Accessed October 16, 2013].

Yee, S.-H. & Gao, J.-H., 2002. Improved detection of time windows of brain responses in fMRI using modified temporal clustering analysis. *Magnetic Resonance Imaging*, 20(1), pp.17–26. Available at: http://www.ncbi.nlm.nih.gov/pubmed/11973026.

You, X. et al., 2011. Sub-patterns of language network reorganization in pediatric localization related epilepsy: A multisite study. *Human Brain Mapping*, 32(5), pp.784–799. Available at: http://dx.doi.org/10.1002/hbm.21066.

Zhang, Y., 1991. Complexity and 1/f noise. A phase space approach. *Journal de Physique I*, 20(8), pp.533–537. Available at: http://jp1.journaldephysique.org/articles/jp1/abs/1991/07/jp1v1p971/jp1v1p971.html [Accessed December 5, 2013].

APPENDIX A

The information summarized in this section can be found with more details in (Friston et al. 1995; Smith 2004).

Statistical Analysis of fMRI data: General Linear Model

In the GLM approach the data is treated as a linear combination of model functions (predictors or regressors) plus noise (error). These model functions are assumed to have known shapes, but unknown amplitudes which need to be estimated. In order to estimate that amplitude, i.e. the coefficients of the general linear model, a voxel-wise analysis is performed through Eq. 10.

$$\begin{bmatrix} Y_1 \\ Y_2 \\ \vdots \\ Y_N \end{bmatrix} = \begin{bmatrix} 1 & X_{11} & \cdots & X_{1p} \\ 1 & X_{21} & \cdots & X_{2p} \\ \vdots & \vdots & \ddots & \vdots \\ 1 & X_{N1} & \cdots & X_{Np} \end{bmatrix} \times \begin{bmatrix} \beta_0 \\ \beta_1 \\ \vdots \\ \beta_p \end{bmatrix} + \begin{bmatrix} \epsilon_0 \\ \epsilon_1 \\ \vdots \\ \epsilon_N \end{bmatrix} \Leftrightarrow \boldsymbol{Y_{N\times 1} = X_{N\times p}\beta_{p\times 1} + \epsilon_{N\times 1}} \quad \textbf{Eq. 10}$$

Where *Y* represents the voxel's time series with a length of *N* time points; *X* is the matrix design in which there are *p* model functions or regressors with *N* time points in length and that reflect the stimuli profiles for statistical testing; the β matrix represent each regressor's amplitude present in that voxel; finally, ε represents the error in the model fitting.

Inference on fMRI data: Statistical Parametric Maps

From the analysis described above an estimation for each β parameter, $\hat{\beta}$, is obtained and in order to make inference about the significance of the results this $\hat{\beta}$ is converted into a useful statistic , namely a t-value through Eq. 11, where σ stands for standard deviation.

$$\boldsymbol{t = \frac{\hat{\beta}}{\sigma(\hat{\beta})}} \quad \textbf{Eq. 11}$$

With this statistic it's possible to measure how significantly different is the estimated parameter from zero. Therefore, a binary contrast vector *c* can be used to infer which brain regions best fit a particular model function or regressor. For example, in a case with 3 regressors, to make inference about the first one the contrast vector must be *c*=[1 0 0], for the second one *c*=[0 1 0], and for the third one *c*=[0 0 1]. Thus, Eq. 11 can be written as Eq. 12.

$$\boldsymbol{t = \frac{c^T\hat{\beta}}{\sigma(c^T\hat{\beta})}} \quad \textbf{Eq. 12}$$

This t-value information can then be transformed into *p*-values using a table of *t* statistic and two additional parameters: the degrees of freedom of the map and the *p*-value of thresholding.

Hence, as a final result a statistical parametric map (SPM) of all brain volume voxels is constructed with t-values information.

Presentation of Statistical Parametric Maps: Thresholding

Thresholding the SPMs is the final step before the results presentation and this can be performed through several ways. The basic one simply defines a fixed value for the threshold, for example a p-value of 0.01 or a significant level of 1%. However, with this approach a problem of multiple comparisons are implicit, i.e., for the example above, considering a 1% of significance there are a chance that in 100 000 voxels, 1000 will activate even if not associated with the stimulus. This phenomena is named Type I error (false positive).

To overcome this shortcoming the p-value can be corrected by the Family-Wise Error Rate (FWER), which is the probability of making one or more Type I errors. The most used method in the FWER is the Bonferroni correction. This method defines the *p*-value threshold as a division between the significant level required and the total number of comparisons made for that given statistical test. In this way, the level of significance considered for the thresholding is considerably more restricted.

Additionally, k-extended threshold can be used in order to limit the minimum extend of a given cluster. This means that a brain region is considered to be activated if the extend of that activations covers k or more voxels. This prevents a unique and isolated voxel to be considered activated.

APPENDIX B

The healthy subject scan used to create the simulated dataset on **Chapter 2: 2.2.1 Simulated Dataset Characterization** is part of a real data study of 2013, acquired at the University of Graz, Austria, which is a result from an experimental paradigm designed to study rest and movement associated brain connectivity. For the purpose of this study only the rest fMRI acquisitions were used. Images were acquired with a 3T Siemens Magneton Skyra syngo MR D13 Scanner. A T2*-weighted single-shot spin echo sequence with echo planar images readout (SS-SE-EPI) was used to acquire BOLD-EPI images over a 5 min run with the following parameters: TR=1.83 s, TE=30 ms, matrix=68 x 68, FOV=240, voxel size = 3.5 x 3.5 x 3.5 mm^3, and 32 interleaved slices.

Pre-processing of the healthy subject scan was performed using DPARSF toolbox (Chao-Gan & Yu-Feng 2010). It consisted of removing the first 10 time points for signal stabilization (steady-state), slice timing to correct for interleaved acquisition, realignment for correction of motion effects, normalization to the MNI space using the EPI template provided by DPARSF, and spatial smoothing using a Guassian 4 mm FWHM kernel. Data was, then, detrended and filtered with a bandpass filter at 0.01~0.08 Hz in order to remove frequencies not expected in BOLD response.

APPENDIX C

Complementary results from patients presented in **Chapter 5: Epileptic Patients Study**.

Pictures for normalization pre-processing step and movement correction plot checking

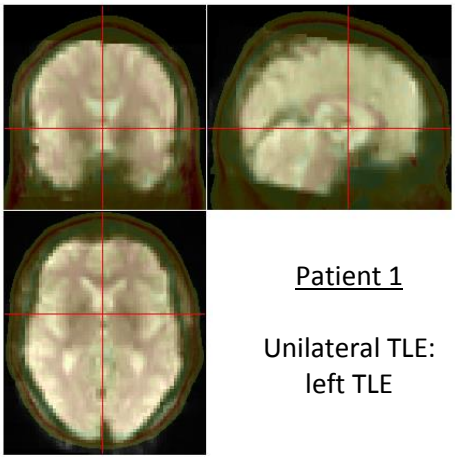

Patient 1

Unilateral TLE:
left TLE

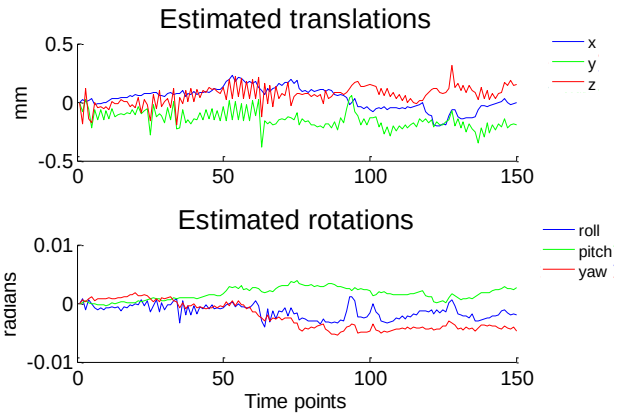

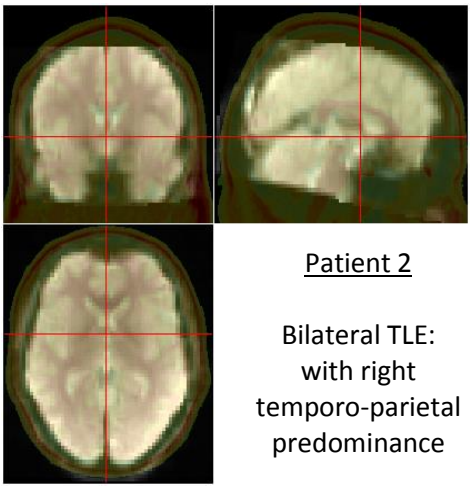

Patient 2

Bilateral TLE:
with right
temporo-parietal
predominance

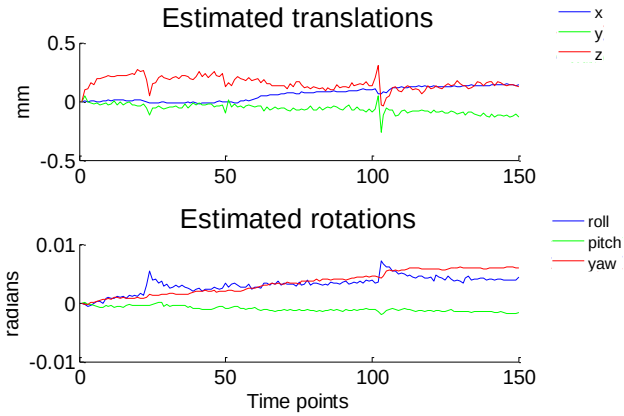

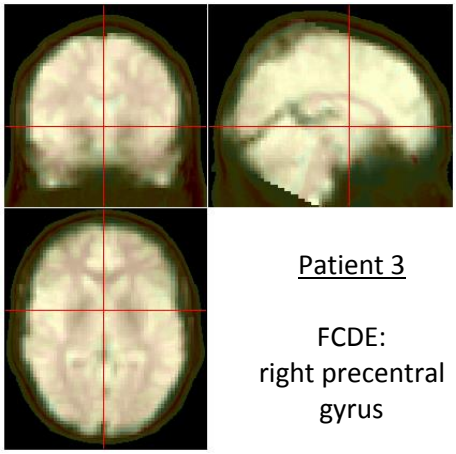

Patient 3

FCDE:
right precentral
gyrus

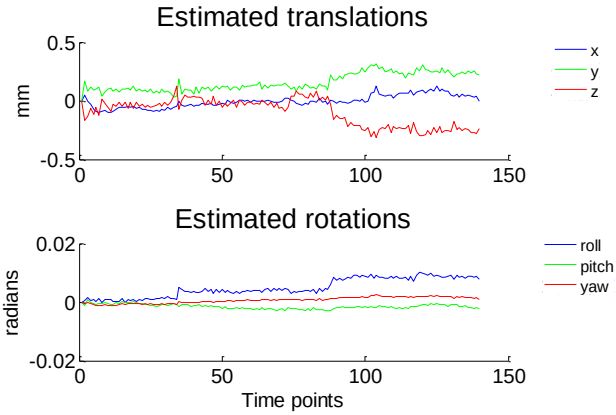

Patient 1 – Unilateral TLE: left TLE

RTCs temporal profile obtained with the 2dTCA.

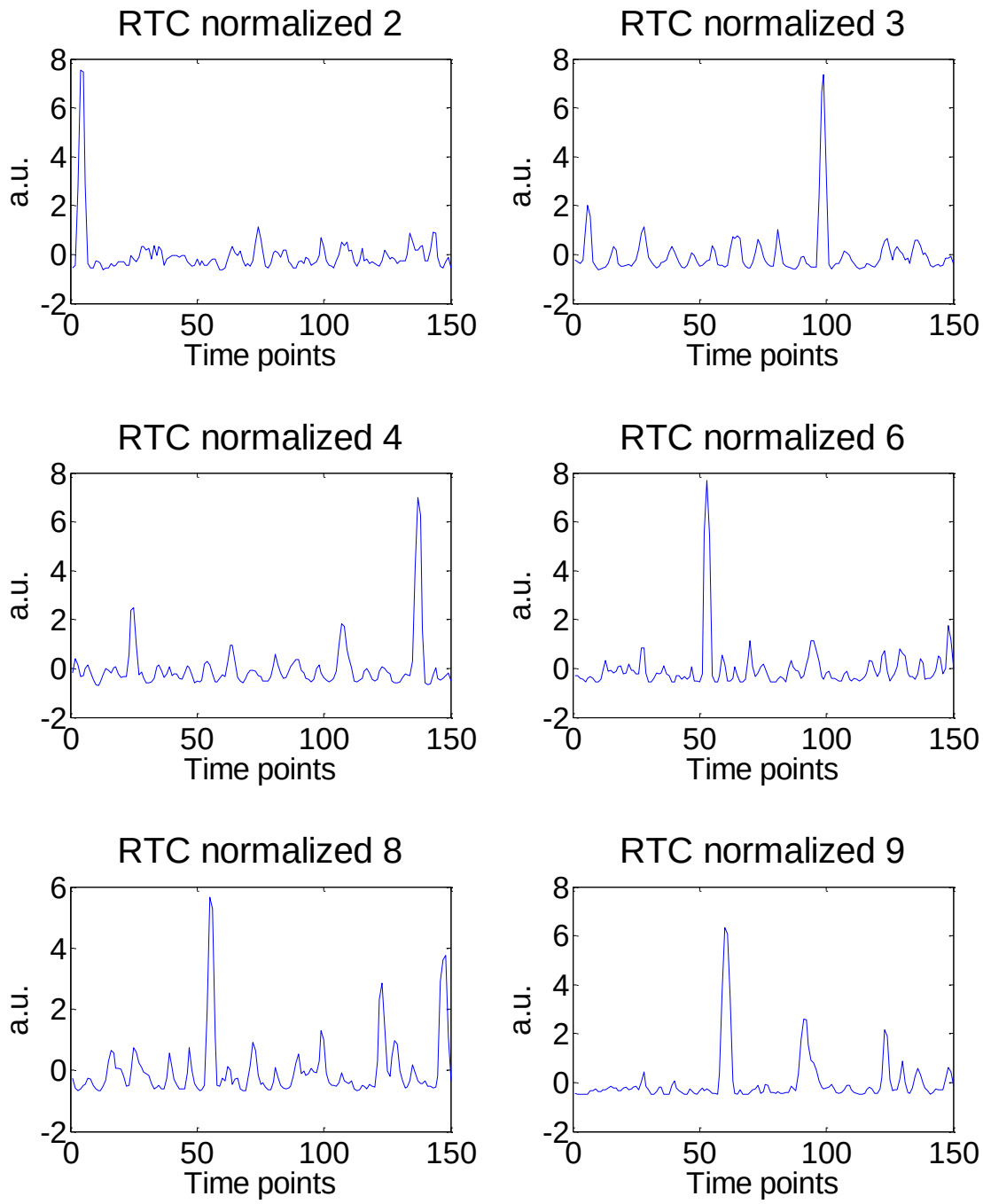

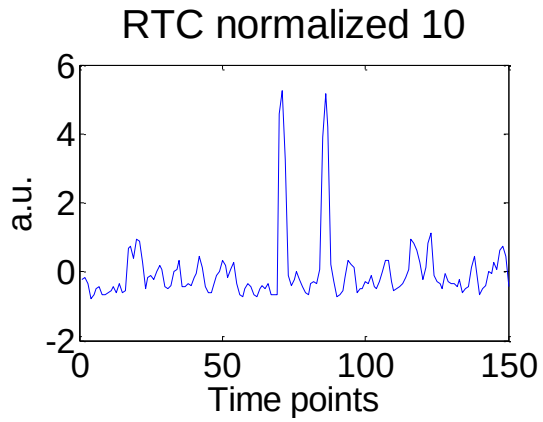
RTC normalized 10
a.u.
Time points
6
4
2
0
-2
0
50
100
150

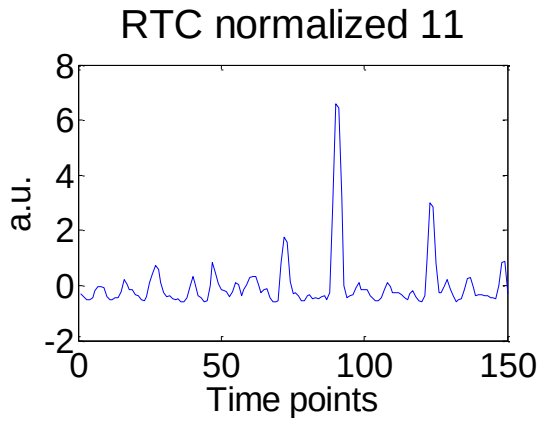
RTC normalized 11
a.u.
Time points
8
6
4
2
0
-2
0
50
100
150

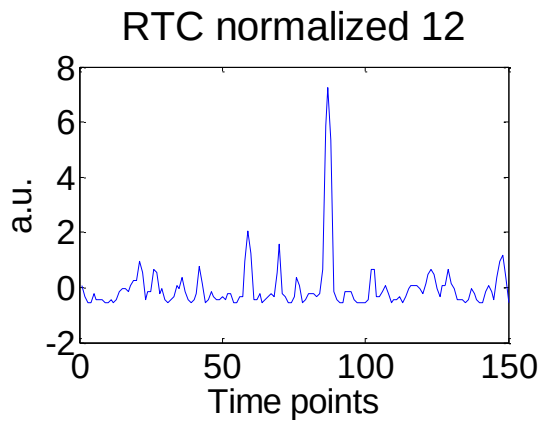
RTC normalized 12
a.u.
Time points
8
6
4
2
0
-2
0
50
100
150

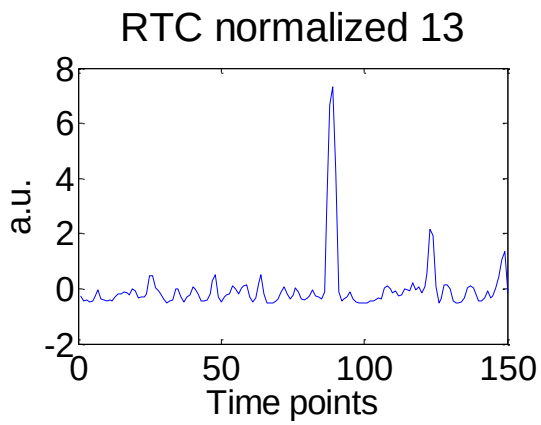
RTC normalized 13
a.u.
Time points
8
6
4
2
0
-2
0
50
100
150

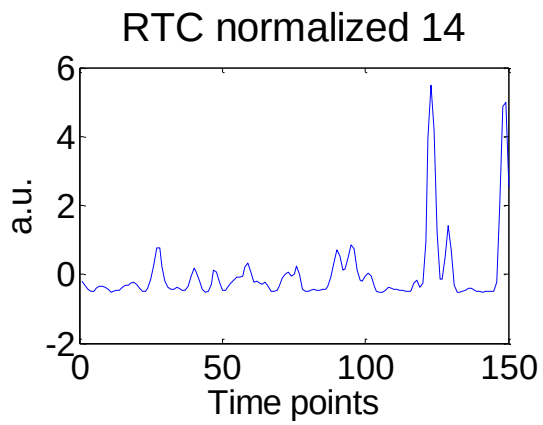
RTC normalized 14
a.u.
Time points
6
4
2
0
-2
0
50
100
150

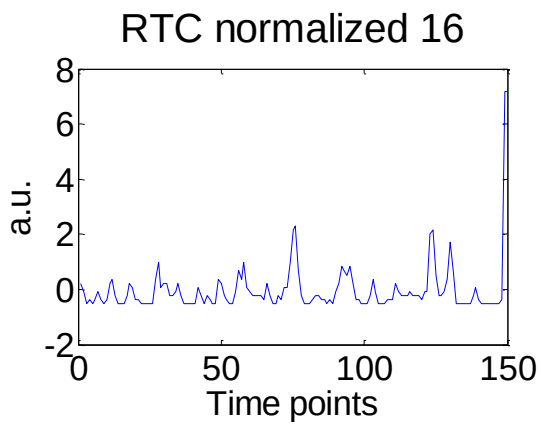
RTC normalized 16
a.u.
Time points
8
6
4
2
0
-2
0
50
100
150

Spatial location of each RTC's clusters and corresponding temporal profiles

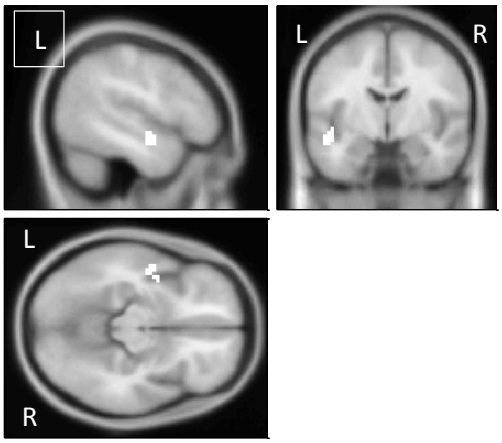

RTC5_30

# voxels	structure
30	--TOTAL # VOXELS--
30	Left Cerebrum
30	Temporal Lobe
22	White Matter
19	Temporal_Sup_L (aal)
17	Sub-Gyral
11	Temporal_Mid_L (aal)
8	Gray Matter
8	Middle Temporal Gyrus
5	brodmann area 21
5	Superior Temporal Gyrus
3	brodmann area 22

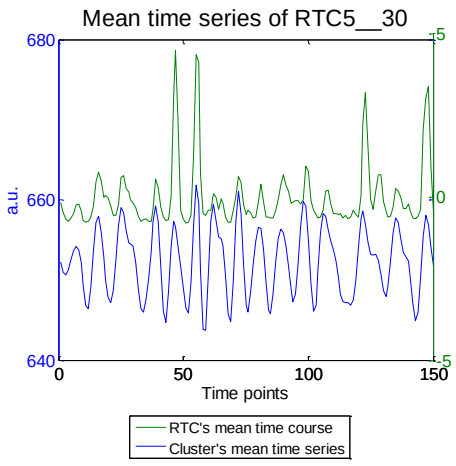

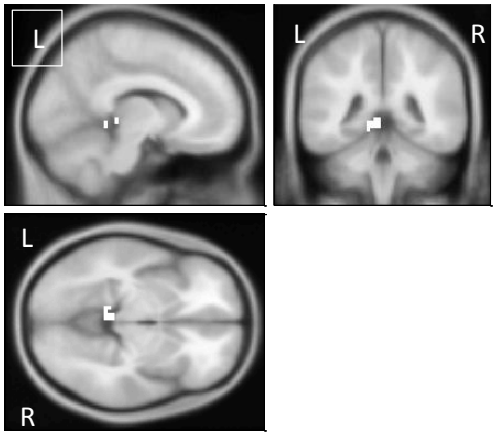

RTC5_30b

# voxels	structure
30	--TOTAL # VOXELS--
18	Cerebelum_4_5_L (aal)
13	Culmen
13	Left Cerebellum
13	Cerebellum Anterior Lobe
8	Lingual_L (aal)
5	Left Cerebrum
4	Limbic Lobe
3	Left Brainstem
3	Gray Matter
3	Midbrain
3	Inter-Hemispheric
2	Posterior Cingulate
2	brodmann area 30
2	Parahippocampa Gyrus
1	Vermis_4_5 (aal)
1	White Matter
1	brodmann area 29
1	Extra-Nuclear
1	Sub-lobar

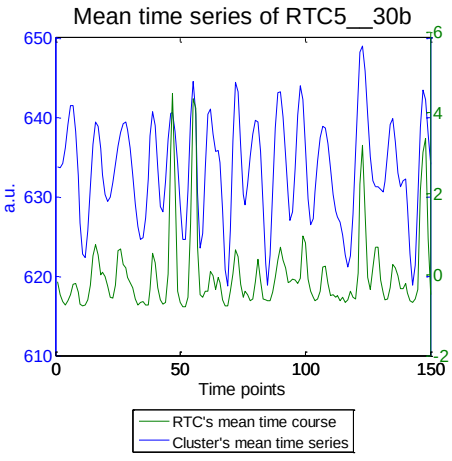

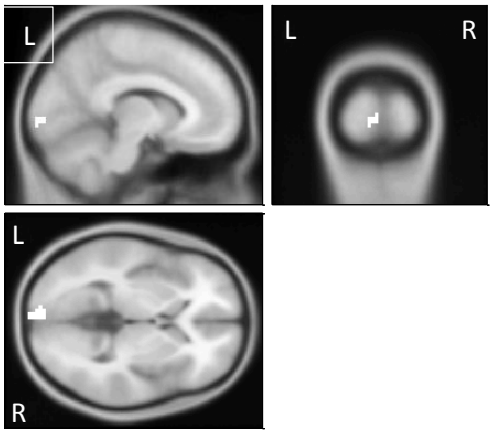

RTC5_31

# voxels	structure
31	--TOTAL # VOXELS--
28	Left Cerebrum
28	Occipital Lobe
24	Calcarine_L (aal)
21	Cuneus
21	Gray Matter
15	brodmann area 17
7	Lingual Gyrus
7	White Matter
6	brodmann area 18
5	Occipital_Mid_L (aal)
1	Inter-Hemispheric
1	Occipital_Sup_L (aal)
1	Cuneus_L (aal)

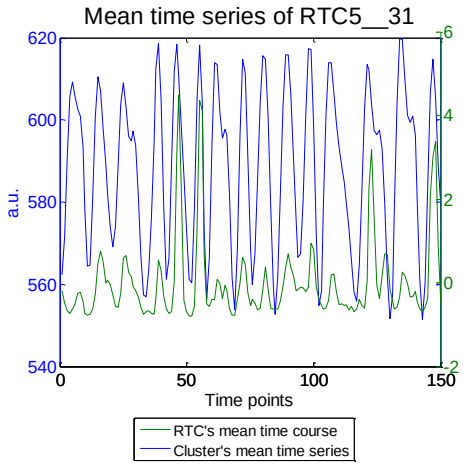

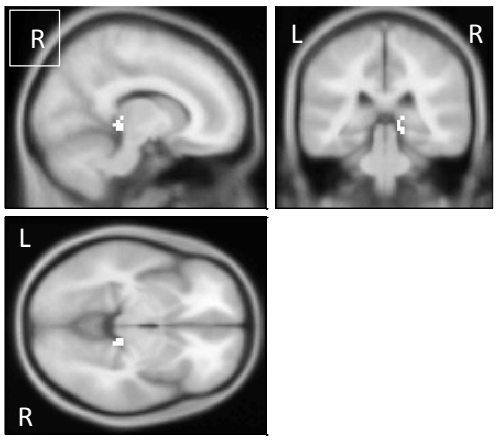

RTC5_36

# voxels	structure
36	--TOTAL # VOXELS--
25	Right Cerebrum
21	Limbic Lobe
19	Parahippocampa Gyrus
16	ParaHippocampal_R (aal)
12	Gray Matter
8	White Matter
8	Lingual_R (aal)
5	brodmann area 35
4	Sub-lobar
4	Thalamus
4	Thalamus_R (aal)
3	Pulvinar
3	Right Brainstem
3	Midbrain
2	brodmann area 30
1	Fusiform_R (aal)
1	Cerebellum Anterior Lobe
1	Culmen
1	brodmann area 36
1	Right Cerebellum

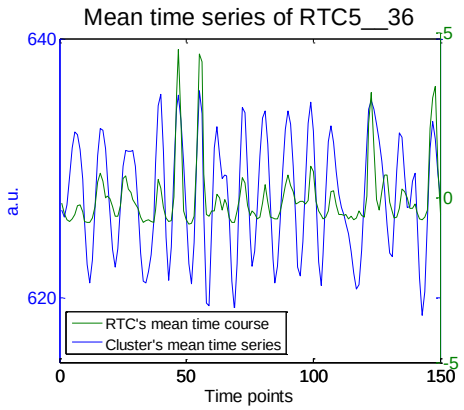

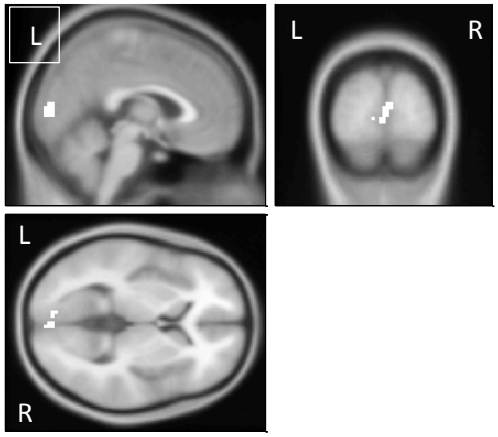

RTC7_38

# voxels	structure
38	--TOTAL # VOXELS--
32	Occipital Lobe
31	Calcarine_L (aal)
24	Cuneus
18	Right Cerebrum
17	Gray Matter
13	brodmann area 18
13	Left Cerebrum
9	White Matter
7	Lingual Gyrus
7	Inter-Hemispheric
7	Calcarine_R (aal)
4	brodmann area 17

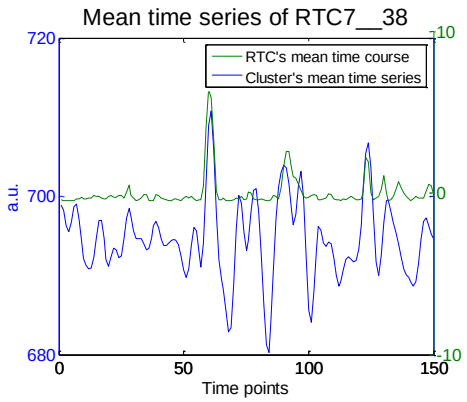

Patient 2 – Bilateral TLE: with right temporo-parietal predominance

RTCs temporal profile obtained with the 2dTCA.

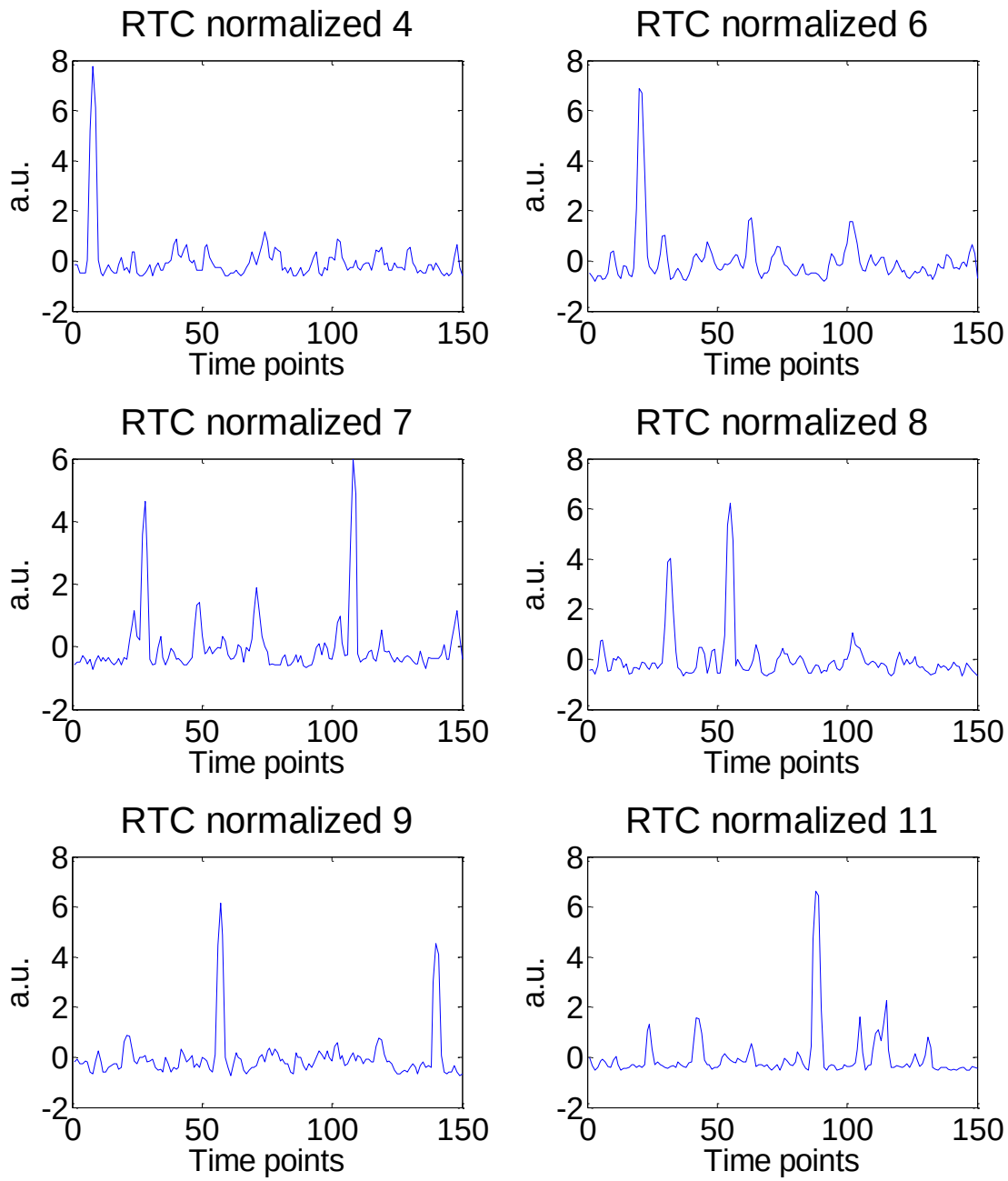

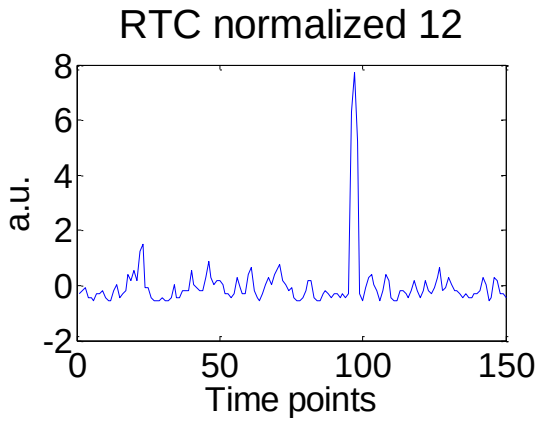
RTC normalized 12
a.u.
8
6
4
2
0
-2
0
50
100
150
Time points

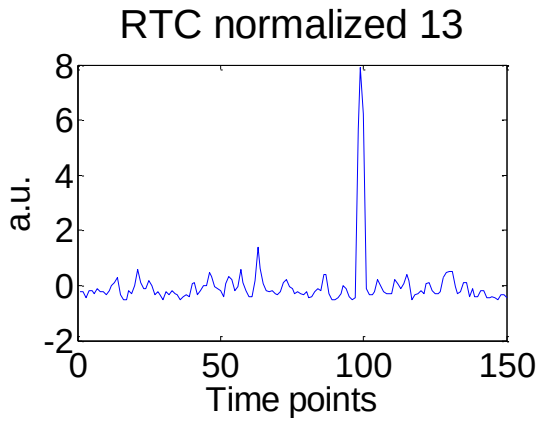
RTC normalized 13
a.u.
8
6
4
2
0
-2
0
50
100
150
Time points

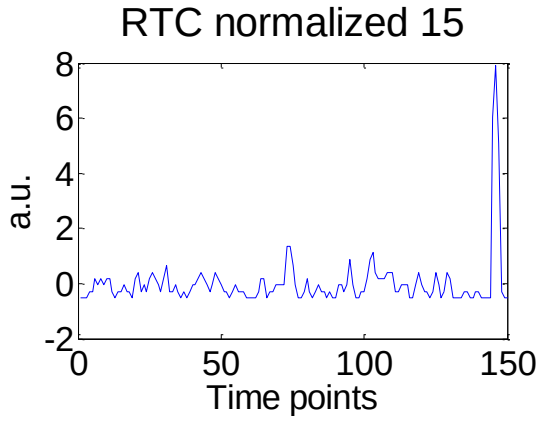
RTC normalized 15
a.u.
8
6
4
2
0
-2
0
50
100
150
Time points

Spatial location of each RTC's clusters and corresponding temporal profiles

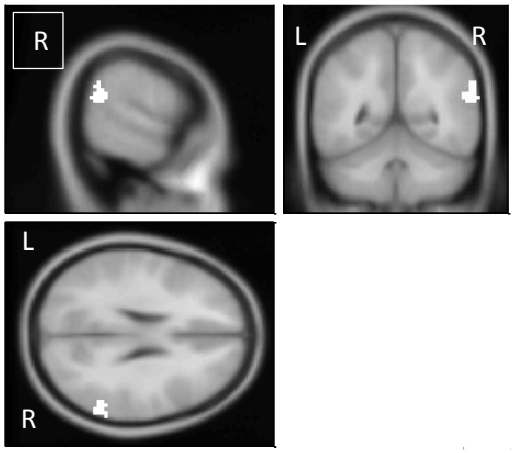

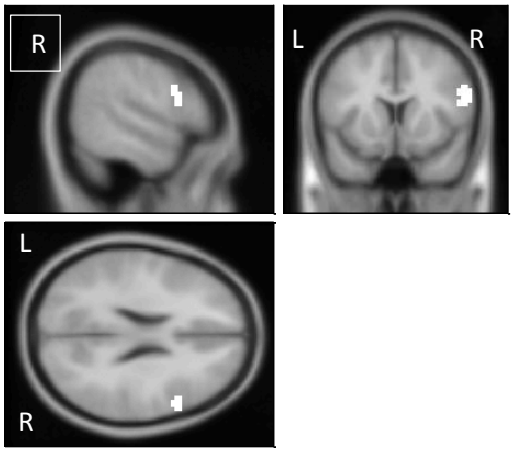

RTC2_58	
# voxels	structure
58	--TOTAL # VOXELS--
58	Right Cerebrum
37	Supramarginal Gyrus
35	Temporal Lobe
31	Gray Matter
28	brodmann area 40
25	White Matter
24	Temporal_Sup_R (aal)
23	Parietal Lobe
19	Angular_R (aal)
12	Superior Temporal Gyrus
9	Inferior Parietal Lobule
9	SupraMarginal_R (aal)
4	Temporal_Mid_R (aal)
3	brodmann area 22

RTC3_50	
# voxels	structure
50	--TOTAL # VOXELS--
50	Frontal Lobe
50	Right Cerebrum
47	Inferior Frontal Gyrus
39	Frontal_Inf_Oper_R (aal)
33	White Matter
17	Gray Matter
12	brodmann area 44
8	Frontal_Inf_Tri_R (aal)
3	brodmann area 9
3	Precentral_R (aal)
2	Sub-Gyral
2	brodmann area 45
1	Middle Frontal Gyrus

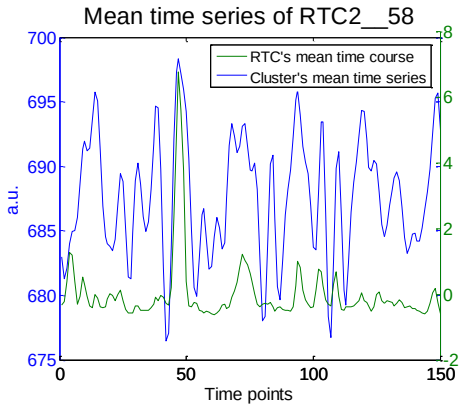

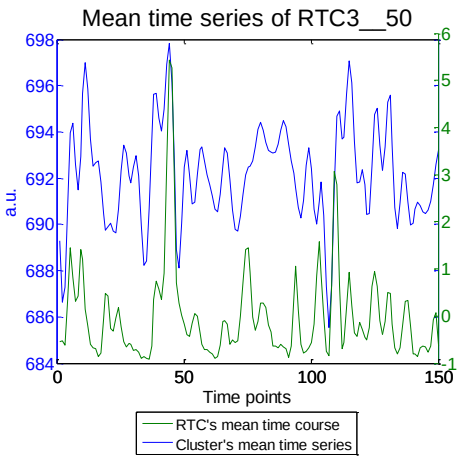

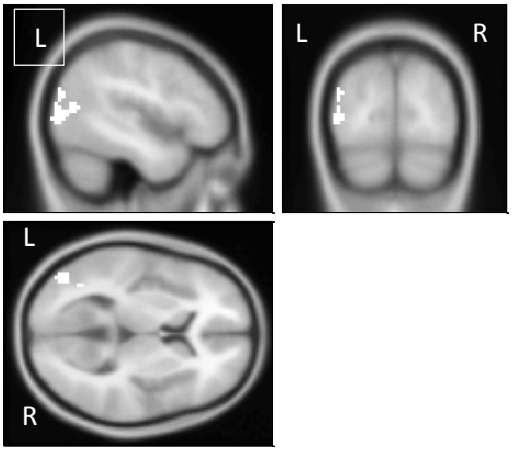

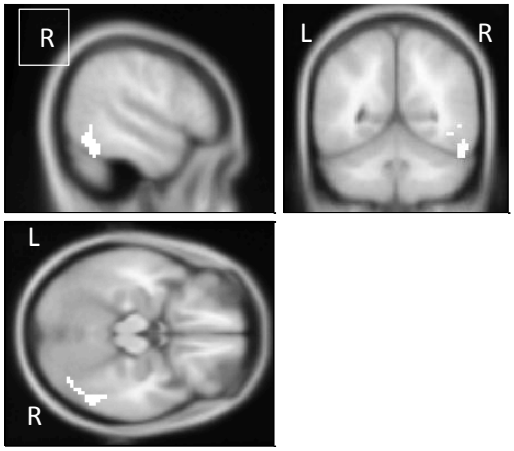

RTC3_93

# voxels	structure
93	--TOTAL # VOXELS--
92	Left Cerebrum
69	Occipital_Mid_L (aal)
58	Occipital Lobe
51	White Matter
46	Middle Temporal Gyrus
34	Temporal Lobe
33	Gray Matter
32	Middle Occipital Gyrus
17	brodmann area 19
16	brodmann area 39
14	Superior Occipital Gyrus
14	Temporal_Mid_L (aal)

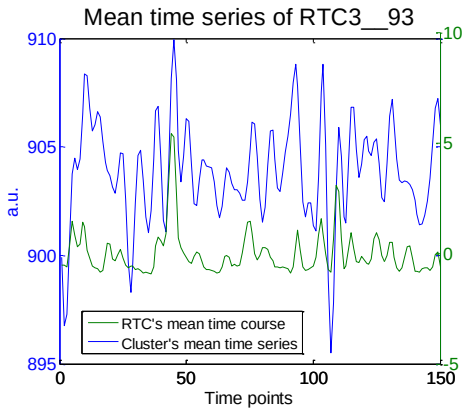

RTC3_100

# voxels	structure
100	--TOTAL # VOXELS--
79	Right Cerebrum
65	Temporal_Inf_R (aal)
49	Temporal Lobe
46	Gray Matter
30	Fusiform Gyrus
30	brodmann area 37
30	Occipital Lobe
29	White Matter
19	Cerebelum_Crus1_R (aal)
17	Cerebellum Posterior Lobe
17	Right Cerebellum
17	Declive
17	Middle Occipital Gyrus
14	Inferior Temporal Gyrus
11	Sub-Gyral
11	brodmann area 20
8	Fusiform_R (aal)
7	Occipital_Inf_R (aal)
7	Middle Temporal Gyrus
5	brodmann area 19
1	Cerebelum_6_R (aal)

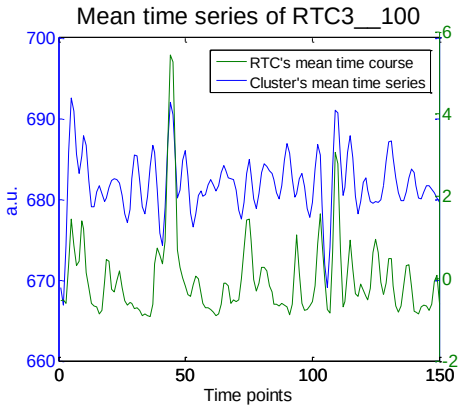

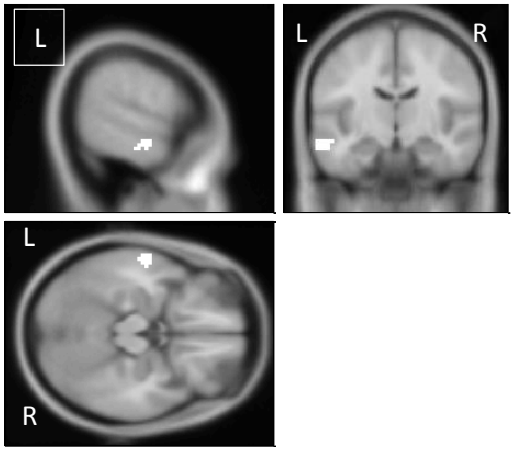

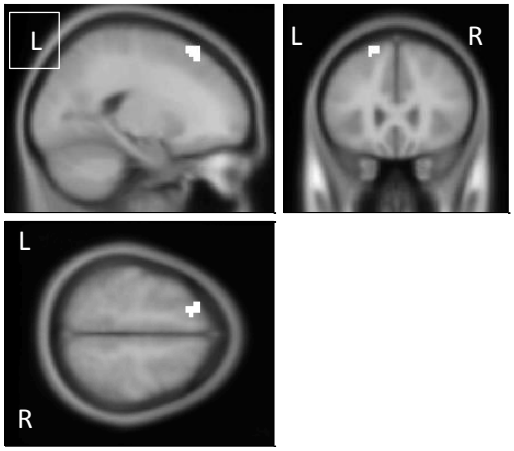

RTC5_28

# voxels	structure
28	--TOTAL # VOXELS--
28	Left Cerebrum
28	Temporal Lobe
27	Temporal_Mid_L (aal)
17	Middle Temporal Gyrus
17	White Matter
11	Gray Matter
11	brodmann area 21
11	Inferior Temporal Gyrus
1	Temporal_Inf_L (aal)

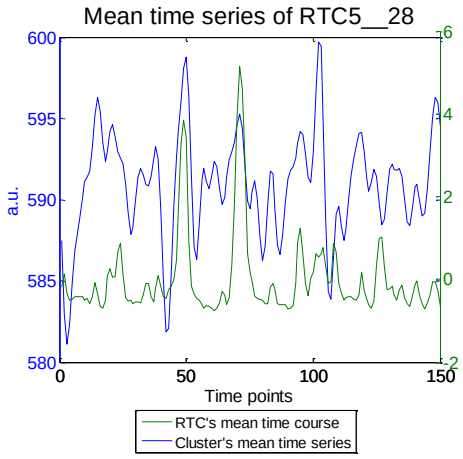

RTC5_28b

# voxels	structure
28	--TOTAL # VOXELS--
26	Frontal Lobe
26	Left Cerebrum
25	Superior Frontal Gyrus
20	Gray Matter
17	Frontal_Sup_L (aal)
16	brodmann area 8
9	Frontal_Mid_L (aal)
5	White Matter
4	brodmann area 6
1	Middle Frontal Gyrus

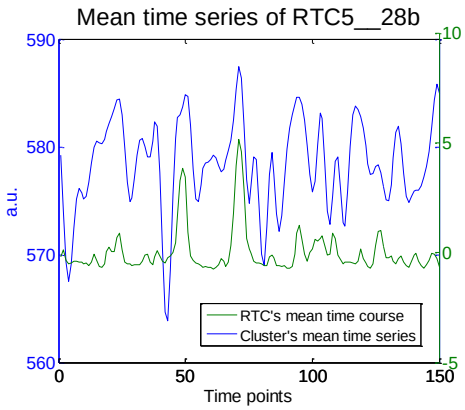

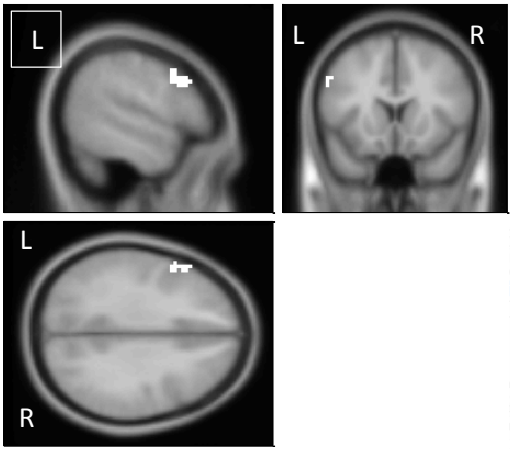

RTC5_35

# voxels	structure
35	--TOTAL # VOXELS--
35	Frontal Lobe
35	Left Cerebrum
25	Gray Matter
22	Middle Frontal Gyrus
21	Precentral_L (aal)
19	brodmann area 9
13	Inferior Frontal Gyrus
10	White Matter
6	Frontal_Inf_Oper_L (aal)
6	brodmann area 8
5	Frontal_Mid_L (aal)
3	Frontal_Inf_Tri_L (aal)

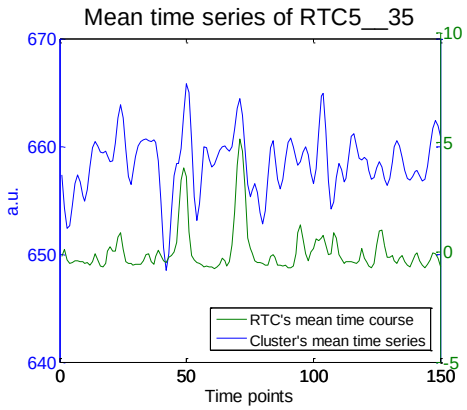

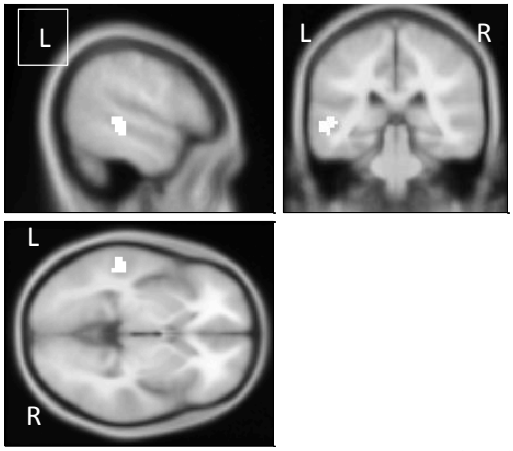

RTC5_44

# voxels	structure
44	--TOTAL # VOXELS--
44	Left Cerebrum
44	Temporal Lobe
44	Temporal_Mid_L (aal)
39	Middle Temporal Gyrus
38	White Matter
6	Gray Matter
4	Superior Temporal Gyrus
3	brodmann area 22
3	brodmann area 21
1	Sub-Gyral

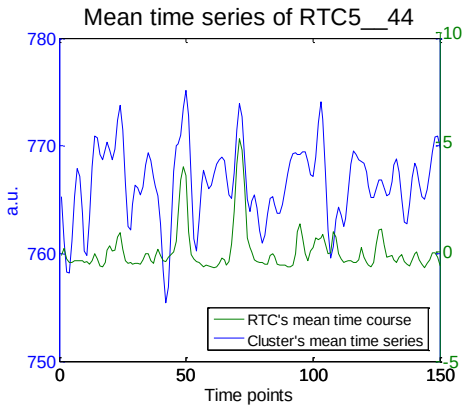

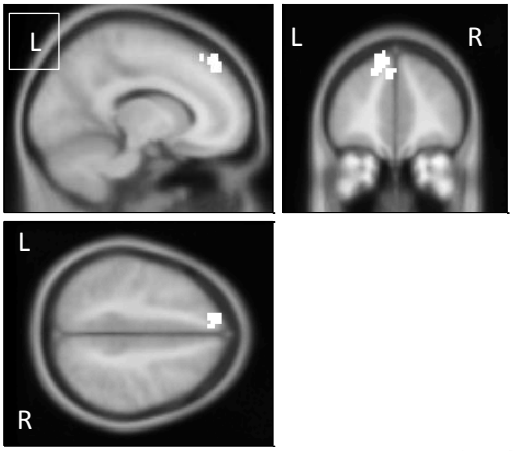

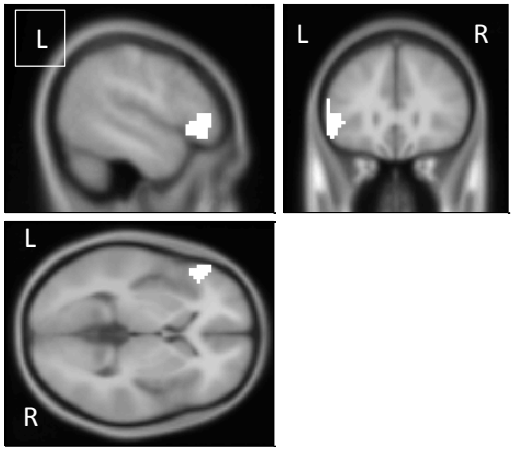

RTC5_76

# voxels	structure
76	--TOTAL # VOXELS--
71	Left Cerebrum
71	Frontal Lobe
56	Superior Frontal Gyrus
51	White Matter
47	Frontal_Sup_L (aal)
28	Frontal_Sup_Medial_L (aal)
19	Gray Matter
15	Medial Frontal Gyrus
13	brodmann area 8
3	brodmann area 9
3	brodmann area 6
1	Inter-Hemispheric

RTC5_113

# voxels	structure
113	--TOTAL # VOXELS--
113	Frontal Lobe
113	Left Cerebrum
110	Inferior Frontal Gyrus
85	White Matter
59	Frontal_Inf_Orb_L (aal)
54	Frontal_Inf_Tri_L (aal)
28	Gray Matter
18	brodmann area 47
5	brodmann area 46
4	brodmann area 45
3	Middle Frontal Gyrus
1	brodmann area 10

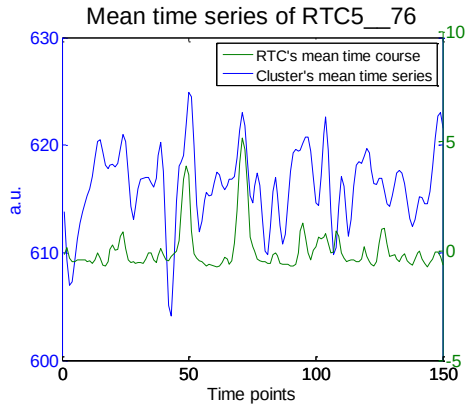

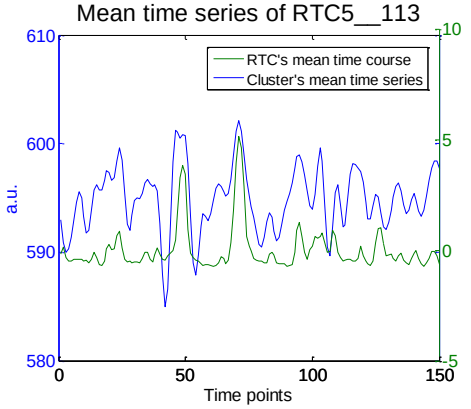

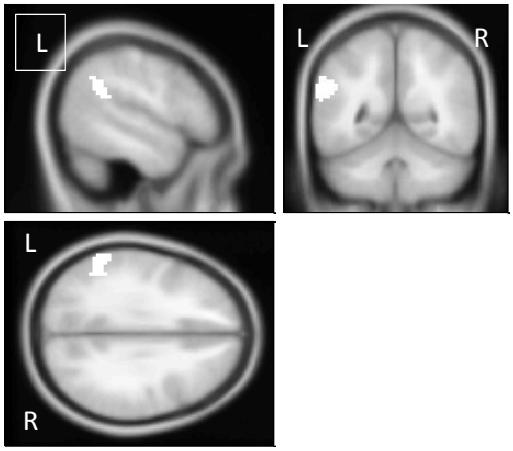

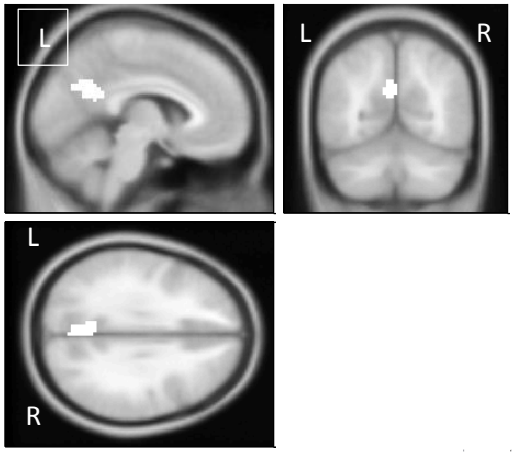

RTC5_125

# voxels	structure
125	--TOTAL # VOXELS--
125	Left Cerebrum
96	Parietal Lobe
83	Supramarginal Gyrus
78	White Matter
76	SupraMarginal_L (aal)
44	Gray Matter
43	brodmann area 40
34	Inferior Parietal Lobule
29	Temporal Lobe
18	Temporal_Sup_L (aal)
16	Angular_L (aal)
8	Superior Temporal Gyrus
8	Temporal_Mid_L (aal)
5	Parietal_Inf_L (aal)
1	brodmann area 39

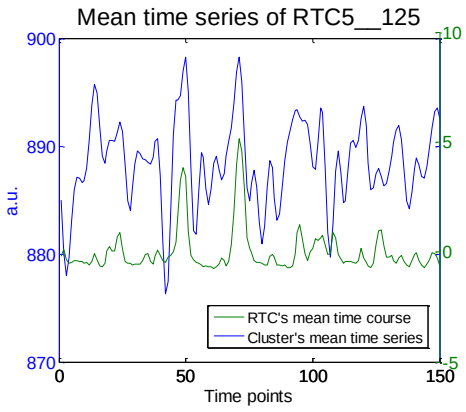

RTC5_140

# voxels	structure
140	--TOTAL # VOXELS--
119	Left Cerebrum
84	Precuneus_L (aal)
75	Precuneus
63	Parietal Lobe
50	Gray Matter
48	White Matter
47	Limbic Lobe
31	Posterior Cingulate
30	Cuneus_L (aal)
29	brodmann area 31
18	Occipital Lobe
17	brodmann area 7
17	Cingulum_Post_L (aal)
15	Cingulate Gyrus
12	Inter-Hemispheric
9	Precuneus_R (aal)
9	Right Cerebrum
6	Cuneus
3	brodmann area 23
1	brodmann area 30

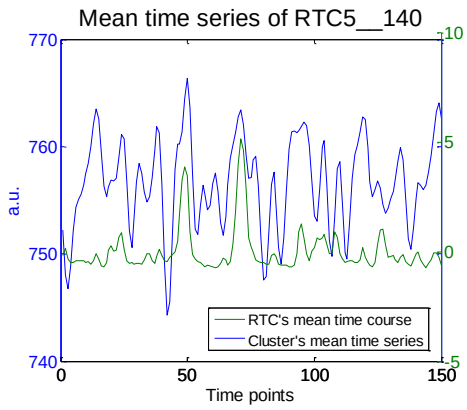

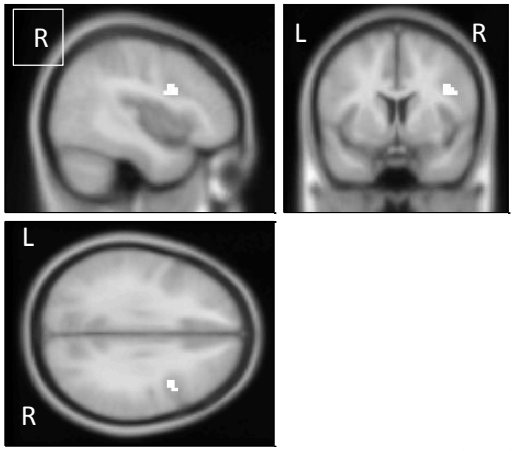

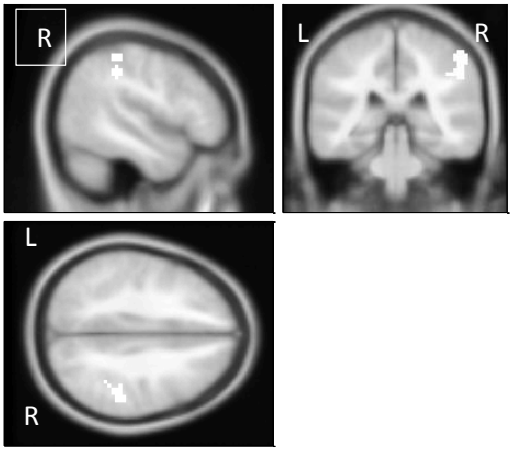

RTC10_33

# voxels	structure
33	--TOTAL # VOXELS--
33	Frontal Lobe
33	Right Cerebrum
31	White Matter
24	Frontal_Inf_Oper_R (aal)
17	Sub-Gyral
13	Inferior Frontal Gyrus
5	Frontal_Inf_Tri_R (aal)
4	Precentral_R (aal)
3	Middle Frontal Gyrus
2	brodmann area 9
2	Gray Matter

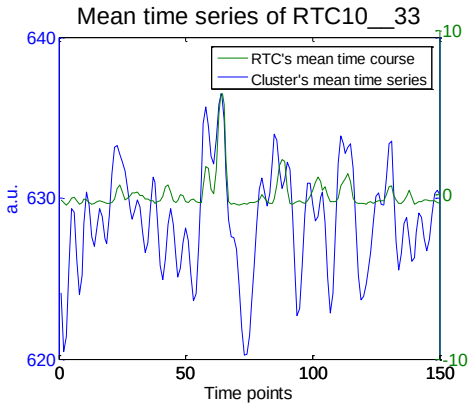

RTC10_92

# voxels	structure
92	--TOTAL # VOXELS--
89	Parietal Lobe
89	Right Cerebrum
57	Inferior Parietal Lobule
51	Gray Matter
45	brodmann area 40
42	Parietal_Inf_R (aal)
40	SupraMarginal_R (aal)
30	Postcentral Gyrus
27	White Matter
6	brodmann area 2
5	Parietal_Sup_R (aal)
3	Postcentral_R (aal)
2	Supramarginal Gyrus

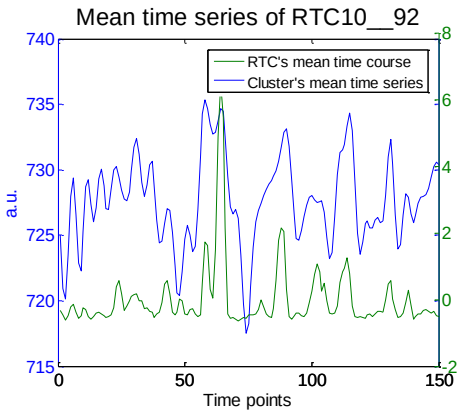

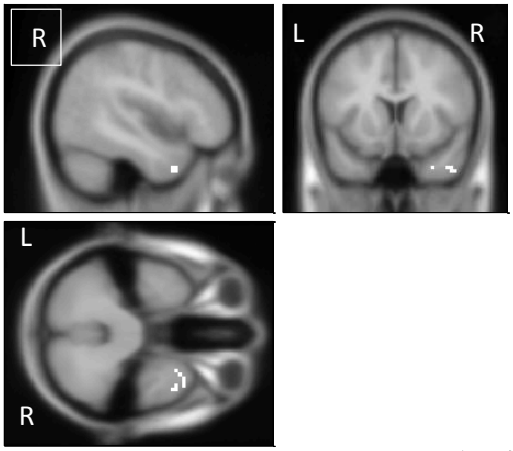

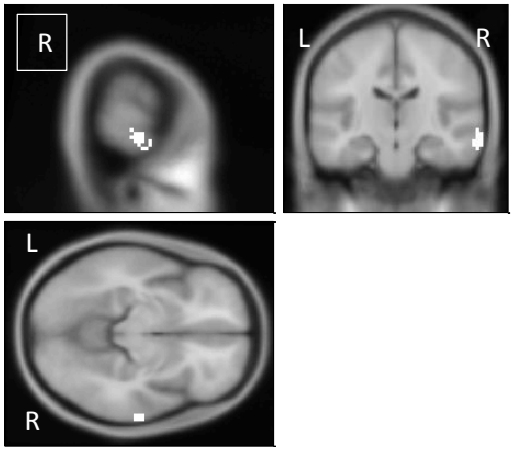

RTC14_27

# voxels	structure
27	--TOTAL # VOXELS--
25	Right Cerebrum
25	Temporal Lobe
19	Superior Temporal Gyrus
17	Temporal_Pole_Mid_R (aal)
15	Gray Matter
12	brodmann area 38
8	Temporal_Pole_Sup_R (aal)
6	Middle Temporal Gyrus
6	White Matter
3	brodmann area 21
2	Temporal_Inf_R (aal)

RTC14_48

# voxels	structure
48	--TOTAL # VOXELS--
45	Temporal_Mid_R (aal)
31	Right Cerebrum
31	Temporal Lobe
26	Middle Temporal Gyrus
20	Gray Matter
19	brodmann area 21
5	Inferior Temporal Gyrus
5	White Matter
3	Temporal_Sup_R (aal)
1	brodmann area 20

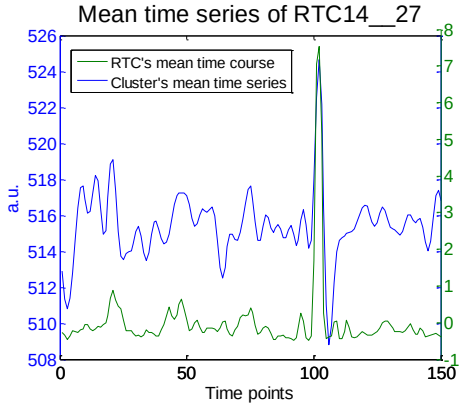

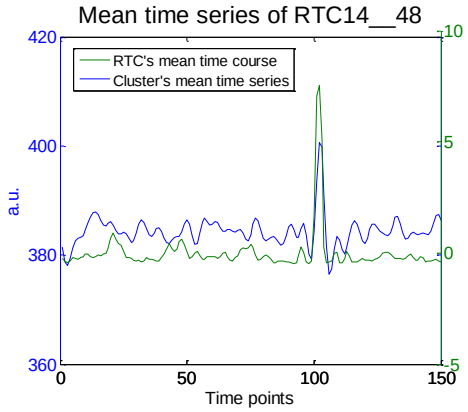

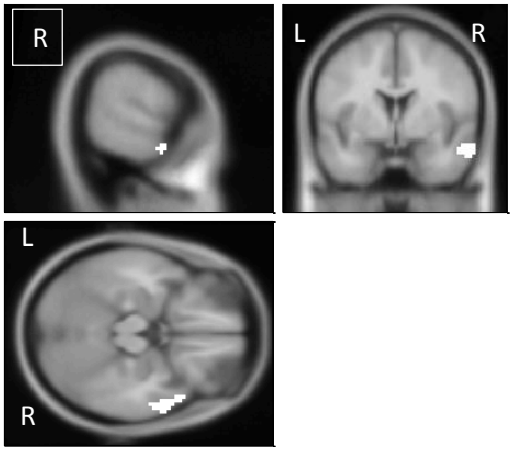

RTC14_115

# voxels	structure
115	--TOTAL # VOXELS--
108	Right Cerebrum
108	Temporal Lobe
75	Middle Temporal Gyrus
59	Temporal_Mid_R (aal)
58	Gray Matter
42	brodmann area 21
41	Temporal_Pole_Mid_R (aal)
30	White Matter
21	Superior Temporal Gyrus
14	brodmann area 38
14	Temporal_Pole_Sup_R (aal)
11	Inferior Temporal Gyrus
2	brodmann area 20
1	Fusiform Gyrus
1	Temporal_Inf_R (aal)

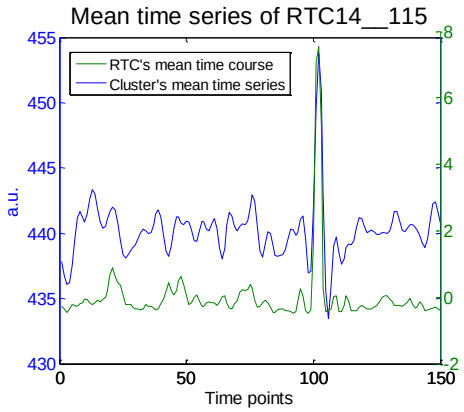

Patient 3 – FCDE: right precentral gyrus

RTCs temporal profile obtained with the 2dTCA.

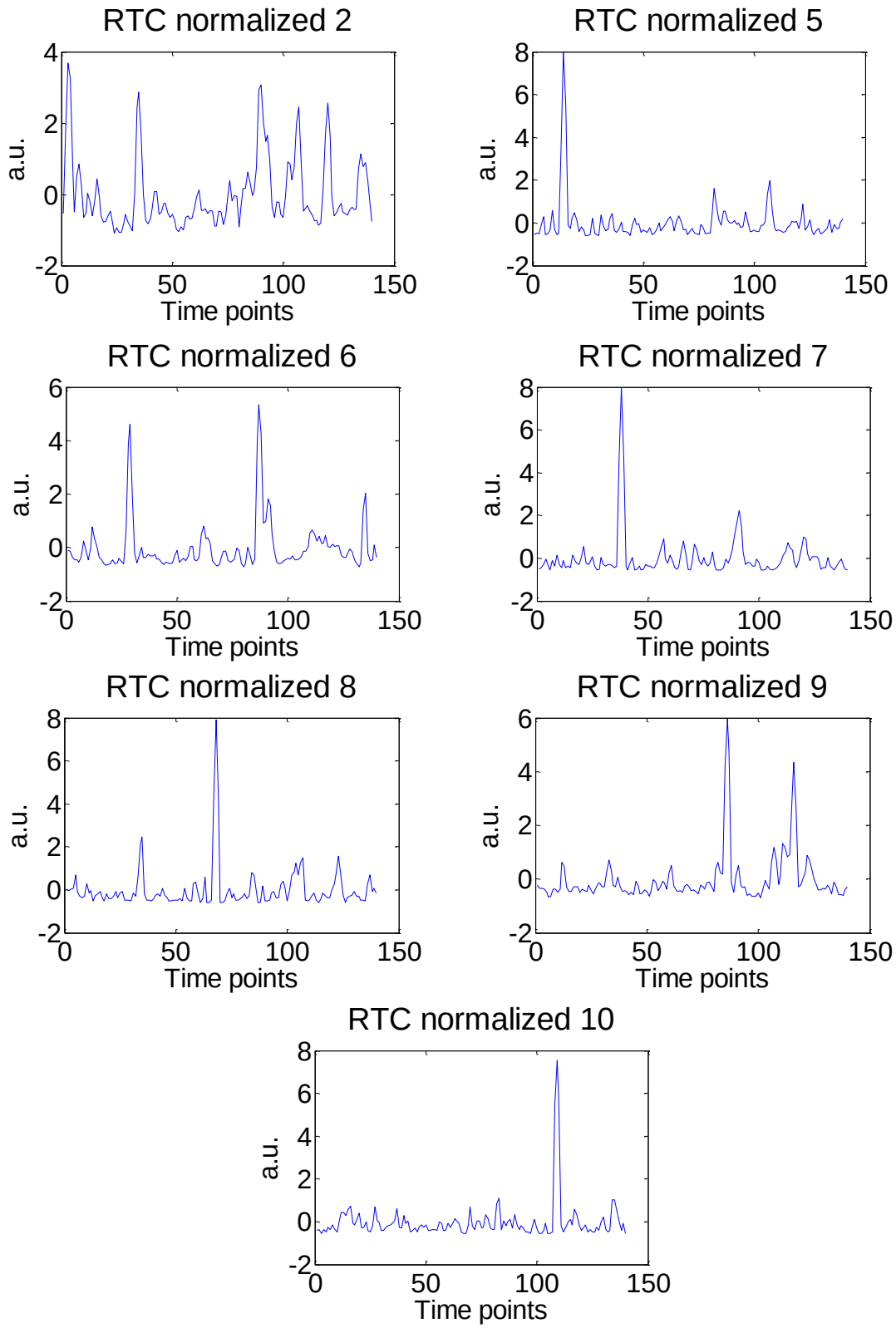

Spatial location of each RTC's clusters and corresponding temporal profiles

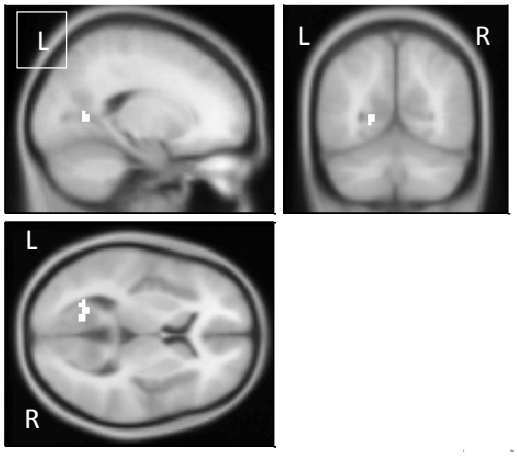

RTC1_28

# voxels	structure
28	--TOTAL # VOXELS--
28	Left Cerebrum
23	Calcarine_L (aal)
19	White Matter
18	Limbic Lobe
18	Posterior Cingulate
8	Occipital Lobe
7	brodmann area 30
7	Gray Matter
4	Cuneus
3	Lingual Gyrus
2	Sub-lobar
1	Lateral Ventricle
1	Middle Occipital Gyrus
1	Extra-Nuclear
1	Cerebro-Spinal Fluid

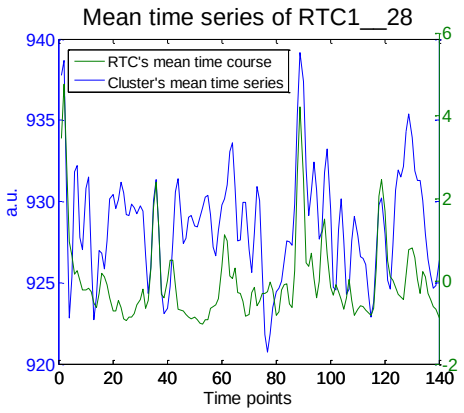

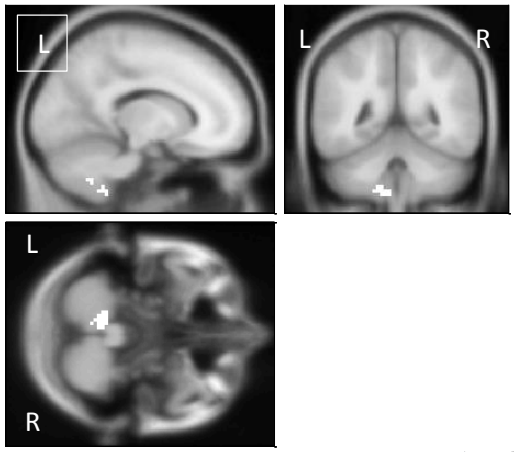

RTC1_34

# voxels	structure
34	--TOTAL # VOXELS--
27	Cerebelum_9_L (aal)
13	Left Cerebellum
13	Cerebellum Posterior Lobe
11	Cerebellar Tonsil
7	Cerebelum_8_L (aal)
2	Inferior Semi-Lunar Lobule

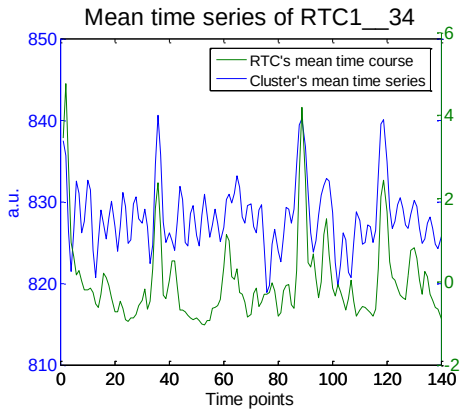

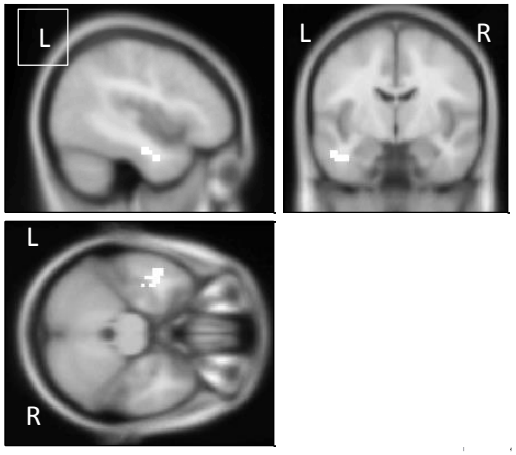

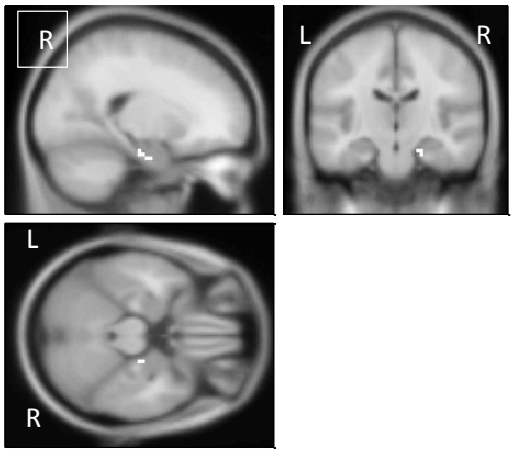

RTC1_42

# voxels	structure
42	--TOTAL # VOXELS--
42	Left Cerebrum
42	Temporal Lobe
28	White Matter
26	Temporal_Inf_L (aal)
18	Fusiform Gyrus
17	Sub-Gyral
14	Temporal_Mid_L (aal)
12	Gray Matter
10	brodmann area 20
5	Middle Temporal Gyrus
2	brodmann area 21
2	Inferior Temporal Gyrus
1	Fusiform_L (aal)

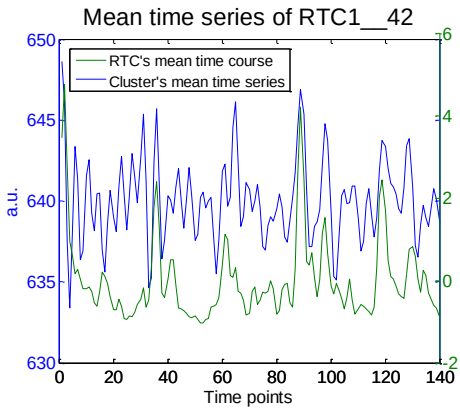

RTC1_80

# voxels	structure
80	--TOTAL # VOXELS--
80	Right Cerebrum
60	White Matter
48	Temporal Lobe
32	Limbic Lobe
28	Temporal_Pole_Mid_R (aal)
22	Uncus
19	Gray Matter
18	ParaHippocampal_R (aal)
18	Temporal_Inf_R (aal)
18	Middle Temporal Gyrus
16	Sub-Gyral
12	Fusiform_R (aal)
9	Parahippocampa Gyrus
8	brodmann area 21
7	Superior Temporal Gyrus
7	Inferior Temporal Gyrus
4	brodmann area 20
3	brodmann area 38
2	brodmann area 28
2	brodmann area 35
1	Fusiform Gyrus
1	Temporal_Pole_Sup_R (aal)

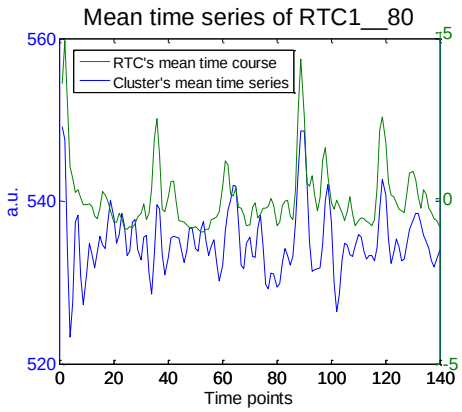

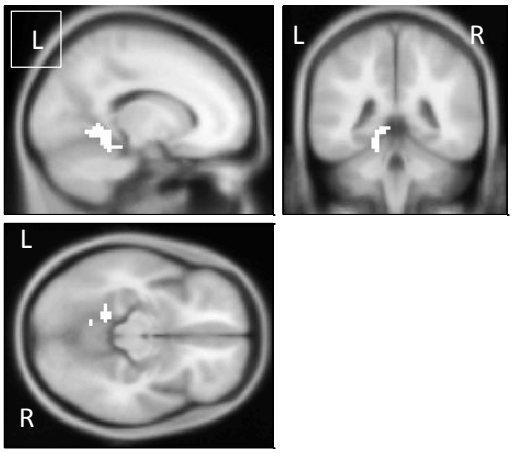

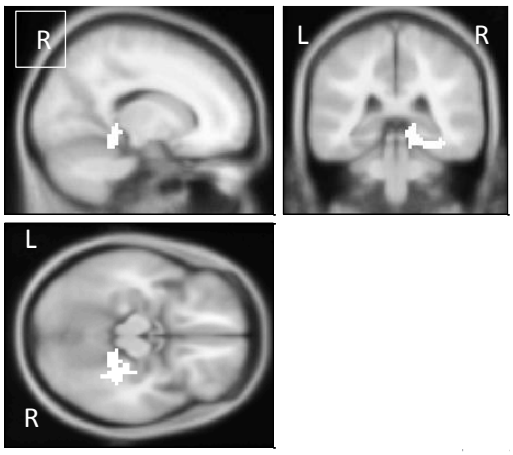

RTC1_81

# voxels	structure
81	--TOTAL # VOXELS--
46	Lingual_L (aal)
40	Left Cerebrum
36	Cerebellum Anterior Lobe
36	Culmen
36	Left Cerebellum
25	Limbic Lobe
23	Cerebelum_4_5_L (aal)
22	Parahippocampa Gyrus
19	Gray Matter
15	White Matter
15	Occipital Lobe
13	Lingual Gyrus
11	brodmann area 19
8	Fusiform_L (aal)
7	brodmann area 30
5	Sub-Gyral
3	Cerebelum_3_L (aal)
2	Midbrain
2	Left Brainstem
1	brodmann area 37

RTC1_132

# voxels	structure
132	--TOTAL # VOXELS--
94	Right Cerebrum
62	Limbic Lobe
61	Fusiform_R (aal)
57	Parahippocampa Gyrus
43	White Matter
39	Gray Matter
30	ParaHippocampal_R (aal)
29	Culmen
29	Cerebellum Anterior Lobe
29	Right Cerebellum
28	Fusiform Gyrus
27	Temporal Lobe
21	Lingual_R (aal)
16	brodmann area 36
13	Cerebelum_4_5_R (aal)
12	brodmann area 37
7	brodmann area 30
6	Sub-Gyral
5	Occipital Lobe
3	Cerebelum_3_R (aal)
2	brodmann area 20
1	Right Brainstem
1	brodmann area 35
1	Temporal_Inf_R (aal)
1	Hippocampus_R (aal)
1	brodmann area 19

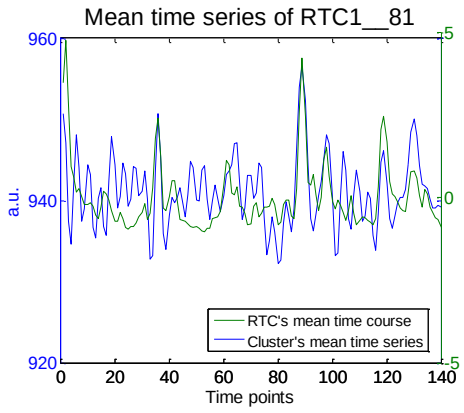

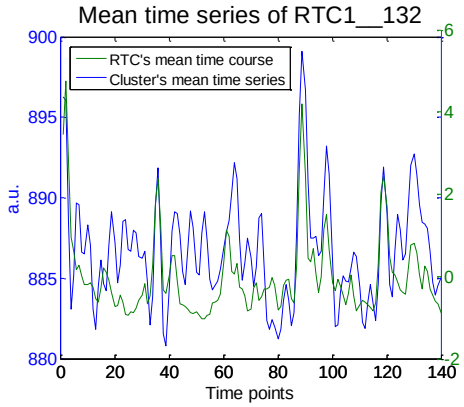

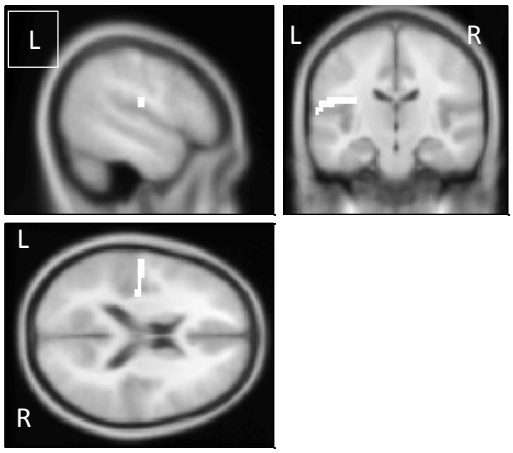

RTC3_64

# voxels	structure
64	--TOTAL # VOXELS--
64	Left Cerebrum
36	White Matter
35	Parietal Lobe
32	Postcentral Gyrus
32	Postcentral_L (aal)
25	Gray Matter
16	Sub-lobar
15	Insula
12	Rolandic_Oper_L (aal)
9	Temporal Lobe
8	brodmann area 43
8	Temporal_Sup_L (aal)
7	Insula_L (aal)
6	Transverse Temporal Gyrus
6	brodmann area 42
5	brodmann area 13
4	Frontal Lobe
4	Precentral Gyrus
3	Superior Temporal Gyrus
3	Sub-Gyral
3	brodmann area 4
2	SupraMarginal_L (aal)
1	brodmann area 40
1	Extra-Nuclear

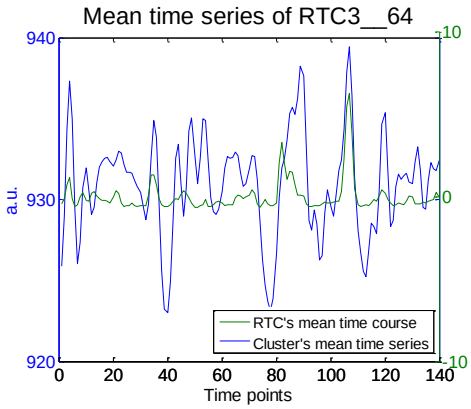

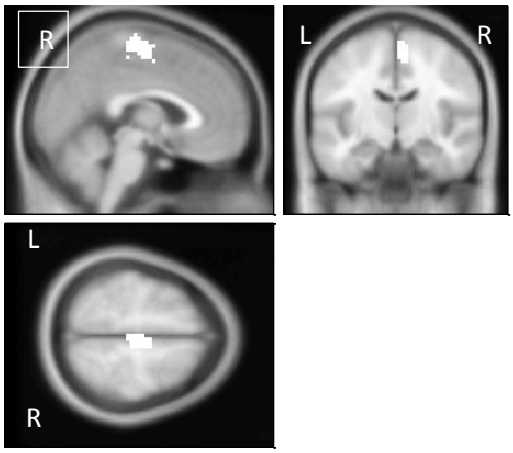

RTC3_136

# voxels	structure
136	--TOTAL # VOXELS--
124	Frontal Lobe
116	Right Cerebrum
110	Medial Frontal Gyrus
104	Supp_Motor_Area_R (aal)
76	brodmann area 6
76	Gray Matter
44	White Matter
12	Paracentral_Lobule_L (aal)
12	Inter-Hemispheric
10	Paracentral Lobule
9	Paracentral_Lobule_R (aal)
8	Left Cerebrum
4	Cingulum_Mid_R (aal)
4	Sub-Gyral
2	Supp_Motor_Area_L (aal)

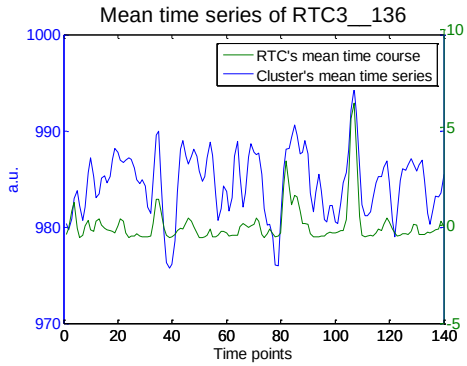

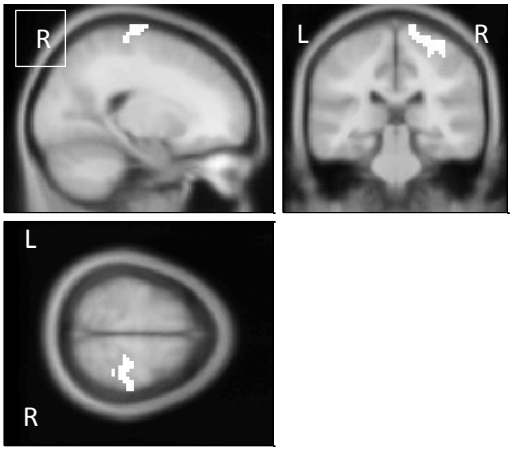

RTC3_170

# voxels	structure
170	--TOTAL # VOXELS--
166	Right Cerebrum
119	Frontal Lobe
118	Precentral Gyrus
95	Precentral_R (aal)
76	Gray Matter
70	White Matter
66	Postcentral_R (aal)
47	Parietal Lobe
42	Postcentral Gyrus
27	brodmann area 4
25	brodmann area 3
17	brodmann area 6
7	Paracentral_Lobule_R (aal)
5	brodmann area 2
4	Superior Frontal Gyrus
1	brodmann area 40
1	brodmann area 5
1	Inferior Parietal Lobule
1	Paracentral Lobule

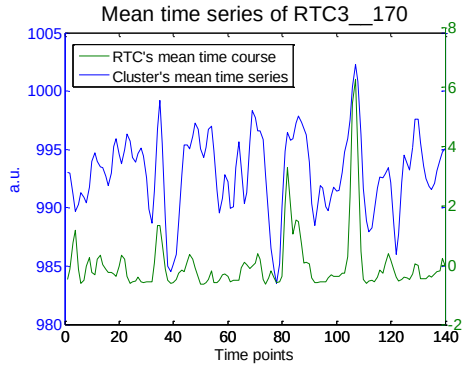

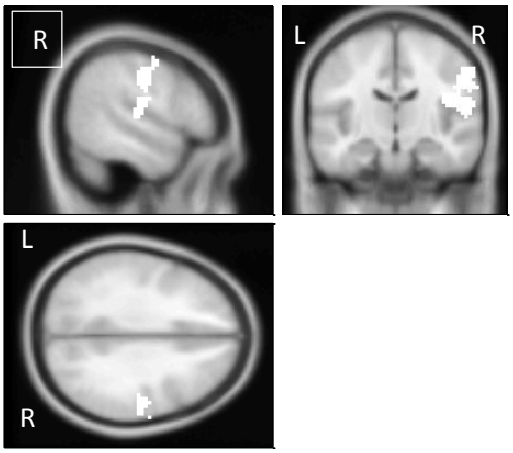

RTC3_275

# voxels	structure
275	--TOTAL # VOXELS--
265	Right Cerebrum
145	White Matter
129	Frontal Lobe
118	Precentral Gyrus
107	Postcentral_R (aal)
103	Gray Matter
71	Parietal Lobe
70	Rolandic_Oper_R (aal)
66	Postcentral Gyrus
36	Precentral_R (aal)
34	brodmann area 6
33	Sub-lobar
32	Temporal Lobe
29	Insula
22	Temporal_Sup_R (aal)
19	Transverse Temporal Gyrus
19	brodmann area 4
13	Frontal_Mid_R (aal)
13	Superior Temporal Gyrus
13	brodmann area 3
11	brodmann area 41
9	Sub-Gyral
9	brodmann area 42
8	SupraMarginal_R (aal)
8	brodmann area 13
6	brodmann area 43

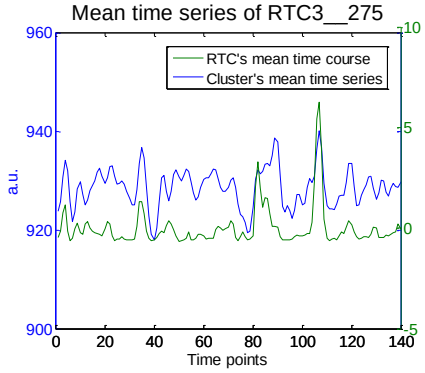

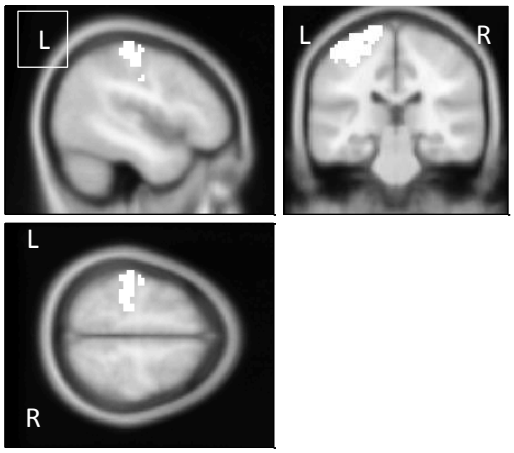

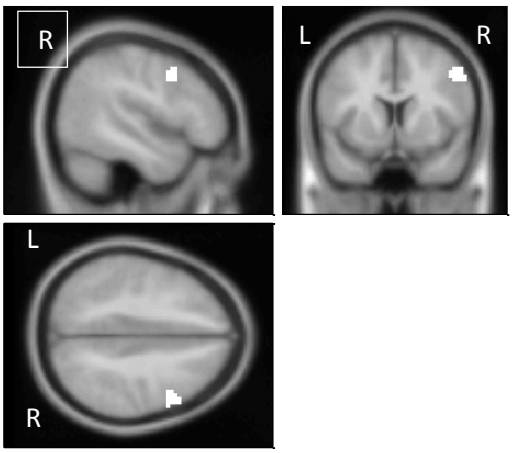

RTC3_354

# voxels	structure
354	--TOTAL # VOXELS--
325	Left Cerebrum
236	Postcentral_L (aal)
167	Parietal Lobe
167	Postcentral Gyrus
162	Gray Matter
158	Frontal Lobe
153	Precentral Gyrus
122	White Matter
80	Precentral_L (aal)
66	brodmann area 3
54	brodmann area 4
30	Paracentral_Lobule_L (aal)
15	brodmann area 2
15	brodmann area 1
12	brodmann area 6
4	Sub-Gyral
4	Parietal_Inf_L (aal)
1	Superior Frontal Gyrus

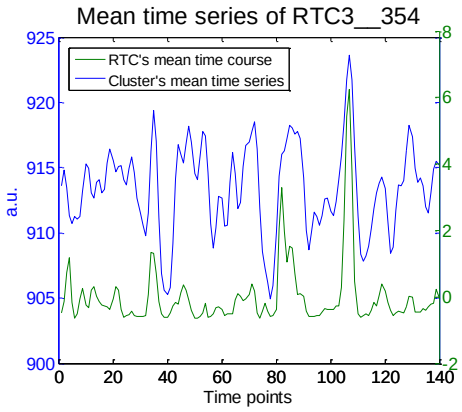

RTC4_55

# voxels	structure
55	--TOTAL # VOXELS--
55	Frontal Lobe
55	Right Cerebrum
40	Precentral_R (aal)
32	Gray Matter
29	Middle Frontal Gyrus
23	Inferior Frontal Gyrus
15	brodmann area 9
15	White Matter
14	Frontal_Mid_R (aal)
13	brodmann area 8
4	brodmann area 6
3	Precentral Gyrus
1	Frontal_Inf_Oper_R (aal)

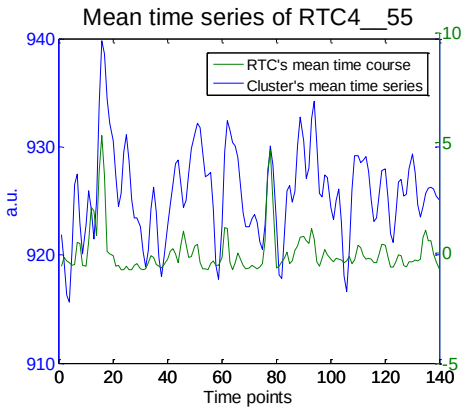

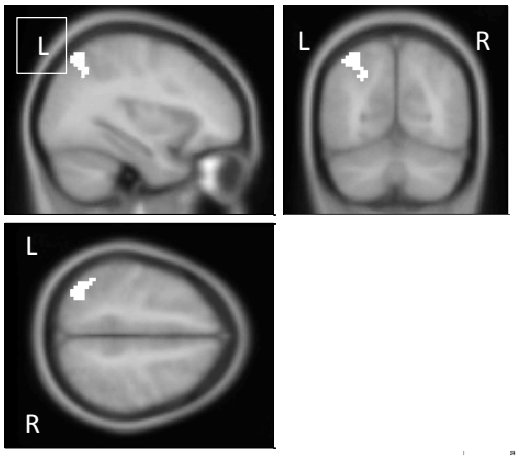

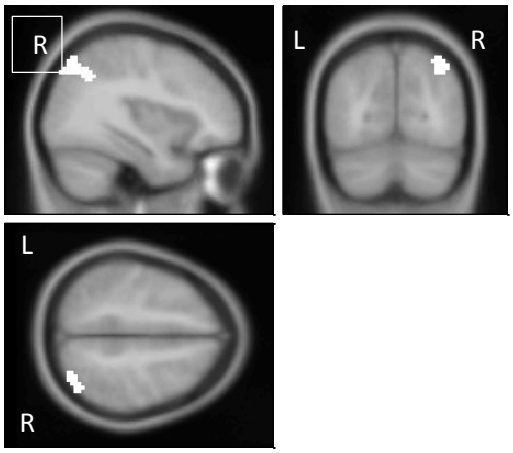

RTC4_87

# voxels	structure
87	--TOTAL # VOXELS--
70	Parietal Lobe
70	Left Cerebrum
38	White Matter
37	Parietal_Sup_L (aal)
32	Superior Parietal Lobule
31	Gray Matter
25	brodmann area 7
25	Parietal_Inf_L (aal)
23	Inferior Parietal Lobule
18	Angular_L (aal)
15	Precuneus
6	brodmann area 40
3	Occipital_Sup_L (aal)
2	Occipital_Mid_L (aal)

RTC4_123

# voxels	structure
123	--TOTAL # VOXELS--
98	Angular_R (aal)
95	Right Cerebrum
95	Parietal Lobe
57	Inferior Parietal Lobule
48	White Matter
46	Gray Matter
21	brodmann area 7
18	Superior Parietal Lobule
13	brodmann area 40
12	Parietal_Sup_R (aal)
10	Occipital_Sup_R (aal)
9	Angular Gyrus
9	Precuneus
7	brodmann area 19
5	brodmann area 39
2	Sub-Gyral
2	Parietal_Inf_R (aal)

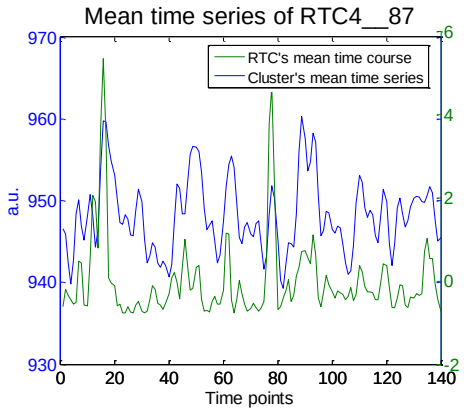

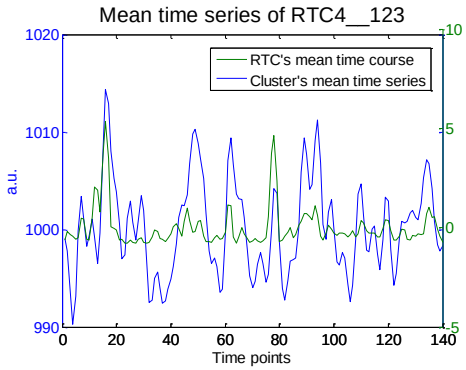

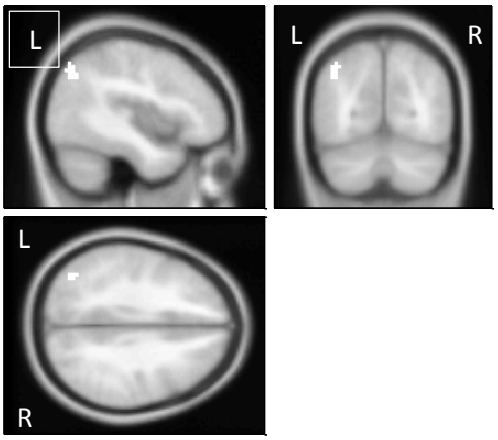

RTC11_39

# voxels	structure
39	--TOTAL # VOXELS--
29	Parietal Lobe
29	Left Cerebrum
22	Gray Matter
21	Angular_L (aal)
12	Precuneus
11	Inferior Parietal Lobule
10	Parietal_Inf_L (aal)
9	brodmann area 39
8	brodmann area 19
5	brodmann area 7
5	White Matter
4	Superior Parietal Lobule
2	Occipital_Mid_L (aal)
2	Angular Gyrus

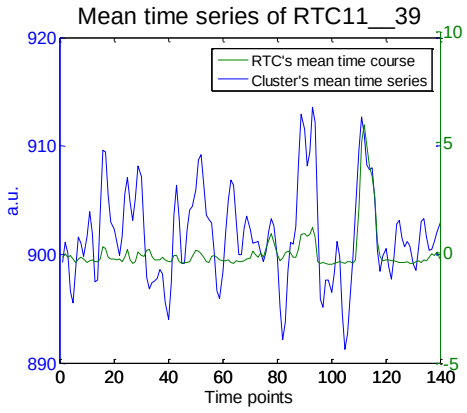

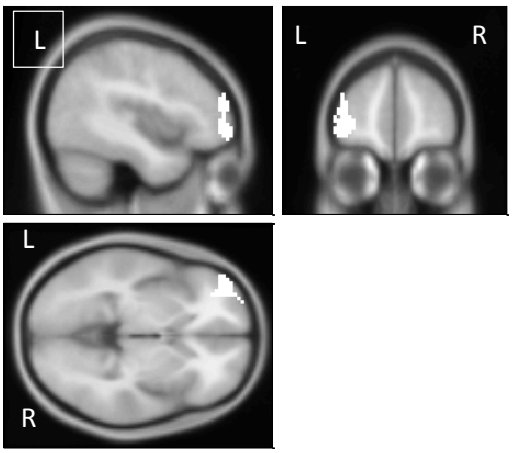

RTC11_166

# voxels	structure
166	--TOTAL # VOXELS--
159	Left Cerebrum
159	Frontal Lobe
130	Middle Frontal Gyrus
89	White Matter
81	Frontal_Mid_L (aal)
64	Frontal_Mid_Orb_L (aal)
59	Gray Matter
46	brodmann area 10
17	Superior Frontal Gyrus
9	Inferior Frontal Gyrus
7	brodmann area 11
3	Sub-Gyral
3	Frontal_Sup_L (aal)
2	brodmann area 47
1	Frontal_Sup_Orb_L (aal)
1	brodmann area 46
1	Frontal_Inf_Tri_L (aal)
1	Frontal_Inf_Orb_L (aal)

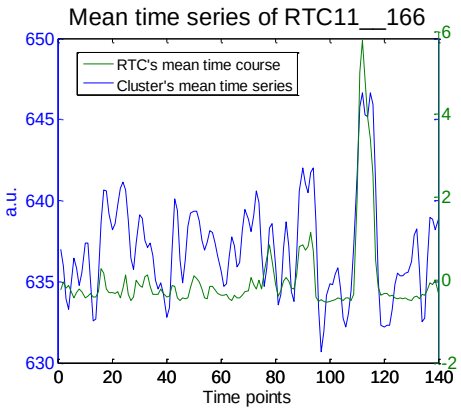

Information of 90 AAL Regions used in cluster report with xjView

Labels	Regions	Regions
1	Precentral_L	Precental gyrus
2	Precentral_R	Precental gyrus
3	Frontal_Sup_L	Superior frontal gyrus, dorsolateral
4	Frontal_Sup_R	Superior frontal gyrus, dorsolateral
5	Frontal_Sup_Orb_L	Superior frontal gyrus, orbital part
6	Frontal_Sup_Orb_R	Superior frontal gyrus, orbital part
7	Frontal_Mid_L	Middle frontal gyrus
8	Frontal_Mid_R	Middle frontal gyrus
9	Frontal_Mid_Orb_L	Middle frontal gyrus, orbital part
10	Frontal_Mid_Orb_R	Middle frontal gyrus, orbital part
11	Frontal_Inf_Oper_L	Inferior frontal gyrus, opercular part
12	Frontal_Inf_Oper_R	Inferior frontal gyrus, opercular part
13	Frontal_Inf_Tri_L	Inferior frontal gyrus, triangular part
14	Frontal_Inf_Tri_R	Inferior frontal gyrus, triangular part
15	Frontal_Inf_Orb_L	Inferior frontal gyrus, orbital part
16	Frontal_Inf_Orb_R	Inferior frontal gyrus, orbital part
17	Rolandic_Oper_L	Rolandic operculum
18	Rolandic_Oper_R	Rolandic operculum
19	Supp_Motor_Area_L	Supplementary motor area
20	Supp_Motor_Area_R	Supplementary motor area
21	Olfactory_L	Olfactory cortex
22	Olfactory_R	Olfactory cortex
23	Frontal_Sup_Medial_L	Superior frontal gyrus, medial
24	Frontal_Sup_Medial_R	Superior frontal gyrus, medial
25	Frontal_Mid_Orb_L	Superior frontal gyrus, medial orbital
26	Frontal_Mid_Orb_R	Superior frontal gyrus, medial orbital
27	Rectus_L	Gyrus rectus
28	Rectus_R	Gyrus rectus
29	Insula_L	Insula
30	Insula_R	Insula
31	Cingulum_Ant_L	Anterior cingulate and paracingulate gyri
32	Cingulum_Ant_R	Anterior cingulate and paracingulate gyri
33	Cingulum_Mid_L	Median cingulate and paracingulate gyri
34	Cingulum_Mid_R	Median cingulate and paracingulate gyri
35	Cingulum_Post_L	Posterior cingulate gyrus
36	Cingulum_Post_R	Posterior cingulate gyrus
37	Hippocampus_L	Hippocampus
38	Hippocampus_R	Hippocampus
39	ParaHippocampal_L	Parahippocampal gyrus
40	ParaHippocampal_R	Parahippocampal gyrus
41	Amygdala_L	Amygdala
42	Amygdala_R	Amygdala
43	Calcarine_L	Calcarine fissure and surrounding cortex
44	Calcarine_R	Calcarine fissure and surrounding cortex
45	Cuneus_L	Cuneus

46	Cuneus_R	Cuneus
47	Lingual_L	Lingual gyrus
48	Lingual_R	Lingual gyrus
49	Occipital_Sup_L	Superior occipital gyrus
50	Occipital_Sup_R	Superior occipital gyrus
51	Occipital_Mid_L	Middle occipital gyrus
52	Occipital_Mid_R	Middle occipital gyrus
53	Occipital_Inf_L	Inferior occipital gyrus
54	Occipital_Inf_R	Inferior occipital gyrus
55	Fusiform_L	Fusiform gyrus
56	Fusiform_R	Fusiform gyrus
57	Postcentral_L	Postcentral gyrus
58	Postcentral_R	Postcentral gyrus
59	Parietal_Sup_L	Superior parietal gyrus
60	Parietal_Sup_R	Superior parietal gyrus
61	Parietal_Inf_L	Inferior parietal, but supramarginal and angular gyri
62	Parietal_Inf_R	Inferior parietal, but supramarginal and angular gyri
63	SupraMarginal_L	Supramarginal gyrus
64	SupraMarginal_R	Supramarginal gyrus
65	Angular_L	Angular gyrus
66	Angular_R	Angular gyrus
67	Precuneus_L	Precuneus
68	Precuneus_R	Precuneus
69	Paracentral_Lobule_L	Paracentral lobule
70	Paracentral_Lobule_R	Paracentral lobule
71	Caudate_L	Caudate nucleus
72	Caudate_R	Caudate nucleus
73	Putamen_L	Lenticular nucleus, putamen
74	Putamen_R	Lenticular nucleus, putamen
75	Pallidum_L	Lenticular nucleus, pallidum
76	Pallidum_R	Lenticular nucleus, pallidum
77	Thalamus_L	Thalamus
78	Thalamus_R	Thalamus
79	Heschl_L	Heschl gyrus
80	Heschl_R	Heschl gyrus
81	Temporal_Sup_L	Superior temporal gyrus
82	Temporal_Sup_R	Superior temporal gyrus
83	Temporal_Pole_Sup_L	Temporal pole: superior temporal gyrus
84	Temporal_Pole_Sup_R	Temporal pole: superior temporal gyrus
85	Temporal_Mid_L	Middle temporal gyrus
86	Temporal_Mid_R	Middle temporal gyrus
87	Temporal_Pole_Mid_L	Temporal pole: middle temporal gyrus
88	Temporal_Pole_Mid_R	Temporal pole: middle temporal gyrus
89	Temporal_Inf_L	Inferior temporal gyrus
90	Temporal_Inf_R	Inferior temporal gyrus